Universität Hamburg
Fakultät für Mathematik,
Informatik und Naturwissenschaften
Fachbereich Physik

Theoretical and experimental investigation of nuclear spin dynamics in water and ammonia

Dissertation
zur Erlangung des Doktorgrades
an der Fakultät für Mathematik, Informatik und Naturwissenschaften
Fachbereich Physik
der Universität Hamburg

vorgelegt von
Guang Yang

Hamburg
2022

Gutachter der Dissertation:	Prof. Dr. Jochen Küpper Dr. Andrey Yachmenev
Zusammensetzung der Prüfungskommission:	Prof. Dr. Jochen Küpper Dr. Andrey Yachmenev Prof. Dr. Franz Kärtner Priv. Doz. Dr. Tim Laarmann Prof. Dr. Arwen Pearson
Vorsitzende/r der Prüfungskommission:	Prof. Dr. Arwen Pearson
Datum der Disputation:	25.11.2022
Vorsitzender Fach-Promotionsausschusses PHYSIK:	Prof. Dr. Wolfgang J. Parak
Leiter des Fachbereichs PHYSIK:	Prof. Dr. Günter H. W. Sigl
Dekan der Fakultät MIN:	Prof. Dr.-Ing Norbert Ritter

Abstract

Water and ammonia have two nuclear spin isomers *para* and *ortho* that differ by the total nuclear spin of the pair of identical hydrogen nuclei. They are essential molecules for life, which play important roles in many aspects such as chemistry, biology, medicine, and astrophysics. These two molecules contain the information of physics and chemistry at the early stage of molecular clouds. People can extract this information by measuring the *ortho-para* ratio, since the nuclear spin conversions between these two nuclear spin isomers are usually slow, and they are supposed to be two different molecules. Molecular collision is one of the most studied mechanisms resulting the nuclear spin conversion. No direct transitions have been ever observed in isolated water and ammonia molecules. However, the hyperfine effects like the nuclear spin-rotation and spin-spin interactions can make the transitions happen by introducing *ortho-para* mixing. The main goal of this thesis is to predict and observe the nuclear-spin-forbidden transitions of water and ammonia. This work can be divided into two major parts, the theoretical part and the experimental part.

In the theoretical part, the first comprehensive theoretical investigation of the hyperfine effects in $H_2{}^{16}O$ is presented, including the *ortho-para* transitions owing to the nuclear spin-rotation and spin-spin interactions. This was achieved by the newly developed general variational approach implemented in Richmol by adding the extra terms in the rovibrational Hamiltonian from TROVE that describes the nuclear spin-rotation and spin-spin interactions. The results suggest that the strongest *ortho-para* transitions intensities at room temperature are on the order of 10^{-31} cm/molecule, and should be detectable in the mid-infrared ν_2, and near-infrared $2\nu_1 + \nu_2$ and $\nu_1 + \nu_2 + \nu_3$ bands by current spectroscopy experiments.

In the experimental part, the broadband absorption spectra of the $3\nu_2$ band of $^{14}NH_3$ near 4 µm were recorded by a homebuilt Fourier-transform spectrometer. The Fourier transform spectrometer is based on a mid-infrared frequency comb with the repetition rate of 150 MHz. The frequency grid of the Fourier-transform spectrometer is set to be the same as the repetition rate of the frequency comb to remove the instrument line shape, resulting in a resolution of 0.00501 cm^{-1}. Line positions, line intensities, self-broadening, and self-shift parameters for six rovibrational lines were determined at room temperature. A liquid-nitrogen-cooled multi-pass-cell cryostat is planned to apply to increase the sensitivity of the Fourier transform spectrometer, and possibly observe the *ortho-para* transitions with the help of optical-optical double-resonance spectroscopy with a frequency comb probe.

Zusammenfassung

Wasser und Ammoniak haben zwei Kernspinisomere *para* und *ortho*, die sich durch den Gesamtkernspin der identischen Wasserstoffkerne unterscheiden. Es handelt sich um zwei für das Leben unverzichtbare Moleküle, die in vielen Bereichen eine wichtige Rolle spielen, z. B. in der Chemie, Biologie, Medizin und Astrophysik. Diese beiden Moleküle beinhalten Informationen der Physik und Chemie im frühen Stadium der Molekülwolken. Diese Informationen können durch Messung des *ortho-para* Verhältnisses ihrer Kernspin-Isomeren entnommen werden, da die Kernspinumwandlung zwischen zwei Kernspin-Isomeren in der Regel langsam ist und man davon ausgeht, dass es sich um zwei verschiedene Moleküle handelt. Die Molekülkollision ist einer der am besten untersuchten Mechanismen, der zu Informationen über die Kernspinumwandlung führt. In isolierten Wasser- und Ammoniakmolekülen wurden bisher keine direkten Übergänge beobachtet. Allerdings können die Hyperfeinstoffeffekte wie Kernspin-Rotation- und Kernspin-Spin-Wechselwirkungen zu Übergängen führen durch die Einführung von *ortho-para* Mischung. Das Hauptziel dieser Arbeit ist es, diese verbotenen Kernspinübergänge von Wasser und Ammoniak vorherzusagen und zu beobachten. Diese Arbeit kann in zwei Hauptteile unterteilt werden, einen theoretischen und einen experimentellen Teil.

Im theoretischen Teil wird die erste umfassende theoretische Untersuchung der Hyperfeinstoff-Effekte in $H_2{}^{16}O$ einschließlich der *ortho-para* Übergänge aufgrund der Kernspin-Rotation- und Kernspin-Spin-Wechselwirkungen präsentiert. Dies wird durch einen neu entwickeltem allgemeinen Variationsansatz erreicht, der in Richmol implementiert ist, indem die zusätzlichen Terme in den rovibrationalen Hamiltonian von TROVE, der die Kernspin-Rotation und die Kernspin-Spin-Wechselwirkung beschriebt. Die Ergebnisse legen nahe, dass die stärksten *ortho-para* Übergänge bei Raumtemperatur in der Größenordnung von 10^{-31} cm/Molekül liegen und in den Bändern im mittleren Infrarot ν_2 und im nahen Infrarot $2\nu_1 + \nu_2$ und $\nu_1 + \nu_2 + \nu_3$ in aktuellen Spektroskopieexperimenten.

Im experimentellen Teil wurden die breitbandigen Absorptionsspektren der $3\nu_2$-Bande von $^{14}NH_3$ bei 4 µm mit einem selbstgebauten Fourier-Transform-Spektrometer aufgenommen. Das Fourier-Transformations-Spektrometer basiert auf einem Mittelinfrarot-Frequenzkamm mit einer Wiederholrate von 150 MHz. Das Frequenzraster des Fourier-Transform-Spektrometers ist so eingestellt, dass es der Wiederholrate des Frequenzkamms entspricht, um die Linienform des Instruments zu entfernen, was zu einer Auflösung von 0,00501 cm^{-1} führt. Linienpositionen, Linienintensitäten, Selbstverbreiterung und Selbstverschiebung Parameter für sechs Rovibrationslinien wurden bei Raumtemperatur bestimmt. Ein mit flüssigem Stickstoff gekühlter Multi-Pass-Zellen-Kryostat soll eingesetzt werden, um die Empfindlichkeit des Fourier-Transform-Spektrometers zu erhöhen und möglicherweise die *ortho-para*-Übergänge mit Hilfe der optisch-optischen Doppelresonanzspektroskopie mit einer Frequenzkamm-Sonde zu beobachten.

Contents

1 Introduction

"To see a world in a grain of sand
And a heaven in a wild flower
Hold infinity in the palm of your hand
And eternity in an hour"

— William Blake

How did life form? This is one of the biggest questions that we can ask ourselves. A complete scientific answer still eludes us, but we have already solved many pieces of the puzzle. It all started from the Big Bang, where the first protons and neutrons condensed from more fundamental particles called quarks. This led to mostly hydrogen and helium nuclei in the early universe. After 380,000 years, the universe became cold and electrons started bonding to nuclei, the first hydrogen and helium atoms were formed. For heavier atoms such as C, N, and O, they came millions or billions of year later via fusion processes in the core of stars and supernovae explosions. The atoms cooled down to a low temperature and the chemical bonds formed between them, which produced the essential molecules for life, like H_2O, NH_3, and CH_4. With the radiation from nearby stars, chemical reactions among them took place forming more complex organic molecules for life.

H_2O and NH_3 are two essential molecules for life. Structures determine functions. It is important to study the structures of these two molecules, such as electronic structure, vibrations, rotations, fine structure, and hyperfine structure. Among them, the molecular hyperfine structure resulting from the nuclear spin is less studied due to more complex calculations and weaker interactions. What kind of roles do the nuclear spins of H_2O and NH_3 play in the evolution of life and the universe? How can we calculate and measure the hyperfine structure of these two molecules? This was where this thesis started.

1.1 The brief story of nuclear spin isomers

Spin is one of the most complicated and confusing concepts in physics. Tomonaga [1] and Gardner [2] gave a detailed description of the history of the spin and how spin "spins". Like mass and charge, spin is another intrinsic property of the particles. The particles can be visualized as a spinning top (Figure 1.1) instead of a spinning planet or basketball with a spin quantum number of $0, \frac{1}{2}, 1, \frac{3}{2} \cdots$. Particles with integer spins are bosons, and particles with half-integer spins are fermions. The half-integer spins result in a peculiar property of fermions which they return to the original state after two full rotations of the spin axis. Dirac's scissors trick and Möbius strip are two famous models used to demonstrate a macroscopic object returns to its original state after two full rotations [2].

Nuclear spin isomers, also called nuclear spin modifications, exist for molecules that are composed of identical nuclei with nonzero spin. Taking the simplest molecule hydrogen as an example, the possible orientations of the proton spin result in two nuclear spin isomers *ortho*-H_2 and *para*-H_2 with different arrangements of total nuclear spin quantum numbers $I = 1$ and $I = 0$ as shown in Figure 1.2 a. The discovery of nuclear spin and the process of the nuclear spin conversion in molecules is contemporaneous with the appearance of quantum mechanics and its application to the hydrogen molecule. The concept of *ortho* and *para* was first introduced in the observed spectrum of Clèveite gas (helium) from Runge and Paschen [4] in 1896. They recorded two sets of spectra, the stronger one belongs to helium, and the weaker one belongs to *Parhelium* which was rewritten as *para*-helium afterward. Later Bohr suggested naming the former *ortho*-helium [5]. During this time, the internal structure of atoms and molecules were still unclear to scientists. In 1911, Rutherfold [6]

Figure 1.1. Pauli and Bohr watching a spinning top, reprinted from [3].

proved his postulation of the nucleus by the alpha particles scattering experiment. In 1913, Bohr [7] introduced quantization in describing the electron motion around the atomic nucleus, which better explained the spectra of hydrogen. Nine years later, Stern and Gerlach (1922) [8] experimentally demonstrated the space quantization with the Silver beam in an inhomogeneous magnetic field, which acquired Stern a Nobel Prize in 1943 "for his contribution to the development of the molecular ray method and his discovery of the magnetic moment of the proton". But people still can not explain why helium had two different sets of spectra, and two more puzzling experimental results were coming out during this time. The first was the anomalous specific heat for H_2, when increased the temperature of cooled H_2 from Eucken [9] in 1912. The second was the intensity alterations with the ratio of 3:1 in the rotational spectra of H_2 from Hori [10] in 1927. These confusing experiments became the three main problems within the development of atomic physics, molecular physics, and quantum mechanics.

The exciting things happened in 1924 and 1925 when people were getting to understand the property of electrons. In 1924, de Broglie [11] came up with the hypothesis about the wave-particle duality of electrons. In 1925, Pauli [12] proposed that no two electrons in an atom can have identical sets of quantum numbers, which earned him a Nobel Prize in 1945 "for the discovery of the Exclusion Principle, also called the Pauli Principle". In the same year, Uhlenbeck and Goudsmit [13] postulated the existence of a new intrinsic property of particles that behaved like an angular momentum, which was later termed spin by Pauli. After introducing electron spin, the two sets of helium spectra were explained by Heisenberg [14] in 1927. The helium atom has two electrons, and the coupling between them results in the two sets of states: singlet where the orientations of two electron spins are

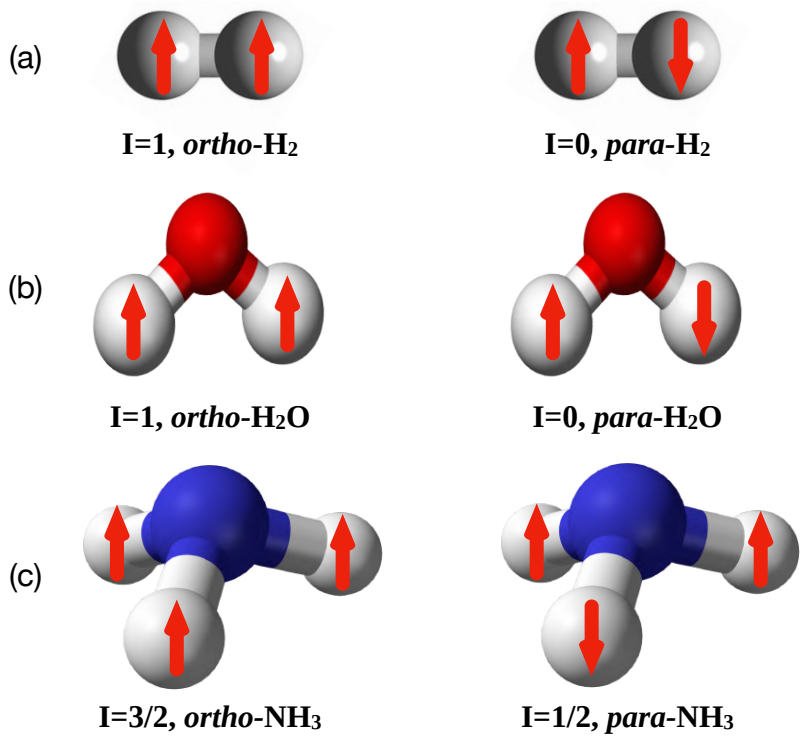

Figure 1.2. Nuclear spin isomers of hydrogen (a), water (b), and ammonia (c) molecules.

parallel, and triplet where they are not parallel. The singlet corresponds to the *para*-helium, and the triplet corresponds to *ortho*-helium. Furthermore, Heisenberg generalized these concepts to protons in H_2, and predicted the existence of *para*-H_2 and *ortho*-H_2 [5]. The Nobel Prize in 1932 was awarded to Werner Heisenberg "for the creation of quantum mechanics, the application of which has, inter alia, led to the discovery of the allotropic forms of hydrogen", which indicated *para*-H_2 and *ortho*-H_2 were a big issue at that time.

In 1927, Hund [15] investigated the correlation between energy levels and the symmetry of rotational wave functions of the hydrogen molecule. He separated the rotational levels by the parity of the rotation quantum number J as shown in Figure 1.3. Inspired by Heisenberg and Hund, Dennison [16] postulated hydrogen nuclei (photon) has the same half spin as the electron in the same year. Referring to the *para*-helium and *ortho*-helium from Heisenberg, the two nuclear spin isomers of hydrogen were named *para* and *ortho*, when the two photon spins are antiparallel and parallel respectively, as shown in Figure 1.2 a. The total nuclear spin quantum number of *para*-H_2 is 0, which corresponds to the energy levels with even rotation quantum number. And likewise, the total nuclear spin quantum number of *ortho*-H_2 is 1, which corresponds to the energy levels of odd rotation quantum number. Dennison's postulate gave a good explanation of the intensity alterations in rotational spectra of hydrogen molecule. The statistic weight of the *para*-H_2 and *ortho*-H_2 is 1 and 3. This means hydrogen molecules consist of one quarter of *para*-H_2 and three quarters of *ortho*-H_2 at room temperature. But at a lower temperature, the situation is different. The big rotational constant of H_2 gives rise to the big frequency intervals of energy levels. The interval between $J = 1$ and $J = 0$ level is 174 K as shown in Figure 1.3, which is much higher than the boiling point of liquid hydrogen (20.3 K). Thus, all the hydrogen molecules are populated on $J = 0$ state (*para*-H_2) when hydrogen molecules are cooled to 20.3 K. With this method, Bonhoeffer and Harteck [17] successfully made the pure *para*-H_2 in 1929. The problem of anomalous specific heat for H_2 was also solved based on Dennison's postulate,

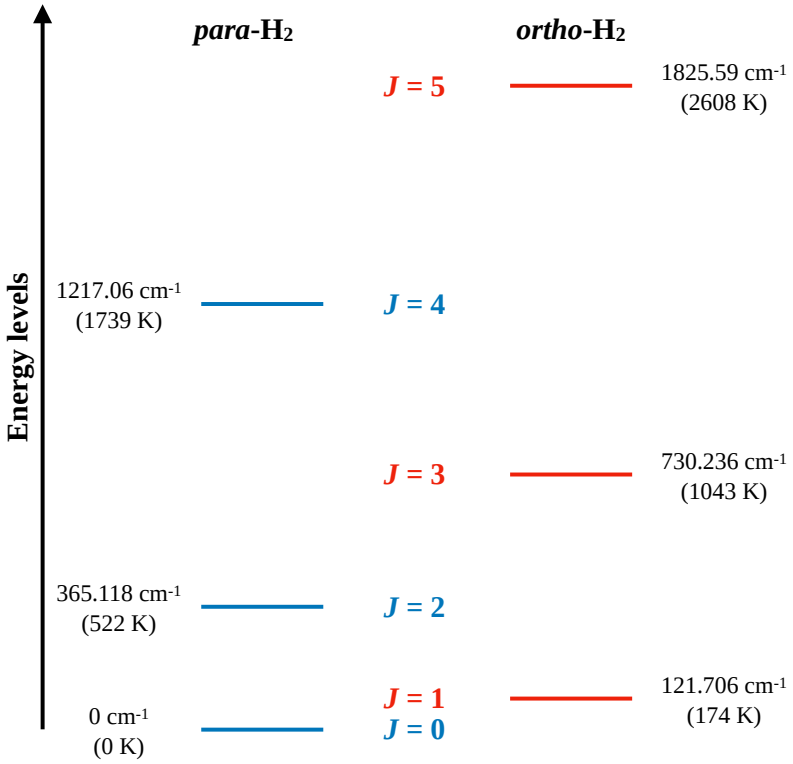

Figure 1.3. Lower rotational levels of H_2 molecule with rotational constant 60.853 cm^{-1}. The energy levels are given in cm^{-1} and K relative to the $J = 0$ level.

since more hydrogen molecules were populated to the *para* state at low temperature. Till 1927, the three problems were all resolved and explained, promoting the development of Pauli's spin theory [18] and launching a new era in modern quantum mechanics.

1.2 The *ortho-para* ratio and nuclear spin conversion

The *para*-H_2 ($I = 1$) and *ortho*-H_2 ($I = 0$) correspond to the two sets of energy levels. The radiative transitions between these two sets are very weak, which are considered to be forbidden. For other polyatomic molecules containing two identical protons, like H_2O (shown in Figure 1.2 b), H_2CO, and H_2S, the *ortho-para* conversion is almost rigorously forbidden in spectroscopy and collisions [5]. These two nuclear spin species are thought of as two independent molecules. This also refers to NH_3 (shown in Figure 1.2 c), CH_3F, CH_3OH, H_3^+ with *ortho* ($I = 3/2$) and *para* ($I = 1/2$) species, and CH_4 with one more meta ($I = 2$) besides *ortho* ($I = 1$) and *para* ($I = 0$) species.

We live in a molecular universe, where molecules are abundant and ubiquitous [20]. Many important processes, such as the formation of stars, the evolution of galaxies, and the origin of life, are driven by the presence of molecules. Consequently, molecules can be used to trace these important processes. The nuclear spin isomers retain the information of chemistry and physics at the early stage of the molecular clouds, since the conversions between different nuclear spin isomers are usually slow in the interstellar medium, comparable to the lifetime of the universe [5]. People can extract this information by measuring the *ortho-para* ratio (OPR) of different molecules, with consideration of the collisions and chemical reactions [21–23], especially the proton exchange reaction with H^+ [24] and H_3^+ [25]. H_2O and NH_3 are

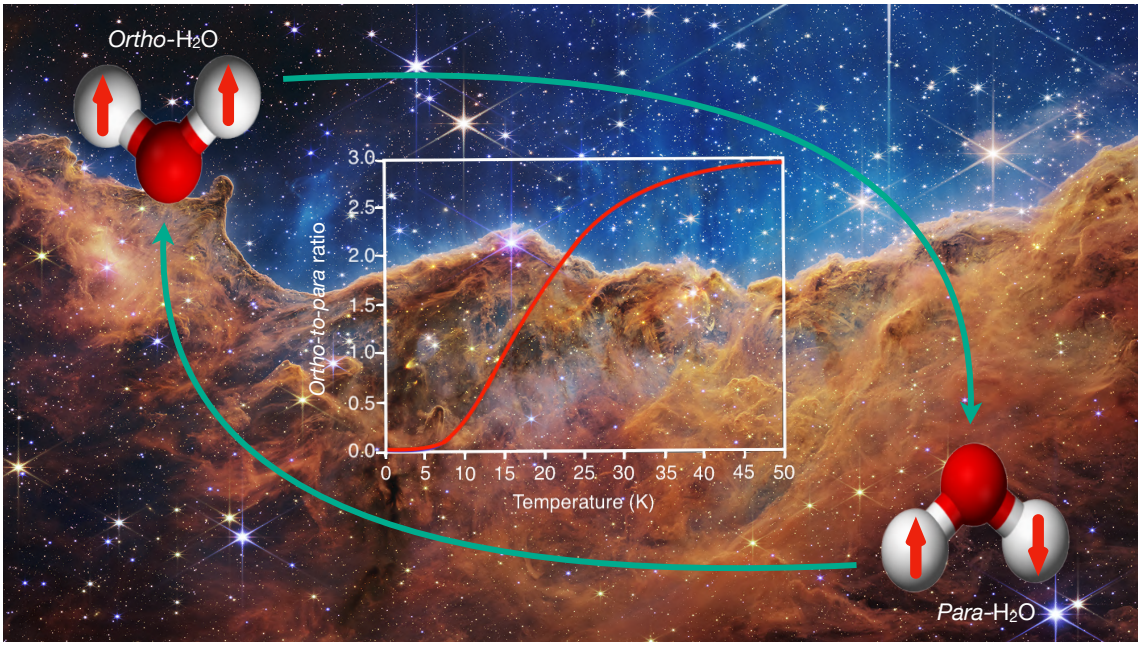

Figure 1.4. Nuclear spin conversion of H_2O in the interstellar medium, and approximate curve for the *ortho-to-para* ratio in lower temperatures adapted from [19]. The background is the first infrared view image of a nearby, young, star-forming region called NGC 3324 in the Carina Nebula from the James Webb Space Telescope (https://www.nasa.gov/webbfirstimages).

the two most important polyatomic molecules for astrophysical observation. Figure 1.4 gives an example of OPR as a function of its equilibrium temperature for H_2O. By observing the OPR of H_2O and NH_3 in cometary comae, star- and planet-forming regions [26–31], people can deduce the temperature to further investigate the chemical and physical history of these two molecules in these regions.

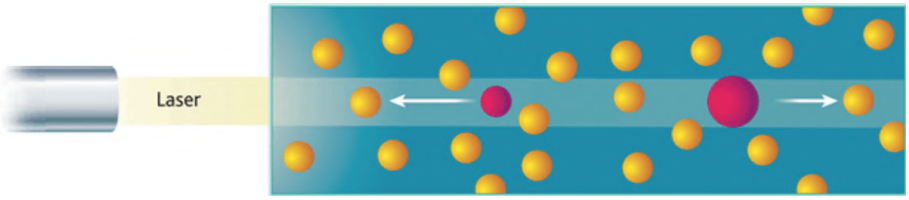

Figure 1.5. The principle of laser-induced drift, reprinted from [32]. The blue-detuned laser only excites the molecule (big red sphere on the right) moving away from the laser and increases the size (kinetic cross-section). This molecule is slowed down by collisions with the buffer gas (yellow sphere) because of its larger size. Whereas the molecule moving toward the laser will not excite, and keep moving at the normal speed. This difference causes a drift of the selected nuclear spin isomer toward the laser.

However, the real meaning of the OPR in the interstellar medium is still a topic of controversy. Theoretical and experimental investigations of the nuclear spin conversion are a straightforward way to better understand the OPR. Molecular collision is one of the most studied mechanisms resulting in the nuclear spin conversion in polyatomic molecules [35, 36]. The nuclear spin conversion has been studied for several molecules, such as H_2O [37, 38], H_2CO [39], CH_3F [36, 40], NH_3 [41], CH_3OH [42, 43], C_2H_4 [44, 45]. Among these molecules, the nuclear spin isomers of CH_3F, C_2H_4 and CH_3OH have been separated by laser-induced

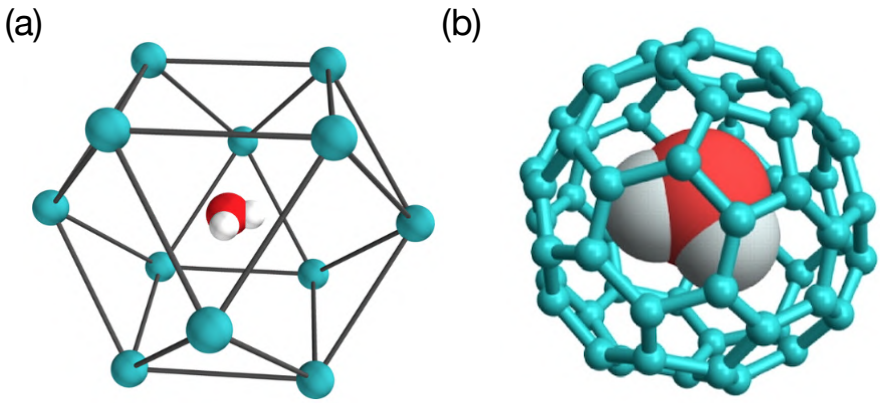

Figure 1.6. Diagram of water molecule isolated in an argon matrix and encapsulated in a fullerene cage, adapted from [33, 34].

drift method [46] (shown in Figure 1.5). Quantum relaxation theory is applied to explain the nuclear spin conversion with involving the nuclear spin-rotation, spin-spin, and quadrupole interactions. These intramolecular interactions mix the *ortho* and *para* states and the collision destruct the coherence between the states. Another mechanism promoting the nuclear spin conversion is the intermolecular interactions in the condensed phase. Nuclear spin conversion has been observed in noble gases or *para*-H_2 matrix (shown in Figure 1.6 a) for H_2O [33, 47–49], NH_3 [50, 51], CH_4 [52–54], CH_3OH [55, 56]. The host matrices confine the rotation of these guest molecules via Van der Waals force, resulting in stronger *ortho-para* mixing. By extending the matrix isolation to fullerene encapsulation [57], Beduz *et al.* [34] observed the *ortho-para* conversion of single water molecules trapped in a closed fullerene cage (shown in Figure 1.6 b).

1.3 Quantum control of nuclear spin isomers

Molecules are complex because they combine different well-separated quantum structures from electric structure to vibration, rotation, and hyperfine structure with reduced symmetry. Consequently, the molecular energy covers several orders of magnitude from more than 100 THz (electric structure) to around 10 THz (vibration), around 10 GHz (rotation), and around 10 MHz (hyperfine structure). With the Born-Oppenheimer approximation, the electronic degrees of freedom can be decoupled from the rovibrational motion. Vibrational and rotational motions can also be separated with the rigid-rotor approximation. These internal structures of molecules underly many possibilities for quantum control [58, 59] to study quantum information, quantum computers, fundamental constants measurement, possible physics beyond the Standard model, chemical reactions, catalysis, solution processes, and so on, even though with great experimental challenges. Since hyperfine transitions involve flipping of the nuclear spin, they are much more stable compared to rovibrational or electronic transitions, and suited for long-period quantum control.

Quantum control of nuclear spin species has been realized by many groups with different methods. Kravchuk *et al.* [60] produced an *ortho* H_2O beam with a purity of 93% by a magnetic-hexapole-focuser setup. Our group [61] applied the electric deflector (shown in Figure 1.7), acting like an "electric prism", to produce both pure *ortho*- and *para*-H_2O. With this method, chemical reactions towards trapped diazenylium ions (NH_2^+) are investigated, indicating that *para*-H_2O reacted 23% faster than *ortho*-H_2O [62]. Direct laser state-selectively cooling of nuclear spin isomers in one dimension has been achieved for

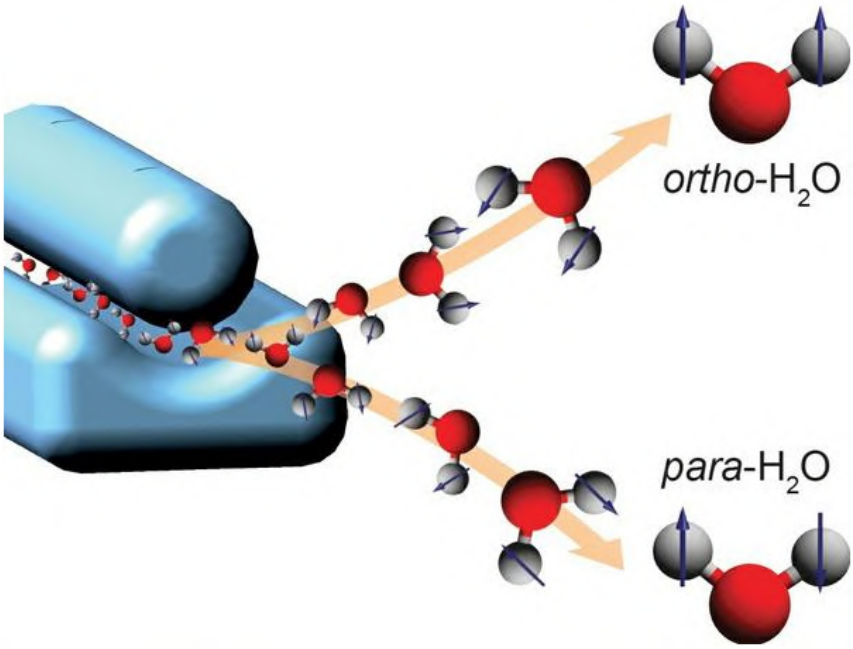

Figure 1.7. Separation of *ortho-* and *para*-H_2O with the electric deflector. The deflector produce a strong inhomogeneous electric field, which deflects the *ortho-* and *para*-H_2O differently from their original path because of the different interactions with electric field.

calcium monomethoxide ($CaOCH_3$) by Mitra *et al.* [63], reducing the temperature of around 10^4 molecules to 1.8 mK. More recently, Vilas [64] demonstrated the magnetic-optical trapping (MOT) of CaOH, suggesting MOT of $CaOCH_3$ is possible to realize.

1.4 Direct *ortho-para* transitions in isolated molecules

There are not strictly "forbidden transitions" if we consider the mixing of eigenfunctions for different states due to some weak internal interactions or the high order interactions beyond the electric dipole. The hyperfine effects such as nuclear spin-rotation, spin-spin, and quadrupole interactions result in the *ortho-para* mixing, and drive the direct electric or magnetic transitions between different nuclear spin isomers. For H_2, the lifetime of the spontaneous emission from $J = 1$ (*ortho*) to $J = 0$ (*para*) (shown in Figure 1.3) is much longer than the lifetime of the universe [65, 66]. Polyatomic molecules, especially the spherical-top molecules, have a faster conversion rate since the rotational levels are closer or clustered [32]. The first observation of direct *ortho-para* transition was realized by Ozier *et al.* [67] with shifting an *ortho* state close to *para* state under an external magnetic field. For rotational cluster states ($J = 53$) of SF_6, Bordé *et al.* [68] measured the transitions between different nuclear spin isomers.

More recently, Kanamori *et al.* [69] reported the microwave transitions between *ortho* and *para* states of an isolated disulfur dichloride (S_2Cl_2), a helically twisted molecule with especially stronger larger quadrupole interaction. The observed intensities of the forbidden transitions were 1000 times smaller than the allowed transitions nearby. This study indicated that the spontaneous emission between the *ortho* and *para* states of S_2Cl_2 molecule happens once every few thousand years.

1.5 Outline of this thesis

The main objective of this thesis is to predict and observe the nuclear-spin-forbidden transitions of water and ammonia. The first main goal is high-accuracy calculations of the hyperfine structure including the *ortho-para* transitions from first principles, and predictions of the strongest forbidden transitions to be possible observed in experiments for H_2O and NH_3. The second main goal concerns the accurate measurement of the hyperfine structure and possible forbidden *ortho-para* transitions in the rovibrational spectrum of H_2O and NH_3 with the Fourier transform spectrometer based on the mid-infrared frequency comb (FC). An overview of the structure of the thesis is described here.

In chapter 2, the fundamental concepts required to follow this thesis are provided. The chapter starts with a brief description of the quantum structure of molecules from electronic structure to hyperfine structure. Then the theoretical approach to constructing the molecular spectra from first principles is described, which includes solving the electronic Schrödinger equations, solving the nuclear Schrödinger equation, and simulating the absorption spectra. In chapter 3, the experimental setup of the mid-infrared FC and Fourier transform spectrometer, is presented.

In chapter 4, the first comprehensive theoretical investigation of the hyperfine effects and *ortho-para* transitions in $H_2{}^{16}O$ due to the nuclear spin-rotation and spin-spin interactions are described. We also present the details of our newly developed general variational approach to the simulation of hyperfine effects in polyatomic molecules. Our results for water suggest that the strongest *ortho-para* transitions with room-temperature intensities on the order of 10^{-31} cm/molecule are about an order of magnitude larger than previously predicted values, and should be detectable in the mid-infrared ν_2, and near-infrared $2\nu_1 + \nu_2$ and $\nu_1 + \nu_2 + \nu_3$ bands by current spectroscopy experiments.

In chapter 5, the broadband absorption spectra of the $3\nu_2$ band of $^{14}NH_3$ near 4 µm is reported. The data were recorded using a mid-infrared FC coupled to a homebuilt Fourier transform spectrometer with a resolution of 0.00501 cm^{-1}. Line positions, line intensities, self-broadening, and self-shift parameters for six rovibrational lines were determined at room temperature ($T = 296$ K). In chapter 6, a liquid-nitrogen-cooled multi-pass-cell cryostat and the optical-optical double-resonance spectroscopy with a FC probe are described as further improvements on our Fourier transform spectrometer.

Finally, in chapter 7, a summary of what has been achieved and an outlook over ongoing projects is given. In the appendices, more detailed information about the symmetry-adapted nuclear spin functions of H_2O and NH_3, hyperfine interaction in rotational chiral states of H_2S can be found.

2 Fundamental concepts

> *"If you want to find the secrets of the universe, think in terms of energy, frequency and vibration."*
>
> — Nikola Tesla

This chapter provides an overview of the quantum structure of molecules and theoretical rovibrational spectroscopy. For the different quantum structures, the orders of magnitude of various interactions are estimated by expressing as a power series of the fine structure constant and the Born-Oppenheimer constant [5]. A general outline of the stages for generating the rotation-vibration linelist is shown in Figure 2.1 by solving the electronic and nuclear Schrödinger equation. The readers are directed to [70, 71] and [72, 73] for detailed reviews of *ab initio* electronic structure calculations in Section 2.2, and variational nuclear motion calculations in Section 2.3, respectively. For more details, I recommend the textbooks [74–76].

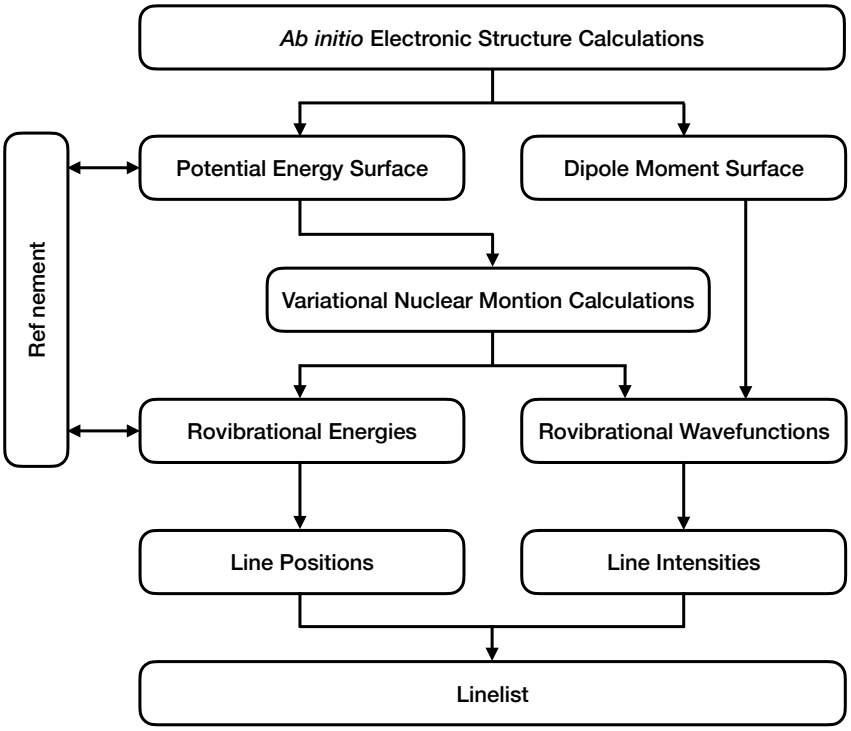

Figure 2.1. The procedure of computing a rotation-vibration linelist for a small polyatomic molecule from first principles, adapted from [77].

2.1 Quantum structure of molecules

A molecule is a collection of electrons and nuclei obeying quantum mechanics. They are held together by certain interactions. Each of them has a mass, an electric charge, a magnetic dipole moment for electrons, and electric and magnetic multipole moment for nuclei. Different interactions result in different structures. Solving the non-relativistic, time-independent Schrödinger equation $H\Psi = E\Psi$ provides a prescription to strictly determine

the quantum structure. The molecular Hamiltonian is written as

$$H = T + V + H_{es} + H_{hfs}, \tag{2.1}$$

where T is the kinetic energy operator, V is the electrostatic potential energy operator, H_{es} is the electron-spin Hamiltonian, and H_{hfs} is the hyperfine Hamiltonian. After the separation of translational energy, we write the internal dynamics Hamiltonian as [74]

$$\begin{aligned} H_{int} &= H_{rve} + H_{es} + H_{hfs} \\ &= T_e + T_N + V_{ee} + V_{Ne} + V_{NN} + H_{sl} + H_{ss'} + H_{Js} + H_{ns} + H_{quad}. \end{aligned} \tag{2.2}$$

The eigenstates of H_{rve} are the starting point for calculating the molecular energies. Under numerous approximations such as Born-Oppenheimer approximation, Hartree-Fock approximation, harmonic oscillator approximation, and rigid rotor approximation, people can solve approximate and separable Schrödinger equations for electron structure, vibrational states, and rotational states. Afterward, the approximations can be corrected by using the variational method or perturbation theory. The extra terms H_{es} and H_{hfs} are then treated as "add-on" terms giving rise to fine structure and hyperfine structure.

All molecular interactions and quantities can be expressed by three fundamental quantities—the elementary charge e, Planck constant $\hbar$, the speed of light c—and the mass of electrons m, the mass of nuclei M, and electric and magnetic multipole moment for nuclei. Two dimensionless quantities, the fine structure constant $\alpha = e^2/\hbar c$ and Born-Oppenheimer constant $\kappa = (m/M)^{1/4}$, can be applied to describe the different interactions as a power series of α and κ, as shown in Figure 2.2.

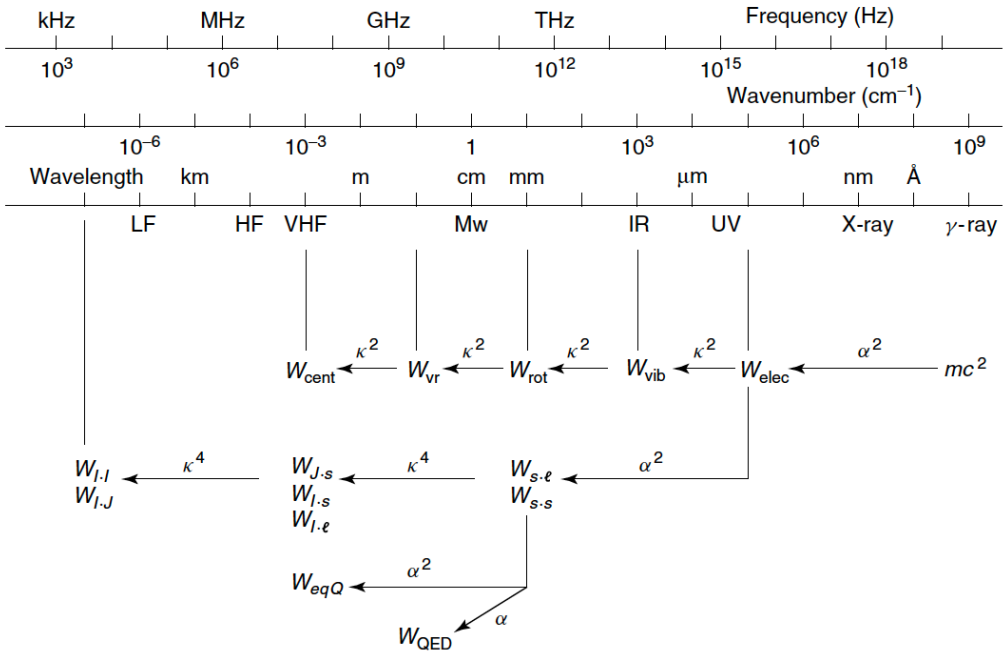

Figure 2.2. Orders of magnitude of all possible atomic and molecular interactions, reprinted from [5].

2.1.1 Born-Oppenheimer Approximation

To solve the rovibronic Schrödinger equation, the Born-Oppenheimer approximation [78] was introduced for separating the electronic motion from nuclear motion based on the fact that electrons are less massive than nuclei. The rovibronic wave function Ψ is separated into the product of electronic and nuclear components,

$$\Psi(r,R) = \psi_{elec}(r,R)\psi_{nuc}(R). \tag{2.3}$$

Choosing a fixed nuclear configuration, the electronic Schrödinger equation is given by

$$H_{elec}(r,R)\psi_{elec}(r,R) = E_{elec}(R)\psi_{elec}(r,R), \tag{2.4}$$

with the electronic Hamiltonian

$$H_{elec} = T_e + V_{ee} + V_{Ne} + V_{NN} \tag{2.5}$$

where V_{NN} is a constant for a selected nuclear coordinate. Solving (2.4) to get the electronic energy E_{elec} for a selection of nuclear geometries repeatedly gives the potential energy surface (PES) V_{PES}. Once the V_{PES} is determined, we can solve the nuclear Schrödinger equation

$$(T_N + V_{PES})\psi_{nul}(R) = E_{nul}\psi_{nul}(R), \tag{2.6}$$

to get the rovibrational energies of the system in the electronic state defined by PES. In this thesis, we only consider the ground electronic state.

2.1.2 Electronic structure

Many chemical processes can be understood through considering the interactions of electrons with nuclei, and interactions between electrons. It is important to calculate the electronic structure, especially PES and dipole moment surface (DMS), which are crucial in calculating the rovibrational spectrum of a molecule as shown in Figure 2.1. Many advanced methods have been developed to solve the electronic Schrödinger equation, which are described in Section 2.2. The DMS represents the charge distribution of a molecule as a function of nuclear geometry. The dipole moment is defined in terms of the molecule's response to an applied electric field and can be calculated as the first derivative of the electronic energy with external electric field strength ϵ_A according to

$$\mu_A = -\left(\frac{dE}{d\epsilon_A}\right)_{(\epsilon_A=0)}, \tag{2.7}$$

which can be approximated by using the numerical finite differences

$$\frac{dE}{d\epsilon_A} \approx \frac{E(\epsilon_A) - E(-\epsilon_A)}{2\epsilon_A}, \tag{2.8}$$

where a small electric field is applied along the Cartesian coordinate axis A= X, Y, Z. The DMS can be calculated as the expectation value of the dipole moment operator.

The electron energy of a hydrogen atom is used to estimate the order of magnitude of the molecular electronic energy [5]

$$W_{elec} = \frac{mv^2}{2} - \frac{e^2}{r} = -\frac{mv^2}{2} = -\frac{1}{2}mc^2\alpha^2 = -\frac{Ry}{n^2} \sim 10000 \text{ cm}^{-1}, \tag{2.9}$$

where Ry is the Rydberg constant given by 109737.31568160(21) cm^{-1} and α is the fine structure constant in the cgs unit with the expression

$$\alpha = \frac{e^2}{\hbar c} = \frac{v}{c} \sim 10^{-2}, \tag{2.10}$$

indicating that the velocity of electrons in atoms or molecules is on the order of 3000 km/s.

2.1.3 Vibrational and rotational states

The choice of a coordinate system to describe the molecular nuclear motion is important for solving the nuclear Schrödinger equation. In a space-fixed frame, a molecule with N atoms requires $3N$ Cartesian coordinates to specify the positions of the atoms without distinguishing the three different types of molecular motion: translation, vibration, and rotation. After removing three translational motions, molecular vibration and rotation can be distinguished by transforming them into a suitable molecular-fix frame. The Euler angles define the orientation of the molecule-fixed axes to the space-fixed axes, and describe the overall rotation of the molecule. The remaining $3N-6$ coordinates correspond to vibration. Theoretical ROVibrational Energies (TROVE) approach [72, 73] is applied to calculate the rotation-vibration energy levels and corresponding transition intensities for a polyatomic molecule of arbitrary structure in an isolated electronic state, as described in Section 2.3.

To better sort out the order of magnitude of the molecular vibration and rotation, the Born-Oppenheimer constant is introduced as

$$\kappa = \left(\frac{m}{M}\right)^{\frac{1}{4}} \sim 10^{-1}, \tag{2.11}$$

where M is the average nuclear mass. The order of magnitude of vibrational energy is

$$W_{vib} \sim \kappa^2 Ry \sim 1000 \text{ cm}^{-1}, \tag{2.12}$$

with the velocity of the vibrational motion on the order of $V_v \sim \kappa^3 \alpha c \sim 3$ km/s. The order of magnitude of rotational energy is

$$W_{rot} \sim \frac{1}{2} M V_r^2 \sim \kappa^4 Ry \sim 10 \text{ cm}^{-1}, \tag{2.13}$$

for a low rotational quantum number with the velocity of the rotation motion on the order of $V_r^2 \sim \kappa^4 \alpha c \sim$ 300 m/s.

2.1.4 Fine and hyperfine structure

The fine structure results from the interaction of electron spin magnetic moments with the other magnetic moments in the molecule, such as electron spin–orbit interaction H_{sl}, electron spin-electron spin interaction $H_{ss'}$, and electron spin-nuclear rotation interaction H_{Js}. The energies of electron spin–orbit interaction and electron spin-electron spin interaction are both on the order of

$$W_{s\cdot l} \sim W_{s\cdot s'} \sim \alpha^2 Ry \sim 10 \text{ cm}^{-1}, \tag{2.14}$$

and the energy of electron spin-nuclear rotation interaction is on the order of

$$W_{J\cdot s} \sim \kappa^4 \alpha^2 Ry \sim 10^{-3} \text{ cm}^{-1} \sim 30 \text{ MHz}. \tag{2.15}$$

The hyperfine fine structure arises from interactions of the magnetic and electric moments

of the nuclei with the other electric and magnetic moments in the molecule. Since the parity of 2^k multipole moments go as $(-1)^k$ for electric moments and $(-1)^{k-1}$for magnetic moments, there are only even electric multipole moments and odd magnetic multipole moments [79]. For hyperfine structure, we only consider the interaction energy of nuclear magnetic dipole moments H_{ns}, and interaction energy of nuclear electric quadrupole moments with electric field gradients H_{quad}, after neglecting the high order interactions like magnetic octupole moment. H_{ns} includes 4 terms which are nuclear spin-electron spin interaction H_{Is}, nuclear spin-electron orbit interaction H_{Il}, nuclear spin-nuclear spin interaction H_{II}, and nuclear spin-nuclear rotation interaction H_{IJ}. The energies of nuclear spin-electron spin interaction and nuclear spin-electron orbit interaction are both on the order of

$$W_{I\cdot s} \sim W_{I\cdot l} \sim \kappa^4 \alpha^2 Ry \sim 10^{-3}\ \mathrm{cm}^{-1} \sim 30\ \mathrm{MHz}, \tag{2.16}$$

and the energies of nuclear spin-nuclear spin interaction and nuclear spin-nuclear rotation interaction are both on the order of

$$W_{I\cdot I} \sim W_{I\cdot J} \sim \kappa^8 \alpha^2 Ry \sim 10^{-7}\ \mathrm{cm}^{-1} \sim 3\ \mathrm{kHz}. \tag{2.17}$$

In addition, the superfine and superhyperfine structures will be mentioned when the molecules are populated to rotational cluster states, especially for XY_6-type molecules [80, 81].

2.2 Electronic structure calculations

The electronic structure calculations are based on the concept of mean-field theory, where the electronic states are represented by a set of occupied molecular orbits (MOs). Many methods have been developed to determine the electronic structure by approximately solving the electronic Schrödinger equation, such as configuration interaction (CI), coupled-cluster (CC) theory, density functional theory (DFT) [82], and Möller-Plesset (MP) perturbation theory [83]. CC method was applied in our calculation, and only CI and CC are discussed in the following sections.

2.2.1 Hartree-Fock approximation

The Hartree-Fock (HF) approximation [84, 85], also called the self-consistent-field method, considers finding the optimized set of spin-orbitals with the lowest energy. This is realized by solving the HF equations with an iterative procedure based on the variational principle

$$E_{HF} = \frac{\langle \psi_{HF} | H_{elec} | \psi_{HF} \rangle}{\langle \psi_{HF} | \psi_{HF} \rangle} \geqslant E_{exact}, \tag{2.18}$$

where ψ_{HF} is the electronic wave function defined by the n-electron Slater determinant, see (3.28) in [75]. The HF energy E_{HF} provides an upper bound to the exact electronic ground energy with the corresponding HF wave function that forms the basis of many post-HF methods. The energy difference between the HF energy and the exact electronic energy is called the electron correlation energy. Many methods focus on recovering the electron correlation effects, and some of them will be discussed in the following sections.

2.2.2 Configuration interaction

The CI is the most straightforward post-HF method. The CI wave function is given by a linear combination of Slater determinants (or configurations), describing the "excitations"

from the HF "reference" determinant [70]. If all possible configurations are constructed, we get the full configuration interaction (FCI). FCI is usually not possible due to factorially increasing the configurations, but for very small molecules. Instead, CI expansion must be truncated at some level of excitation, with single electron excitations called CIS and double excitations called CISD. These truncations limit the accuracy of the calculations and cause the size extensive problem. Modifications to CI have been developed to deal with the lack of size extensivity, but simply CC methods are preferred [86].

2.2.3 Coupled-cluster theory

CC is commonly used as a preferred post-HF method for electric structure calculation, see [70, 87] for a detailed review. CC constructs multi-electron wave functions using the exponential cluster operator based on the HF method to account for electron correlation

$$\psi_{CC} = e^{T}\psi_{HF}, \tag{2.19}$$

where the cluster operator $T = \sum_{\mu} t_{\mu}\tau_{\mu}$ is a linear combination of excitation operators τ_{μ} multiplied by corresponding associated cluster amplitude t_{μ}. The CC theory provides an exact solution to the electronic Schrödinger equation in a given one-electron basis set by including all the possible excitations in the cluster operator which is equivalent to FCI on the same basis. Similar to CI, the cluster operator is truncated due to the expensive calculation. By introducing the notation

$$T = T_1 + T_2 + T_3 + ..., \tag{2.20}$$

we produce the different levels of CC theory: CC singles theory (CCS), CC singles-and-doubles theory (CCSD), CC singles-doubles-triples theory (CCSDT), and the additional letters referring to higher excitations. It is usually computational infeasible if we go beyond CCSD. A successful approximation to treat the triples contribution is CCSD(T), which includes a triples contribution calculated by 4th and 5th order MP perturbation theory connecting with the CCSD amplitudes [88–90].

Explicitly correlated F12 methods provide an efficient and high-accuracy way for electronic structure by introducing an explicit dependence of the interelectronic distance R_{12} into the wave function and have been applied to CI, MP perturbation theory, and CCSD [91, 92]. Currently, most quantum chemistry software packages applied the CCSD(T)-F12 method because of the simplicity and effectiveness [93].

2.2.4 One-electron basis sets

The one-electron spin-orbitals, also known as atomic orbitals, are the fundamental bricks for building the molecular wave function, and much progress has been made in developing them as basis sets. Each basis set is designed for modeling a specific physical property at the complete basis set (CBS) limit, and there is not an optimum basis set that can employ in all scenarios. There are two types of commonly used basis functions in quantum chemistry, which are Slater-type orbitals [94] and Gaussian-type orbitals (GTOs) [95]. In practical calculations, GTOs are preferred due to the efficient computation in integrals. GTOs in Cartesian coordinates are given by

$$G_{\zeta,l_x,l_y,l_z}(x,y,z) = Nx^{l_x}y^{l_y}z^{l_z}e^{-\zeta r^2}, \tag{2.21}$$

where $l_x + l_y + l_z$ determines the type of orbital, ζ defines the radial extent of the function, N is a normalization constant. A single Gaussian function is known as a primitive and linear combinations or contractions of primitives are taken to form MO functions

$$\chi_k = \sum_{l_x,l_y,l_z} d^k_{l_x,l_y,l_z} G_{\zeta,l_x,l_y,l_z} \tag{2.22}$$

with the contraction coefficients $d^k_{l_x,l_y,l_z}$. Contraction gives a more compact basis set and two different approaches are performed, which are general contraction [96] and segmented contraction [97].

There are a lot of Gaussian basis sets assembled with slightly different principles [98]. We only mention the correlation-consistent basis sets and their corresponding explicitly correlated F12 basis sets. Firstly proposed by Dunning [99], the correlation-consistent polarized valence basis sets are denoted by cc-pVXZ where basis set size increases with X = D, T, Q, 5, 6, 7. The cc-pVXZ basis sets provide a systematic route towards the CBS limit for correlated methods. Generally speaking, at each step up in X, functions of different angular momentum are added in a structured manner to recover more of the correlation energy. Some widely employed basis sets are core-valence cc-pCVXZ, weighted core-valence cc-pwCVXZ, and augmented correlation-consistent, aug-cc-pVXZ [99–101]. For the recent advancements in explicitly correlated (F12/R12) methods [102–104], some cc-F12/R12 optimized basis sets have been developed [105–107].

2.2.5 Additional higher-level corrections

Due to the limitations of electronic structure methods, a pure *ab initio* PES is challenging for high-accuracy rovibrational energy level calculations. To achieve high accuracy, people must consider the higher-level electron correlation beyond CC method for generating the PES with a one-electron basis set near the CBS limit [108]. Core valence electron correlation [71], higher-order electron correlation [109, 110], scalar relativistic effects [111] and the Born-Huang approximation [112] are considered to be the leading high-level contributions. Despite the expensive computation, these considerations can significantly improve the accuracy of the calculated rotation-vibration energy levels.

2.3 Theoretical ROVibrational Energies (TROVE)

With the PES from *ab initio* electronic structure calculation, we can now move on to solving the rotation-vibration Schrödinger equation. Variational methods provide a complete treatment of the nuclear motion problem, and can achieve exceptional accuracy. Besides, pure vibrational methods have been developed with the progress in electronic structure theory, including the vibrational self-consistent field method, vibrational CI, and vibrational CC theory [113, 114]. TROVE [72, 73] is a variational nuclear motion program and "black box" for calculating the rovibrational spectra for a polyatomic molecule of the arbitrary structure consisting of the rotation-vibration energy levels and corresponding transition intensities. The generality of TROVE has applied to many molecular systems comprising up to five atoms [115–122].

2.3.1 Kinetic energy operator

By diagonalizing the rovibrational Hamiltonian constructed in terms of a symmetry-adapted basis set, we get the solution of the rotation-vibration Schrödinger equation given by (2.6) in TROVE. The rovibrational Hamiltonian is described in the product form as

a truncated power series expansion around the equilibrium geometry or some non-rigid flexible configurations. The expansion is usually in terms of internal coordinates defined by users.

The molecular kinetic energy operator (KEO) with M vibrational modes can be expressed by

$$T_N = \frac{1}{2}\sum_{\lambda,\mu=1}^{M+3} \Pi_\lambda^\dagger(\xi) G_{\lambda\mu}(\xi)\Pi_\mu + U(\xi), \tag{2.23}$$

where $\xi = (\xi_1, \xi_2, ...\xi_M)$ is the vibrational coordinate, and $\Pi = (p_1, p_2, ..., p_M, J_x, J_y, J_z)$ is the generalized momenta with $p_n = -i\hbar\partial/\partial\xi_n$ and the components of total angular moment J_x, J_y, J_z. The kinetic energy matrix $G_{\lambda\mu}(\xi)$ and the pseudopotential $U(\xi)$ are constructed in a recursive numerical procedure. Together with PES, they are represented as series expansions in terms of functions of the generalized coordinates with truncation order defined by the user.

2.3.2 Vibrational coordinates

To compute the kinetic energy operator in (2.23), it is necessary to define a molecule-fixed axis system by satisfying the Eckart conditions [123]. The Eckart frame minimizes rovibrational coupling by the maximum separation between vibrational and rotational motion, consequently accelerating basis set convergence when computing rovibrational energy levels. Two types of vibrational coordinates are usually employed in practical calculations. The first is linearized coordinates [72]. They are in terms of Cartesian displacements of the nuclei from their equilibrium positions in the molecule-fixed axis system. The second is curvilinear internal coordinates [115] implemented in TROVE recently, which improve basis set convergence of rovibrational calculations.

2.3.3 Rovibrational basis set

After the numerical construction of the rovibrational Hamiltonian, people must choose a suitable rovibrational basis set to solve the nuclear Schrödinger equation with a variational approach. In TROVE, the vibrational basis set is constructed as products of one-dimensional primitive functions

$$|v\rangle = \prod_v |v_v\rangle = \phi_{v_1}(\xi_1)\phi_{v_2}(\xi_2)...\phi_{v_M}(\xi_M), \tag{2.24}$$

where each $\phi_{v_M}(\xi_M)$ depends on one internal coordinate. Functions of stretching, bending and inversion coordinates are usually chosen. For the stretching and inversion functions, the Numerov-Cooley method is applied to solve the 1D Schrodinger equation [124, 125]. For the bending functions, the harmonic oscillator approach is performed.

The rotational basis set $|J, K, m, \pm\rangle$ in TROVE is built from the rigid-rotor functions, see (73) and (74) in [72]. The final rovibrational basis set is then given by

$$|v, J, K, m, \pm\rangle = \prod_v |v_v\rangle \times |J, K, m, \pm\rangle. \tag{2.25}$$

Symmetry plays an important role in computing the rovibrational spectra of polyatomic molecules. Using a symmetry-adapted basis set can reduce the Hamiltonian matrix to be block diagonal. Each block corresponds to an irreducible representation of the molecular symmetry group [74]. This is helpful when handling the large matrices associated with the variational calculations since each block can be diagonalized separately. The calculated energy levels are labeled with symmetry, which is useful for computing spectra by imposing

additional selection rules. The approach to realizing the symmetry-adapted basis set is detailed in [73].

2.3.4 Potential energy surface refinement

The PES is the foundation of nuclear motion calculations. For larger polyatomic molecules, the electronic structure calculation is much more expensive. To realize the "spectroscopic" accuracy in rovibrational calculation compared with experiments, it is common for adjusting the analytic representation of the PES based on the experimental data. The procedure for empirical refinement was reported in [126] by applying an efficient least-squares fitting. The principle is to treat the effect of refinement as a perturbation ΔV to *ab initio* PES V_{PES} in terms of

$$\Delta V = \sum_{ijk\ldots} \Delta f_{ijk} \{\xi_1^i \xi_2^j \xi_3^k \ldots\}^A, \tag{2.26}$$

where Δf_{ijk} is the corrections to the original PES expansion parameters f_{ijk}, and the expansion terms $\{\xi_1^i \xi_2^j \xi_3^k \ldots\}^A$ are symmetrized combinations of vibrational coordinates ξ. The new perturbed Hamiltonian is given by

$$H_{rv} = T_N + V_{PES} + \Delta V, \tag{2.27}$$

and then diagonalized with a basis set of eigenfunctions from the unperturbed Hamiltonian. Each iteration implements the previous "unperturbed" basis set in this way until a desirable quality PES is reached.

2.4 Simulation of absorption spectra

2.4.1 Line intensities and selection rules

Electromagnetic waves can induce oscillating electric or magnetic moments in molecules, resulting in the absorption of photons with specific frequencies satisfied by certain resonance conditions. The amplitude of each moment is the transition moment between an initial state i and a final state f, which is related to the line strength in the following form

$$S(f \leftarrow i) = g_{ns} \sum_{m_i, m_f} \sum_{A=X,Y,Z} \left| \langle \phi_{rv}^{(f)} | \mu_A | \phi_{rv}^{(i)} \rangle \right|^2, \tag{2.28}$$

where g_{ns} is the nuclear spin statistical weight, μ_A is the electronically averaged DMS in the space-fix axis system. With the line strength, we can determine two important parameters in the cgs unit for rovibrational spectroscopy which are Einstein A coefficient

$$A_{fi} = \frac{64\pi^4 \nu_{if}^3}{3h g_f} S(f \leftarrow i), \tag{2.29}$$

and spectral line intensity

$$I(f \leftarrow i) = \frac{8\pi^3 N_A \nu_{if} e^{-E_i/k_B T} \left(1 - e^{-hc\nu_{if}/k_B T}\right)}{3hcZ(T)} S(f \leftarrow i), \tag{2.30}$$

where $\nu_{if} = |E_i - E_f|$ is the transition wavenumber with E_i and E_f as energy term values of initial and final states, $Z(t)$ is the partition function.

In order for the line strength in (2.28) not to vanish, the molecular symmetry of the rovibrational wave functions must satisfy [74]

$$\Gamma(\phi^*_{rv,j'}) \otimes \Gamma(\phi_{rv,j}) \supset \Gamma(\mu_A). \tag{2.31}$$

For vibrational transitions between vibrational states $\phi_{vib,v'}$ and $\phi_{vib,v''}$ in an electronic state, the selection rule is

$$\Gamma(\phi^*_{vib,v'}) \otimes \Gamma(\phi_{vib,v}) \supset \Gamma(T_\alpha). \tag{2.32}$$

where $\Gamma(T_\alpha)$ is the symmetry species of α component of the translational normal coordinate. For the rotational transitions, the selection rules are

$$\begin{aligned} \Delta J &= 0, \pm 1, \\ \Delta K &= 0, \pm 1. \end{aligned} \tag{2.33}$$

2.4.2 Line profiles and absorption cross-sections

The spectra lines have characteristic widths and shapes. Doppler effect and the finite lifetime of states are the two main important causes of line broadening. The molecules in the gas phase are not at rest and have a distribution of speeds. For a molecule with a speed of v moving to the direction of propagation of radiation with frequency ν_{fi}, there will be a shift by $\nu_{fi} \cdot (v/c)$ due to the Doppler effect. The cumulative effects of molecules moving with different velocities result in the inhomogeneous broadening of the spectral lines. This is well represented by a Gaussian profile,

$$f_G(\nu) = \sqrt{\frac{ln2}{\pi \alpha_D^2}} exp\left(-\frac{ln2(\nu - \nu_{ij})}{\alpha_D^2}\right) \tag{2.34}$$

with the half-width at half-maximum (HWHM)

$$\alpha_D = \frac{\nu_{ij}}{c}\sqrt{\frac{2N_A kTln2}{M}}. \tag{2.35}$$

Molecular energy levels have a finite natural radiative lifetime, which results in intrinsic or natural linewidth. Collisions between molecules reduce the lifetime of an excited state, and the linewidth will increase by raising the pressure. This mechanism is called collisional or pressure broadening, and it is represented by a homogeneous Lorentz profile,

$$f_L(\nu) = \frac{1}{\pi} \frac{\gamma(p,T)}{\gamma(p,T)^2 + [\nu - (\nu_{ji} + \delta(p_{ref})p)]^2}, \tag{2.36}$$

with the pressure induced line shift $\delta(p_{ref})$ and the HWHM

$$\gamma(p,T) = \left(\frac{T_{ref}}{T}\right)^{n_{air}} \left(\gamma_{air}(p_{ref},T_{ref})(p - p_{self}) + \gamma_{self}(p_{ref},T_{ref})p_{self}\right). \tag{2.37}$$

The most used approximation to the line shape is the Voigt profile, which is a convolution of a Gaussian and Lorentz profile. Although it can simulate both thermal and collisional effects, it cannot provide an accurate representation of the spectral line shapes [127]. Two more effects should be considered in the line profile, velocity change due to collisions reducing the Doppler linewidth and the speed-dependent influence on the relaxation rates. Hartmann-Tran profile with seven parameters is a more reliable reference line profile, and

is highly recommended [128].

For a single line $f \leftarrow i$, the spectral line intensity I_{fi} is related to the corresponding integration of absorption cross-section $\sigma_{fi}(\nu)$:

$$I_{fi} = \int_{-\infty}^{+\infty} \sigma_{fi}(\nu) d\nu. \tag{2.38}$$

By introducing the normalized line profiles $f_{\nu_{fi}}(\nu)$ which is aforementioned, the absorption cross-section can be defined as

$$\sigma_{fi} = I_{fi} f_{\nu_{fi}}(\nu). \tag{2.39}$$

The absorption cross-sections are related to the experimental measured quantities transmittance T and absorbance A by the Beer-Lambert law:

$$T = \frac{I_{tr}}{I_{in}} = e^{-\sum_{k=1}^{N} n_k L \sigma_k} \tag{2.40}$$

$$A = -log_{10} T \tag{2.41}$$

where I_{tr} and I_{in} are the input and output radiation fluxes respectively, N is the number of absorbing species, L is the optical path length, n_k is the number density of absorbers of species k, and σ_k is the corresponding absorption cross-section. Finally, we can generate the synthetic spectra based on the theoretical linelist, and compare with experimental spectra databases such as HITRAN [129], CDMS [130], JPL [131], PNNL [132], and GEISA [133].

3 Experimental setup

"One shall stand, one shall fall."

— Optimus Prime

The chapter serves as an overview and supplement of the experimental setup reported in chapter 5. The experimental setup was used for measuring the absorption spectrum of ammonia in collaboration with Ingmar Hartl's group. The schematic diagram is shown in Figure 3.1.

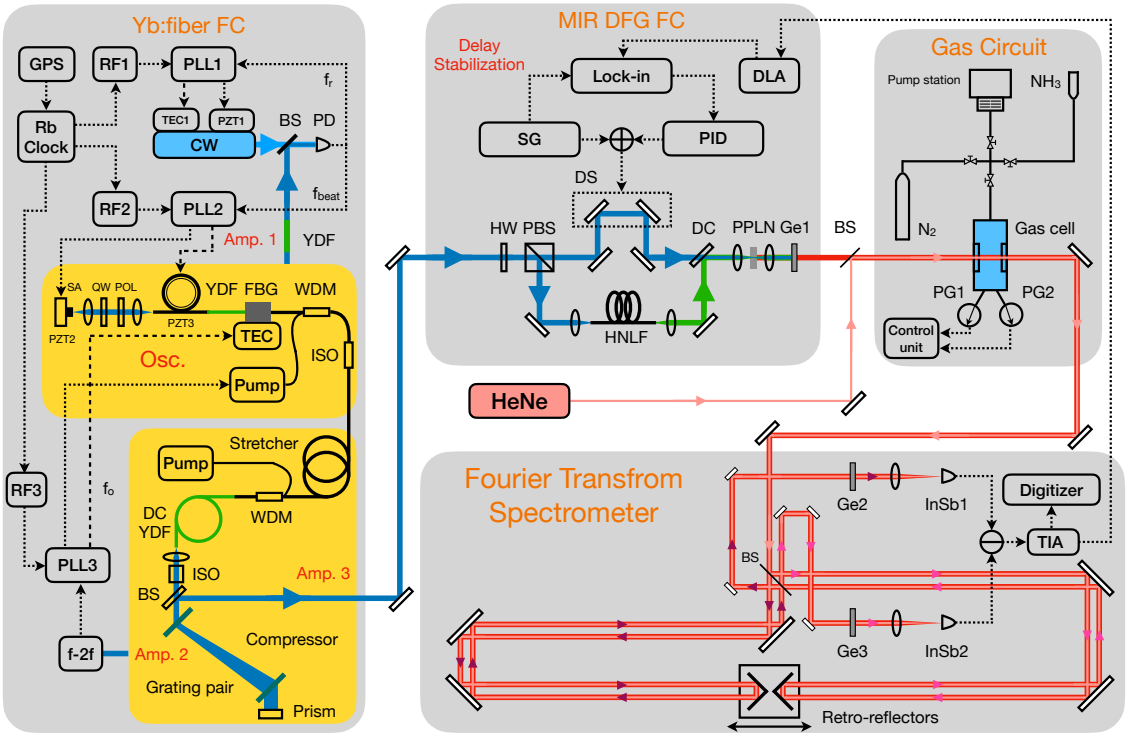

Figure 3.1. Schematic of the experimental setup. It mainly consists four parts: Yb:fiber frequency comb (Yb:fiber FC), DFG based mid-infrared frequency comb (MIR DFG FC), gas circuit, and Fourier transform spectrometer. The following abbreviations are used in these four parts. Yb:fiber FC: SA, saturable absorber; PZT, piezoelectric ceramic transducer; QW, quarter-wave plate; POL, polarizer; YDF, Yb doped fiber; FBG, fiber Bragg grating; TEC: thermoelectric cooler; WDM, wavelength division multiplexer; ISO, optical isolator; DC-YDF: double-cladding YDF; BS, beam splitter; RF, radio frequency; PLL, phase-locked loop; PD, photodiode. MIR DFG FC: HW, half-wave plate; PBS, polarization beam splitting cube; DS, delay stage; DC, dichroic mirror; PPLN, periodically poled Lithium Niobate; Ge, Germanium filter; HNLF, highly-nonlinear suspended-core fiber; SG, signal generator, PID, proportional–integral–derivative controller; Lock-in, lock-in amplifier; DLA, demodulating logarithm amplifier. Gas circuit: PG, pressure gauge; N_2, nitrogen bottle; NH_3, ammonia bottle. Fourier transform spectrometer: InSb, indium antimonide detector; TIA, transimpedance amplifier.

3.1 Frequency comb based on mode-lock laser

Optical frequency combs (FCs) are laser sources whose spectra involve a series ($\sim 10^5$) of discrete, equally spaced frequency lines. Figure 3.2 a illustrated the generation of a FC. The optical waves are phase synchronized due to phase coherence between the modes of cavity, and produce a optical pulse circulating inside the cavity [134]. The comb frequencies are given by

$$f_n = nf_r + f_o, \tag{3.1}$$

here f_r is the repetition rate, f_o is an frequency offset originates from the carrier-to-envelop offset phase, both f_r and f_o are in the range of 0.1 to 10 GHz corresponding to $n = 10^4...10^6$ for f_n being near-infrared range. The FC can operate as an optical clockwork to connect microwave to optical, optical to microwave, and optical to optical as shown in Figure 3.2 b.

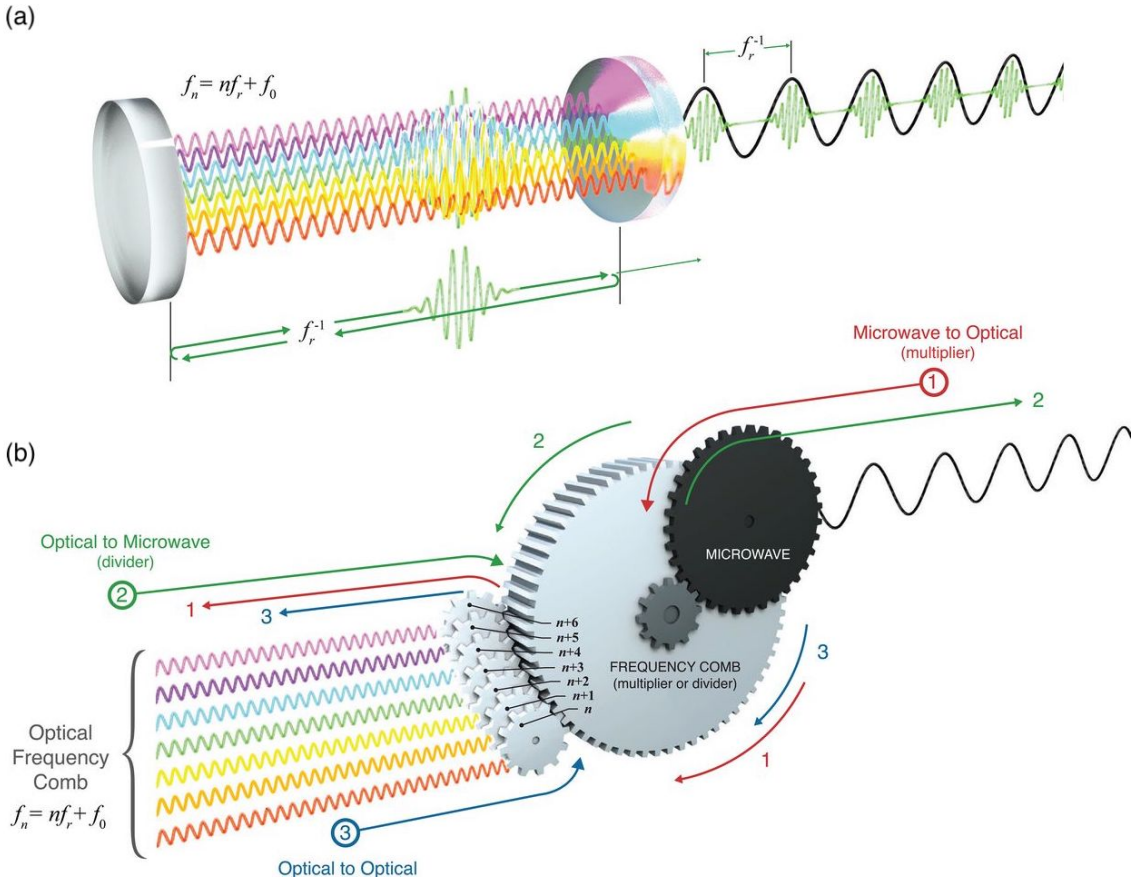

Figure 3.2. The frequency comb to link ratio frequency to optical frequency acting as an optical clockwork, reprinted from [135].

FCs were developed initially to measure and count the optical frequencies in terms of the hyperfine transition frequency of Cs from SI defining constants, which are important in precision spectroscopy, frequency metrology, and clocks [136, 137]. Three main methods can be employed to generate the optical FC: mode-lock laser FCs [138–143], electro-optic FCs [144–147], and microresonator FCs [148–154]. With the developments of optical FCs in the last 20 years, diverse applications have been found, and interlaced technologies have been utilized [135]. Nonlinear optical processes have already extended the range of FCs across from terahertz (THz) [155, 156] and mid-infrared (MIR) domains [157, 158], and up to ultraviolet (XUV) [140–143]. Nanoscale waveguide technology has provided a procedure

to build FCs at wafer scale [148, 153], which is capable of advanced photonic integrated circuits.

In our experiment, we utilized the mode lock laser FC based on the Ytterbium (Yb) doped fiber for MIR FC generation. The system consists of two parts: oscillator and amplifiers as illustrated in the Yb:fiber FC block of Figure 3.1. The oscillator was based on a Fabry-Pérot (FP) cavity, with a semiconductor saturable absorber mirror (SA) attached to PZT1 at one end and a fiber Bragg grating (FBG) for dispersion compensation at the other end [159]. The mode-locking was initialized and stabilized by the SA and the nonlinear polarization rotation (NPR) through adjusting the quarter waveplate and polarizer. The oscillator generated around 100 mW optical pulse at 1050 nm with a repetition rate of 150 MHz and pulse duration of 60 fs. Three parts were separated and amplified from the output of the oscillator for the optical beat (amp. 1 in Figure 3.1), the self-referencing (amp. 2 in Figure 3.1), and the difference frequency generation (amp. 3 in Figure 3.1). The amp. 1 was based on core-pump gain fiber, the amp. 2 and amp. 3 were based on the double-cladding pumped gain fibers, which generate an optical pulse with 130 fs pulse duration and 1.5 W output power by chirped pulse amplification [160].

3.1.1 Stabilization of the frequency comb

The FC structure in the frequency domain has two degrees of freedom controlled by the repetition rate f_r, and the carrier-to-envelop offset frequency f_o. The stabilization of the FC was realized by locking f_r and f_o separately with phase-locked loops (PLLs) [161]. Optical heterodyne detection was applied to lock one of the comb modes to a stable continuous wave (CW) reference laser (Coherent Mephisto) by detecting the beat note signal f_{beat} whose phase was compared with RF2. The fast feedback and slow feedback from PLL2 were accomplished respectively by PZT2 and PZT3, since both of them controlled the length of the FP cavity, and hence the f_r of the laser. A $f-2f$ interferometer [162] was performed to lock the f_o by detecting the f_o beat note whose phase was compared with RF3. The fast feedback and slow feedback from PLL3 were accomplished by adjusting the current of the pump diode and the temperature of the FBG, respectively. With both f_{beat} and f_o locked, the whole FC structure was fixed.

Considering that the frequency change of the CW reference laser was transferred to the change of repetition rate because of the stabilized f_{beat}, the repetition rate signal from the heterodyne detection was filtered out and utilized in the stabilization of the CW reference laser to control the FC structure. PLL1 was performed to generate the error signals between the f_r signal and RF1. The temperature controller and the PZT1 of the reference laser provided slow and fast feedback. The long-term stabilization of the radio frequency generators was performed via a GPS-locked rubidium clock, which provides the 10 MHz references for RF1, RF2 and RF3.

3.2 Mid-infrared comb from difference frequency generation

Coherent MIR light sources offer the possibility to determine molecular fingerprints, which are important in breath analysis, atmospheric measurements, astrochemistry, and astrophysics. Nonlinear frequency conversion provides a powerful tool to generate a laser source which the spectral range is not covered by laser gain media. Several techniques offer ways to transfer the established laser technologies to MIR. Among them, the optical parametric oscillator (OPO) [158, 163, 164], optical parametric amplification (OPA) [165], and difference frequency generation (DFG) [166–168] are widely applied.

We performed the DFG in our experiment since the carrier-to-envelop offset was zero [168] as schematically shown in the MIR DFG FC block of Figure 3.1. The output of amp. 3 for MIR FC generation was separated into two parts, which served as the pump pulse and generate the signal pulse for the DFG process, respectively. The signal pulse was realized by selecting the longest wavelength Raman soliton in a highly-nonlinear suspended-core fiber (HNLF) [169]. The core of HNLF was around 2 µm in diameter and surrounded by six air holes. The spectrum of the signal pulse can be tuned from 1.2 µm to 1.6 µm by controlling the coupled power. The pump and signal pulse were combined with a dichroic mirror and overlapped with waist diameters of 180 µm and 116 µm in a fan-out periodically poled lithium niobate (PPLN) crystal (HCPhotonics) for generating the MIR FC. The center wavelength of MIR frequency can be adjusted by alternating the power to the highly nonlinear fiber, changing the lateral position of the PPLN crystal, and tuning the pump–signal temporal overlap. The output MIR spectra ranging from 3 µm to 5.5 µm was realized in our experiment [170].

3.2.1 Intensity noise of the mid-infrared comb

For absorption spectroscopy with MIR FC, the long-term stability of the DFG process and the high signal-to-noise ratio (SNR) of the spectra are important. The relative intensity noise (RIN) of MIR FC were connected strongly with the pump-signal temporal overlap in the nonlinear crystal [170]. To realize long-term stability and low RIN, we applied a dither-lock scheme by modulating the PZT in the delay stage with 200 nm of total path length at 200 Hz. The detection of the MIR RIN power was performed by amplifying the interference signal from the Fourier transform spectrometer (FTS) with a demodulating logarithmic amplifier (DLA) [171]. In order to detect MIR power, MIR RIN, and the FTS signal at the same time, different band-pass filters were applied for MIR power measurement with spectral ranges from DC to 10 Hz, RIN measurement with 1 kHz to 30 kHz, and the FTS output signal with 100 kHz to 500 kHz.

3.3 Experimental gas circuit

The experimental gas circuit is shown in Figure 3.1. A pump station (HiCube 80 Eco) was used to remove air from the gas circuit and tuned the pressure of the gas sample in the gas cell. The pressure measurement of the sample was achieved by two calibrated ceramic capacitance gauges covering different pressure ranges: Pfeiffer CMR 361 from 0.1 mbar to 1000 mbar, and Pfeiffer CMR 364 from 10^{-4} mbar to 1.1 mbar. Nitrogen was used to get rid of the contamination with laboratory air by pumping the nitrogen three times to vacuum. The ammonia sample (Linde HiQ 6.0) was loaded to the gas cell after removing the contamination. The gas cell had two view ports with wedge CaF_2 windows, which allowed the transmission from visible to MIR and avoid the etalon effect.

3.3.1 Optical path length measurement

To retrieve the line intensities for different transitions, the optical path length through the gas sample was measured by using low-coherence interferometry [172]. The principle was to measure the interference signal between the reflected light from the two gas cell windows and a reference pulse as shown in Figure 3.3. The residual 1050 nm laser from DFG process served as the input signal and the gas cell was pumped to vacuum with pressure less than 4×10^{-4} mbar. Two fiber couplers with a 50% splitting ratio were used for balanced detection, and the second coupler acted as the beam splitter of a Michelson

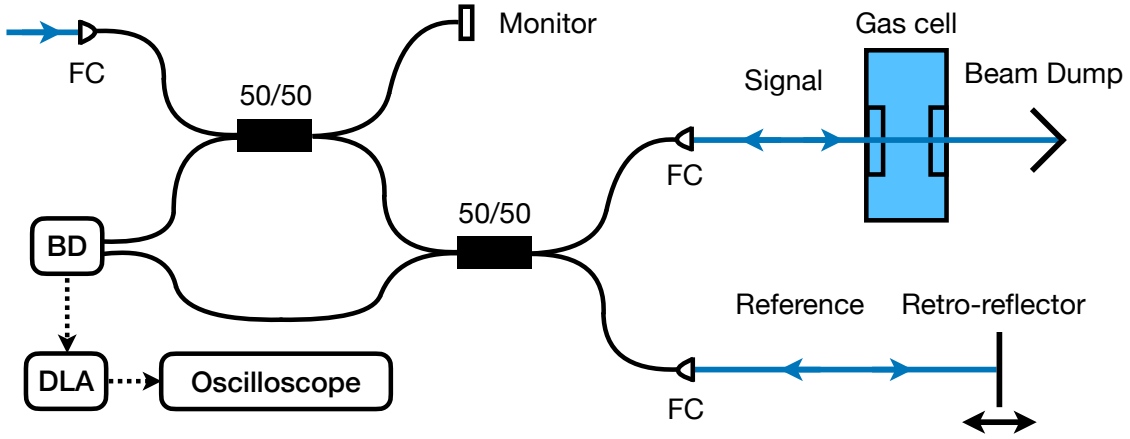

Figure 3.3. Experimental setup for lower coherence interferometer. The following abbreviations are used: FC, fiber collimator; BD, balanced detector; DLA, demodulating logarithmic amplifier.

interferometer. The reference arm of the interferometer was reflected by the retro-reflector in a 1 m translational stage. The interference signal was detected with an InGaAs balanced detector (Thorlabs PDB450C) and a DLA. Four reflections are detected and a parabola fit was used to calculate the interference signal. After measuring the optical path differences (OPDs) between the two inside surfaces of the windows 20 times, the optical path length was finally determined with the mean value of 35.4646 mm and the standard deviation of 0.0012 mm.

3.4 Fourier transform spectrometer based on the mid-infrared frequency comb

FTS is based on a Michelson interferometer, and the nominal resolution of the FTS is inversely proportional to the maximum OPD. FTS with incoherent broadband sources such as lamps, LED, and Globars, was developed in the 1950s and has been applied in many aspects of research [173–175]. Due to the low spatial coherence and brightness, incoherent light sources have limitations at high resolutions, long optical paths, and high sensitivity [176]. Long OPD is necessary to achieve high resolution, and high-resolution FTSs, especially the nine-chamber Bruker IFS 125HR system with maximum OPD around 9.8 m, are common to find in synchrotron light sources [177]. For more details about FTS, I recommend the textbook [176].

FCs provide advantages for FTS with high resolution, high sensitivity, and high SNR over a broadband range owing to the high spectral brightness, and spatial and temporal coherence [158, 163, 164, 178–181]. According to the Nyquist-Shannon sampling theorem, the sampling frequency of the FTS should be two times higher than the FC mode spacing. The maximum OPD should be $2c/f_{rep}$ =4 m to observe 3 fringes with the nominal resolution of 75 MHz. In order to realize 4 m OPD, we performed retro-reflectors to move both arms of the interferometer on a 1 m long translational stage as illustrated in Figure 3.1. The Michelson interferometer started from the beam splitter (BS). The transmitted arm and reflected arm are illustrated with dark pink and light pink arrows, respectively. The retroreflectors were moved with the OPD-changed speed of 500 mm/s for spectra measurements. The beams from both arms went through two liquid-nitrogen-cooled indium antimonide (InSb) detector (InfraRed Associates IRA 20-00060) for balanced detection. Balanced detection is

a well-established technique that can efficiently suppress noise [182, 183]. The principle of balanced detection is subtracting the currents before amplification, which suppresses the in-phase components of the signal. The transimpedance amplifier (TIA) was used for amplifying the interference signal with a gain to be approximately 70 dB to 100 dB. Since the intense central fringe saturated the detection system, the gain of TIA was reduced by a factor of 5. The interference signals were digitized by a computer-controlled data acquisition board (National Instruments PCI-5922) with the 24 bits resolution at a low sampling rate of 500 kSa/s, and the 16 bits resolution at a higher rate of 15 MSa/s.

3.4.1 Calibration absolute frequency with reference laser

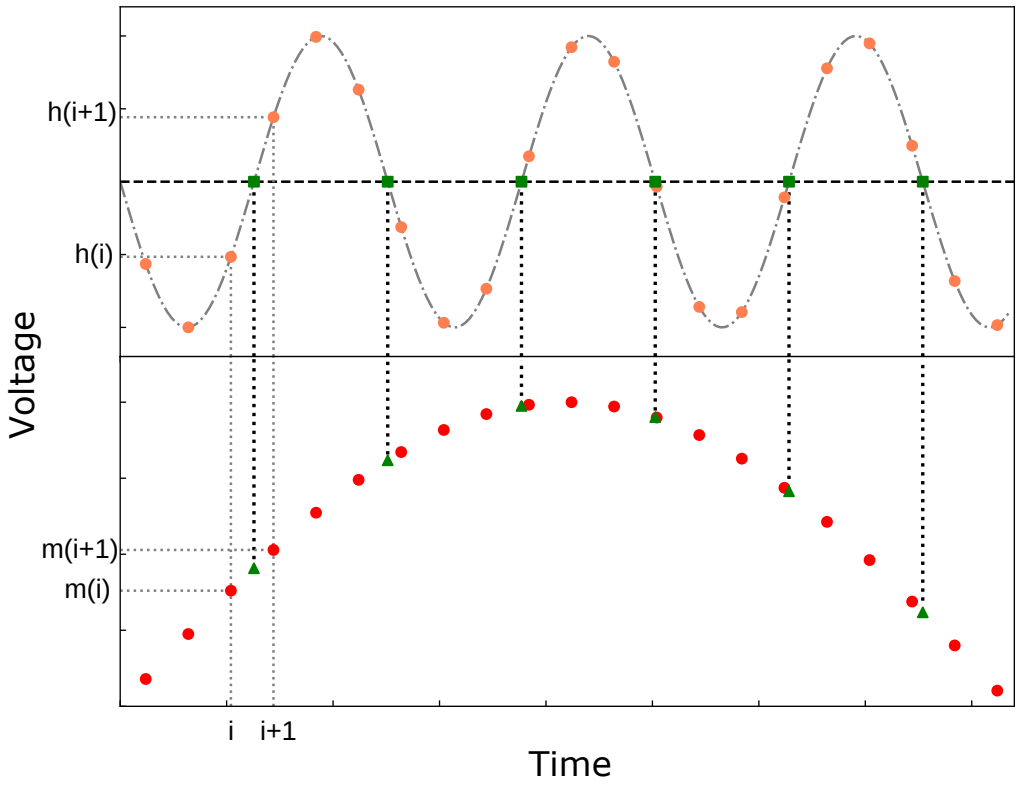

Figure 3.4. Resampling MIR interfeorogram with zeor-crossings from the HeNe laser interferogram.

The correct calculation of the frequency information needs the interferogram to be sampled at equidistant steps. A frequency stabilized helium-neon (HeNe) laser (SIOS SL4) was used as a reference for calibrating the OPD with a wavelength of 632.9909178 nm and a corresponding frequency 473612436.6MHz. The absolute frequency stability is 1 MHz over one hour. The HeNe laser was aligned with MIR FC before the gas cell. This monochromatic HeNe laser produced a sinusoidal interferogram serving as an equidistant grid for resampling the MIR at equal OPD intervals by determining the positions of the zero-crossings. The simplified resampling procedure is shown in Figure 3.4. The indices of data points before and after the first zero-crossing are denoted by i and i+1. The intensities of the interferogram with the corresponding indices are h(i) and h(i+1), m(i) and m(i+1) for HeNe laser and MIR FC, respectively. The equation to calculate the interpolated points

at the fixed OPD step corresponding to half of the HeNe laser wavelength is given by

$$res = m(i) - \frac{h(i)}{h(i) - h(i+1)} \big(m(i) - m(i+1)\big). \tag{3.2}$$

The number of point to realize the resolution of f_r is given by

$$N_0 = \frac{2c}{\lambda_{ref} f_{rep}} = \frac{2c}{\lambda_{vac} f_{rep}} \frac{n_{HeNe}}{n_{mir}} \approx 6300552, \tag{3.3}$$

here n_{HeNe} and n_{mir} are the calculated refractive indices of air for HeNe laser and MIR FC based on the equations in [184]. Due to the discrete sampling of the interferogram, it is necessary to round N_0 to the closest integer which is 6300552. To match the FTS grid exactly with the repetition rate, zero-padding the interferogram and adding a frequency shift on the FTS grid were applied to reach sub-nominal resolution [185, 186]. The zero-padding approach was performed in the interferogram length by changing the number of points on the interferogram. For the frequency shift approach, a multiplication was performed on the interferogram with fixed points.

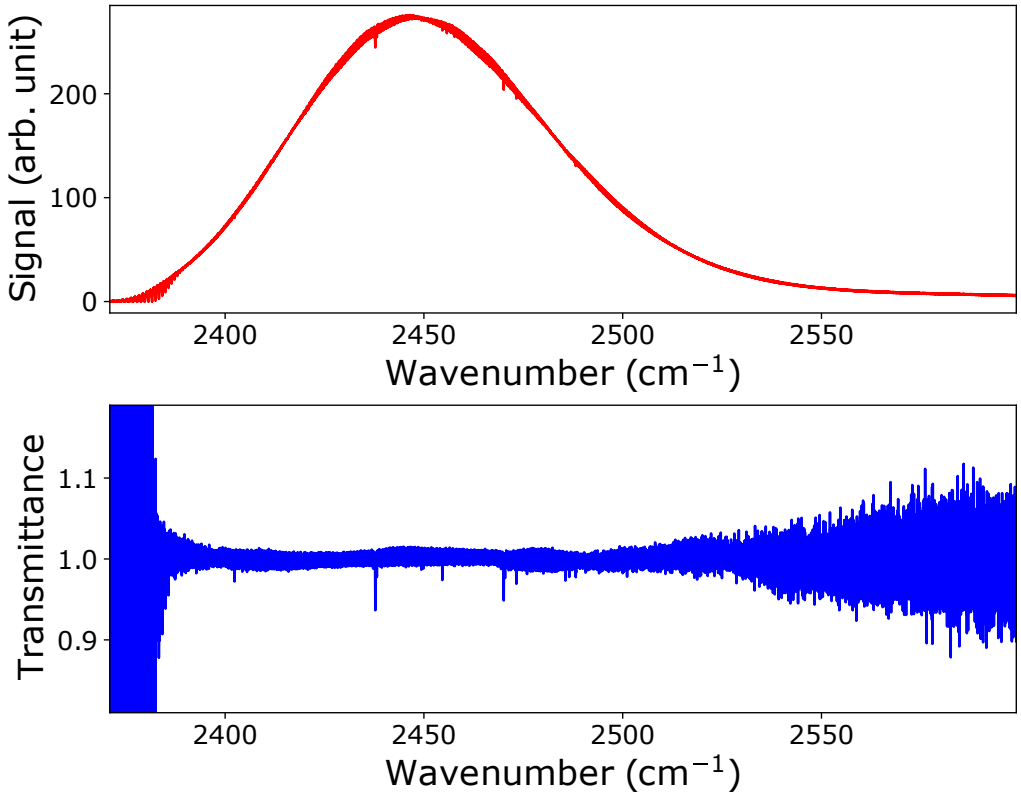

Figure 3.5. Absorption spectra of ammonia with the MIR source at 98.90 mbar and 296 K. The upper panel shows the MIR spectrum with several tiny absorption dips. After subtracting the spectra without gas sample, the transmittance is shown in the lower panel.

After performing the fast Fourier transform, we finally got the MIR spectra with absorption features for ammonia as shown in the upper panel of Figure 3.5. The spectra were recorded at 98.90 mbar and 296 K. By subtracting the MIR spectra without ammonia, we got the transmittance spectra of ammonia as shown in the lower panel of Figure 3.5. The SNR of the spectra was low due to the relatively high noise level and short absorption length. The numerical method to remove the regular signal on the noise level and the

fitting procedure to retrieve the spectra parameters are described in chapter 5.

4 The nuclear-spin-forbidden rovibrational transitions of water from first principles*

"If there is magic on this planet, it is contained in water."
— Loren Eiseley

4.1 Introduction

Water is the third most abundant molecule in the universe. It is also quite unique in that it possesses a wide range of anomalous properties, some of which may be a result of nuclear spin symmetry breaking. It has two nuclear spin isomers, *ortho*, with a total nuclear spin of hydrogen atoms $I = 1$, and *para*, with a total nuclear spin of hydrogens $I = 0$. In isolated-molecule conditions the *ortho* and *para* nuclear spin isomers show tremendously long-lasting stability to inter-conversion [38, 187], can be spatially separated [60, 61], and exhibit distinct physical and chemical properties [34, 62]. Thus the nuclear spin isomers of water are frequently treated as distinct molecular species.

The concept of stable nuclear spin isomers is appealing to astrophysicists, as it allows to deduce temperatures, below 50 K, in cometary comae, star- and planet-forming regions from the observations of relative abundance of *ortho* and *para* species [26, 28–31]. Some astronomical observations however reported anomalous *ortho-para* ratios (OPR), corresponding to spin temperatures that are much lower than gas kinetic temperatures in the same region [188–191]. These observations pose the intriguing question if the OPR values could be altered as a result of internal *ortho-para* conversion, which can possibly be enhanced by natural factors, such as molecular collisions [35, 36, 45], interaction with catalytic surfaces [192], external fields [40] and radiation [37]. Low nuclear-spin temperatures have been attributed to the photodesorption of water from colder icy grains [193]. However, this theory was benchmarked and disputed in a number of recent laboratory experiments [19, 49, 194, 195]. Arguably there could be another yet unknown mechanism of spin-non-destructive desorption of water molecules from ice.

The OPR values can change as a result of the interaction between the nuclear spins and an induced internal magnetic field of the rotating molecule, which is called the nuclear spin-rotation interaction. For the main water isotopologue $H_2^{16}O$, considered here, the ^{16}O has zero nuclear spin, and the hyperfine coupling between the spins of the protons is very weak, providing a fundamental rationale for neglecting the *ortho-para* conversion in practical applications. However, it can be significantly enhanced by accidental resonances between the *ortho* and *para*states, which are present in vibrationally excited bands of isolated water. Their coupling can be amplified by external effects such as molecular collisions and interactions with strong external fields and field gradients. The accurate modeling of these processes may unravel previously unknown mechanisms contributing to the observed anomalous OPR of water in space. Precise knowledge of the molecular hyperfine states and corresponding transitions is mandatory for the understanding of such conversion mechanisms. This information can also be important for cold-molecule precision spectroscopy relying on controlled hyperfine transitions and hyperfine-state changing collisions [196].

Here, we report a complete linelist of rovibrational hyperfine transitions in $H_2{}^{16}O$ at room-

*This chapter is based on the publication: "*The nuclear-spin forbidden rovibrational transitions of water from first principles*" by Andrey Yachmenev, Guang Yang, Emil Zak, Sergei Yurchenko, and Jochen Küpper, *J. Chem. Phys.* **156**, 204307 (2022), arXiv:2203.07945 [physics]. I contributed to the theory derivation checking, computation of the linelist, preparation of figures, and writing the results and discussion part of the manuscript.

temperature that we computed using an accurate variational approach [72, 73, 115, 197] with an empirically refined potential energy surface (PES) [198] and a high-level *ab initio* spin-rotation tensor surface. The spin-spin coupling was modelled as the magnetic dipole-dipole interaction between the two hydrogen nuclei. We show that the strongest forbidden *ortho-para* transitions are on the order of 10^{-31} cm/molecule, which is about ten times stronger than previously reported calculations for the same lines [187]. We also present the details of our variational approach for computing hyperfine effects, which is general and not restricted by the numbers and specific magnitudes of the molecules' nuclear spins.

4.2 Theoretical details

4.2.1 Spin-rotation and spin-spin coupling

In this section we describe the implementation of the nuclear spin-rotation and spin-spin coupling terms within the general variational framework of the nuclear motion approach TROVE [72, 73, 115, 197]. Implementation details of the hyperfine nuclear quadrupole coupling can be found in our previous works [199, 200].

The spin-rotation coupling is the interaction between the rotational angular momentum $\mathbf{J}$ of the molecule and the nuclear spins $\mathbf{I}_n$ of different nuclei [201]

$$H_{\rm sr} = \sum_{n}^{N_I} \mathbf{I}_n \cdot \mathbf{M}_n \cdot \mathbf{J}, \tag{4.1}$$

where $\mathbf{M}_n$ is the second-rank spin-rotation tensor relative to the nucleus n and the sum runs over all nuclei N_I with non-zero spin. The interaction between the nuclear spins $\mathbf{I}_n$ of different nuclei is given by the spin-spin coupling as

$$H_{\rm ss} = \sum_{n>n'}^{N_I} \mathbf{I}_n \cdot \mathbf{D}_{n,n'} \cdot \mathbf{I}_{n'}, \tag{4.2}$$

where $\mathbf{D}_{n,n'}$ is the second-rank spin-spin tensor, which is traceless and symmetric. Using the spherical-tensor representation [79], the spin-rotation and spin-spin Hamiltonians can be expressed as

$$\begin{aligned} H_{\rm sr} = & \frac{1}{2} \sum_{n}^{N_I} \sum_{\omega=0}^{2} \sqrt{2\omega+1} \left(-\frac{1}{\sqrt{3}} \right) \mathbf{I}_n^{(1)} \\ & \cdot \left((-1)^{\omega} \left[\mathbf{M}_n^{(\omega)} \otimes \mathbf{J}^{(1)} \right]^{(1)} + \left[\mathbf{J}^{(1)} \otimes \mathbf{M}_n^{(\omega)} \right]^{(1)} \right) \end{aligned} \tag{4.3}$$

and

$$H_{\rm ss} = \sum_{n>n'}^{N_I} \mathbf{D}_{n,n'}^{(2)} \cdot \left[\mathbf{I}_n^{(1)} \otimes \mathbf{I}_{n'}^{(1)} \right]^{(2)}, \tag{4.4}$$

where $\mathbf{M}_n^{(\omega)}$, $\mathbf{D}_{n,n'}^{(2)}$, $\mathbf{J}^{(1)}$, and $\mathbf{I}_n^{(1)}$ denote the spherical-tensor representations of operators in (4.1) and (4.2) and the square brackets are used to indicate the tensor product of two spherical-tensor operators. Because the spin-rotation tensor is generally not symmetric, the second term in the sum (4.3) is added to ensure that the Hamiltonian is Hermitian.

The nuclear-spin operator $\mathbf{I}_n$ and the rotational-angular-momentum operator $\mathbf{J}$ are coupled using a *nearly-equal* coupling scheme, i. e., $\mathbf{I}_{1,2} = \mathbf{I}_1 + \mathbf{I}_2$, $\mathbf{I}_{1,3} = \mathbf{I}_{1,2} + \mathbf{I}_3$, ..., $\mathbf{I} \equiv \mathbf{I}_{1,N} = \mathbf{I}_{1,N-1} + \mathbf{I}_N$, and $\mathbf{F} = \mathbf{J} + \mathbf{I}$. The nuclear-spin functions $|I, m_I, \mathcal{I}\rangle$ depend on the

quantum numbers I and m_I of the collective nuclear-spin operator $\mathbf{I}$ and its projection onto the laboratory Z axis, respectively. The set of auxiliary quantum numbers $\mathcal{I} = \{I_1, I_{1,2}, I_{1,3}, \ldots, I_{1,N-1}\}$ for the intermediate spin angular momentum operators provide a unique assignment of each nuclear-spin state. The total spin-rovibrational wave functions $|F, m_F, u\rangle$ are built as symmetry-adapted linear combinations of the coupled products of the rovibrational wave functions $|J, m_J, l\rangle$ and the nuclear-spin functions $|I, m_I, \mathcal{I}\rangle$. Here, J and F are the quantum numbers of $\mathbf{J}$ and $\mathbf{F}$ operators with m_J and m_F of their Z-axis projections. l and u denote the rovibrational and hyperfine state indices, respectively, and embrace all quantum numbers, e. g., rotational k and vibrational quantum numbers $v_1, v_2, \ldots$, that are necessary to characterize a nuclear spin-rovibrational state.

The symmetrization postulate requires the total wavefunction of the H_2O molecule to change sign upon exchange of the protons, i. e., to transform as one of the irreducible representations B_1, B_2 of its $\mathbf{C}_{2v}(M)$ symmetry group. Accordingly, the *ortho* spin state $|I = 1\rangle$ of A_1 symmetry can be coupled with the rovibrational states of B_1 and B_2 symmetries and the *para* state $|I = 0\rangle$ of B_2 symmetry can be coupled with the rovibrational states of A_1 and A_2 symmetries.

The matrix representations of the spin-rotation and spin-spin Hamiltonians in the basis of the $|F, m_F, u\rangle$ functions are diagonal in F and m_F, with the explicit expressions given by

$$\begin{aligned}\langle F, m_F, u'|H_{\mathrm{sr}}|F, m_F, u\rangle =& \frac{1}{2}(-1)^{I+F}\sqrt{(2J+1)(2J'+1)}\begin{Bmatrix} I' & J' & F \\ J & I & 1 \end{Bmatrix} \\ &\times \sum_{n}^{N_I}\sum_{\omega=0}^{2} N_\omega \left[(-1)^{\omega} J \begin{Bmatrix} \omega & 1 & 1 \\ J & J' & J \end{Bmatrix} \begin{pmatrix} J & 1 & J \\ -J & 0 & J \end{pmatrix}^{-1}\right. \\ &\left. + J' \begin{Bmatrix} 1 & \omega & 1 \\ J & J' & J' \end{Bmatrix} \begin{pmatrix} J' & 1 & J' \\ -J' & 0 & J' \end{pmatrix}^{-1}\right] \\ &\times \mathcal{M}_{\omega,n}^{(J'l',Jl)} \langle I'||\mathbf{I}_n^{(1)}||I\rangle\end{aligned} \tag{4.5}$$

and

$$\begin{aligned}\langle F, m_F, u'|H_{\mathrm{ss}}|F, m_F, u\rangle =& (-1)^{I+J'+J+F}\sqrt{(2J+1)(2J'+1)}\begin{Bmatrix} I' & J' & F \\ J & I & 2 \end{Bmatrix} \\ &\times \sum_{n>n'}^{N_I} \mathcal{D}_{n,n'}^{(J'l',Jl)} \langle I'||[\mathbf{I}_n^{(1)} \otimes \mathbf{I}_{n'}^{(1)}]^{(2)}||I\rangle,\end{aligned} \tag{4.6}$$

with the normalization constant $N_\omega = 1$, $-\sqrt{3}$, and $\sqrt{5}$ for $\omega = 0$, 1, and 2, respectively. The expressions for the reduced matrix elements of the nuclear-spin operators $\langle I'||\mathbf{I}_n^{(1)}||I\rangle$ and $\langle I'||[\mathbf{I}_n^{(1)} \otimes \mathbf{I}_{n'}^{(1)}]^{(2)}||I\rangle$ depend on the total number of coupled spins and can be computed using a general recursive procedure as described, for example, in [199]. Here, for the two

equivalent hydrogen spins $I_1 = I_2 = 1/2$, the reduced matrix elements are

$$\begin{aligned}\langle I'||\mathbf{I}_n^{(1)}||I\rangle =&(-1)^{I\delta_{n,1}+I'\delta_{n,2}} I_1\sqrt{(2I+1)(2I'+1)}\\ &\times\begin{Bmatrix} I_1 & I' & I_1\\ I & I_1 & 1\end{Bmatrix}\begin{pmatrix} I_1 & 1 & I_1\\ -I_1 & 0 & I_1\end{pmatrix}^{-1},\end{aligned} \tag{4.7}$$

with the explicit values $\langle 0||\mathbf{I}_n^{(1)}||0\rangle = 0$, $\langle 1||\mathbf{I}_n^{(1)}||1\rangle = \sqrt{3/2}$, $\langle 0||\mathbf{I}_n^{(1)}||1\rangle = \pm\sqrt{3}/2$ for $n = 1$ and 2, respectively, and $\langle 1||\mathbf{I}_n^{(1)}||0\rangle = \mp\sqrt{3}/2$.

The expressions for the $\mathcal{M}_{\omega,n}^{(J'l',Jl)}$ and $\mathcal{D}_{n,n'}^{(J'l',Jl)}$ tensors in Eqs. (4.5) and (4.6) depend on the chosen rovibrational wave functions $\left|J,m_J,l\right\rangle$, which are represented by the molecular rovibrational eigenfunctions calculated with the variational approach TROVE. The functions $\left|J,m_J,l\right\rangle$ are linear combinations of products of vibrational wave functions $|v\rangle = |v_1,v_2,\ldots,v_M\rangle$ (M is the number of vibrational modes) and symmetric-top rotational functions

$$|J,m_J,l\rangle = \sum_{v,k} c_{v,k}^{(J,l)}\,|v\rangle\left|J,k,m_J\right\rangle. \tag{4.8}$$

In this basis, the $\mathcal{M}_{\omega,n}^{(J'l',Jl)}$ and $\mathcal{D}_{n,n'}^{(J'l',Jl)}$ tensors are

$$\begin{aligned}\mathcal{M}_{\omega,n}^{(J'l',Jl)} =&\sum_{v'k'}\sum_{vk}\left[c_{v'k'}^{(J',l')}\right]^* c_{vk}^{(J,l)}\,(-1)^{k'}\\ &\times\sum_{\sigma=-\omega}^{\omega}\sum_{\alpha,\beta=x,y,z}\begin{pmatrix} J & \omega & J'\\ k & \sigma & -k'\end{pmatrix} U_{\omega\sigma,\alpha\beta}^{(2)}\langle v'|\bar{M}_{\alpha\beta,n}|v\rangle\end{aligned} \tag{4.9}$$

and

$$\begin{aligned}\mathcal{D}_{n,n'}^{(J'l',Jl)} =&\sum_{v'k'}\sum_{vk}\left[c_{v'k'}^{(J',l')}\right]^* c_{vk}^{(J,l)}\,(-1)^{k'}\\ &\times\sum_{\sigma=-2}^{2}\sum_{\alpha,\beta=x,y,z}\begin{pmatrix} J & 2 & J'\\ k & \sigma & -k'\end{pmatrix} U_{2\sigma,\alpha\beta}^{(2)}\langle v'|\bar{D}_{\alpha\beta,nn'}|v\rangle\end{aligned} \tag{4.10}$$

where $\bar{M}_{\alpha\beta,n}$ and $\bar{D}_{\alpha\beta,nn'}$ ($\alpha,\beta = x,y,z$) are spin-rotation and spin-spin interaction tensors in the molecule-fixed frame and the 9×9 constant matrix $U_{\omega\sigma,\alpha\beta}^{(2)}$ ($\omega = 0,\ldots,2$, $\sigma = -\omega,\ldots,\omega$) defines the transformation of a general second-rank Cartesian tensor operator into its spherical-tensor representation, see, e. g., (5.41)–(5.44) in [79].

The total Hamiltonian H is composed of a sum of the pure rovibrational Hamiltonian $H_{\rm rv}$ and hyperfine terms $H_{\rm sr}$ and $H_{\rm ss}$. In the basis of TROVE wave functions, the rovibrational Hamiltonian $H_{\rm rv}$ is diagonal, its elements are given by the rovibrational energies

$$\begin{aligned}\langle F,m_F,u'|H|F,m_F,u\rangle =&E_u\delta_{u,u'} + \langle F,m_F,u'|H_{\rm sr}|F,m_F,u\rangle\\ &+\langle F,m_F,u'|H_{\rm ss}|F,m_F,u\rangle,\end{aligned} \tag{4.11}$$

where $\delta_{u,u'} = \delta_{J,J'}\delta_{l,l'}\delta_{I,I'}\delta_{\mathcal{I},\mathcal{I}'}$.

The above equations were implemented in the `hyfor` module of the Python software package Richmol [202, 203], which uses rovibrational molecular states calculated in TROVE as a variational basis. Alternative approaches using Watson-type effective Hamiltonians [204]

are also implemented in the Richmol package.

The hyperfine energies and wave functions are computed in a three step procedure. First, we solve the full rovibrational problem using TROVE and obtain the rovibrational energies and wave functions for all states with energies below a selected threshold. In the next step, the rovibrational matrix elements of the spin-rotation and spin-spin tensors are computed in the form given by Eqs. (4.9) and (4.10). These matrix elements are later used to build the spin-rotation and spin-spin interaction Hamiltonians using Eqs. (4.5) and (4.6). The total Hamiltonian is composed of the sum of a purely rovibrational part, which is diagonal and given by the rovibrational state energies, and non-diagonal spin-rotation and spin-spin parts. In the final step, the hyperfine energies and wave functions are obtained by diagonalizing the total Hamiltonian.

The computation of the dipole transition intensities also proceeds in two steps. First, the rovibrational matrix elements of the dipole moment surface are computed and cast into a tensor form similar to (4.10),

$$\begin{aligned}\mathcal{K}_{\omega}^{(J'l',Jl)} = &\sum_{\nu'k'}\sum_{\nu k}\left[c_{\nu'k'}^{(J',l')}\right]^{*} c_{\nu k}^{(J,l)}\,(-1)^{k'} \\ &\times \sum_{\sigma=-\omega}^{\omega}\sum_{\alpha,\beta=x,y,z}\begin{pmatrix} J & \omega & J' \\ k & \sigma & -k' \end{pmatrix} U_{\omega\sigma,\alpha}^{(1)}\langle\nu'|\bar{\mu}_{\alpha}|\nu\rangle,\end{aligned} \tag{4.12}$$

where $\bar{\mu}_{\alpha}$ ($\alpha = x,y,z$) is the permanent dipole moment in the molecule-fixed frame and the 3×3 constant matrix $U_{\omega\sigma,\alpha}^{(1)}$ ($\omega = 1$, $\sigma = -\omega,\ldots,\omega$) defines the transformation of a general first-rank Cartesian tensor operator into its spherical-tensor representation, see, e. g., (5.4) in [79]. In the second step, the dipole matrix elements are transformed into the basis of hyperfine wave functions, i. e.,

$$\begin{aligned}\mathcal{K}_{\omega}^{(F',u',F,u)} = &\sum_{I',\mathcal{I}',J',l'}\sum_{I,\mathcal{I},J,l}\left[c_{I',\mathcal{I}',J',l'}^{(F',u')}\right]^{*} c_{I,\mathcal{I},J,l}^{(F,u)}(-1)^{I} \\ &\times\sqrt{(2J'+1)(2J+1)}\begin{Bmatrix} J' & F' & I \\ F & J & \omega \end{Bmatrix}\mathcal{K}_{\omega}^{(J',l',J,l)}\delta_{I',I}\delta_{\mathcal{I}',\mathcal{I}},\end{aligned} \tag{4.13}$$

where $c_{I,\mathcal{I},J,l}^{(F,u)}$ are hyperfine wave function coefficients obtained by diagonalization of the total Hamiltonian. Finally, the line strengths for transitions between hyperfine states $|f\rangle = |F',u'\rangle$ and $|i\rangle = |F,u\rangle$ are computed as [200]

$$S(f\leftarrow i) = (2F'+1)(2F+1)\left|\mathcal{K}_{1}^{(F'u',Fu)}\right|^{2}, \tag{4.14}$$

where we sum over all degenerate m_F and m_F' components. The expression for the integrated absorption coefficient of the dipole transition in units of cm/molecule reads

$$I(f\leftarrow i) = \frac{8\pi^{3}\nu_{if}e^{-hcE_i/kT}\left(1-e^{-hc\nu_{if}/kT}\right)}{3hcZ(T)}S(f\leftarrow i), \tag{4.15}$$

where $\nu_{if} = |E_i - E_f|$ is the transition wavenumber, E_i and E_f are energy term values of the initial and final states in cm^{-1}, $Z(T)$ is the temperature dependent partition function, h (erg·s) is the Planck constant, c (cm/s) is the speed of light and k (erg/K) is the Boltzmann constant.

4.2.2 Electronic structure calculations

The molecule-fixed frame spin-rotation tensors $\bar{M}_{\alpha\beta,n}$ ($\alpha,\beta = x,y,z$, $n = 1,2$) were calculated *ab initio* on a grid of 2000 different molecular geometries with electronic energies ranging up to 30 000 cm^{-1} above the equilibrium energy. We used the all-electron CCSD(T) (coupled-cluster singles, doubles, and perturbative triples) method with the augmented core-valence correlation-consistent basis set aug-cc-pwCVTZ [101] and aug-cc-pVTZ [99, 100] for the oxygen and hydrogen atoms, respectively. The basis sets were downloaded from the Basis Set Exchange library [205–207]. The calculations employed second-order analytical derivatives [208] together with the rotational London orbitals [209, 210], as implemented in the quantum chemistry package CFOUR [211].

The electronic structure calculations used the principal axes of inertia coordinate frame. For variational calculations another frame was employed, defined such that the x axis is parallel to the bisector of the valence bond angle with the molecule lying in the xz plane at all instantaneous molecular geometries. In this frame, the z axis coincides with the molecular axis at the linear geometry. The computed spin-rotation tensors were rotated from the principal axis of inertia to the new frame. The permutation symmetry is such, that exchange of the two hydrogen atoms transforms $\bar{M}_{\alpha\beta,1}$ into $\bar{M}_{\alpha\beta,2}$ followed by a sign change for non-diagonal elements ($\alpha \neq \beta$).

The expression for the spin-rotation tensor, as computed in CFOUR, contains multiplication by the inverse of the tensor of inertia, see (3) and (7) in [210]. For linear and closely linear geometries of the molecule, the inertial tensor becomes singular, which creates a discontinuity in the dependence of xz and zz elements of spin-rotation tensor on the bending angle. To circumvent this problem, we have multiplied the computed spin-rotation tensors on the right side by the corresponding inertial tensors. The resulting data for the inertia-scaled spin-rotation tensor was parameterized through least-squares fitting, using a power series expansions to fourth order in terms of valence bond coordinates, with $\sigma_{\mathrm{rms}} \leq 0.3$ kHz for all tensor components. Later, when computing the rovibrational matrix elements of the spin-rotation tensor, we have multiplied the inertia-scaled tensor with the inverse moment of inertia. The divergence of the spin-rotation tensor in the vicinity of linear geometries is exactly canceled by the basis functions chosen to satisfy the kinetic cusp condition at the linear geometry [197, 212].

The spin-spin tensor elements were computed as magnetic dipole-dipole interaction between two hydrogen nuclei H_1 and H_2,

$$D_{\alpha\beta,12} = \frac{\mu_0}{4\pi}\frac{\mu_1\mu_2}{I_1 I_2 r_{12}^3}\left(\mathbf{I} - 3\mathbf{n}\otimes\mathbf{n}\right)_{\alpha\beta}, \tag{4.16}$$

where $\mu_1 = \mu_2 = 2.79284734$ are the magnetic dipole moments of H_1 and H_2 in units of the nuclear magneton, $I_1 = I_2 = 1/2$ are the corresponding hydrogen nuclear spins, r_{12} is the distance between the hydrogen nuclei, and $\mathbf{n}$ is the unit vector directed from one hydrogen to another. The indirect spin-spin coupling constants mediated by the electronic motions were not considered here, as they are typically two orders of magnitude smaller than the direct constants [213].

The magnitudes of the equilibrium *ab initio* spin-rotation and direct spin-spin diagonal tensor elements are about 30 and 60 kHz, respectively [214]. However, the corresponding matrix elements have different selection rules. In particular, due to the traceless-tensor nature of the spin-spin interaction, it can couple only states with $|J - J'| = 2$, see (4.6) and (4.10). The spin-rotation interaction can in principle couple states with $|J - J'| \leq 2$, where the *ortho-para* interaction between states with $|J - J'| \leq 1$ and $|k - k'| = 1$ occurs due to antisymmetric behavior of the off-diagonal elements of the spin-rotation tensor with respect

to the proton exchange, i. e., $\bar{M}_{xz,1} = \bar{M}_{zx,2}$, see (4.5) and (4.9).

4.2.3 Nuclear motion calculations

We employed TROVE to calculate the rovibrational states using the exact kinetic-energy operator formalism recently developed for triatomic molecules [212]. This formalism is based on the use of associated Laguerre polynomials $L_n^l(x)$ as bending basis functions, which ensures a correct behavior of the rovibrational wave functions at linear molecular geometry [212]. The bisecting frame embedding was selected as a non-rigid reference frame, with the x axis oriented parallel to the bisector of the valence bond angle and the molecule placed in the xz plane. In this frame, the z axis coincides with the linearity axis at linear molecular geometry. Accurate empirically refined PES of $H_2^{16}O$ was employed [198].

The primitive-stretching vibrational basis functions were generated by numerically solving the corresponding one-dimensional Schrödinger equations on a grid of 2000 points using the Numerov-Cooley approach [124, 125]. The primitive basis functions were then symmetry-adapted to the irreducible representations of the $\mathbf{C}_{2v}(M)$ molecular symmetry group using an automated numerical procedure [73]. The total vibrational basis set was formed as a direct product of the symmetry-adapted stretching and bending basis functions, contracted to include states up to a polyad 48. It was used to solve the $J = 0$ eigenvalue problem for the complete vibrational Hamiltonian of H_2O. A product of the $J = 0$ eigenfunctions and symmetry-adapted rigid rotor wavefunctions formed the final rovibrational basis set. The rovibrational wavefunctions $|J, m_J, l\rangle$ for rotational excitations up to $J = 40$ and four irreducible representations A_1, A_2, B_1 and B_2 were computed by diagonalizing the matrix representation of the total rovibrational Hamiltonian H_{rv} in the rovibrational basis set. More details about the variational approach and the basis-symmetrization procedure for the case of triatomic molecules can be found in [212].

4.2.4 Line list simulations

The linelist of hyperfine rovibrational transitions for $H_2^{16}O$ was computed with an energy cutoff at 15000 cm^{-1} and includes transitions up to $F = 39$ ($J = 40$). To further improve the accuracy of the linelist, after solving the pure rovibrational problem and before entering the hyperfine calculations, the rovibrational energies E_u in (4.11) were replaced with the high-resolution experimental IUPAC values from [215], where available. Such empirical adjustment of the rovibrational energies have been adopted and tested, e. g., for the production of molecular linelists as part of the ExoMol project [216]. Recently, this approach was proven accurate for computing the ultra-weak quadrupole transitions in water [217, 218] and carbon dioxide [219, 220], which enabled their first laboratory (H_2O and CO_2) and astrophysical (CO_2) detection.

The final linelist has been calculated at room temperature ($T = 296$ K) with the corresponding partition function $Z = 174.5813$ [221], and a threshold of 10^{-36} cm/molecule for the absorption intensity based on (4.15). The linelist stored in the ExoMol [222] format is provided in the supplementary information.

4.3 Results and discussion

An overview of the calculated $H_2^{16}O$ dipole absorption stick spectrum at $T = 296$ K is shown in Figure 4.1. The forbidden *ortho-para* transitions are plotted as red circles. Despite being, at least, 10 orders of magnitude weaker than the corresponding allowed transitions, for someof the strongest *ortho-para* transitions the predicted absorption intensities are close to

Table 4.1: Strongest predicted *ortho-para* transitions in $H_2{}^{16}O$ at $T = 296$ K with the 10^{-31} cm/molecule intensity cutoff.

ν_1'	ν_2'	ν_3'	F'	J'	k_a'	k_c'	I'	E' (cm^{-1})	ν_1	ν_2	ν_3	F	J	k_a	k_c	I	E (cm^{-1})	Freq. (cm^{-1})	Int. (cm/molec.)
0	1	0	3	4	2	3	*o*	1908.016319	0	0	0	4	4	4	0	*p*	488.134170	1419.882149	2.26×10^{-31}
0	1	0	3	3	3	1	*p*	1907.450231	0	0	0	3	4	3	2	*o*	382.516901	1524.933330	1.36×10^{-31}
0	1	0	3	3	3	1	*p*	1907.450231	0	0	0	3	4	1	4	*o*	224.838381	1682.611850	1.12×10^{-31}
0	1	0	3	4	2	3	*o*	1908.016319	0	0	0	3	3	2	2	*p*	206.301430	1701.714889	1.02×10^{-31}
0	1	0	3	3	3	1	*p*	1907.450231	0	0	0	2	3	1	2	*o*	173.365811	1734.084420	2.05×10^{-31}
0	1	0	3	4	2	3	*o*	1908.016319	0	0	0	2	2	2	0	*p*	136.163927	1771.852392	3.28×10^{-31}
2	1	0	3	4	1	4	*o*	8979.657423	0	0	0	4	4	1	3	*p*	275.497051	8704.160372	3.36×10^{-31}
2	1	0	3	4	1	4	*o*	8979.657423	0	0	0	3	3	1	3	*p*	142.278493	8837.378930	1.01×10^{-31}
2	1	0	3	4	1	4	*o*	8979.657423	0	0	0	2	2	1	1	*p*	95.175936	8884.481487	6.41×10^{-31}
1	1	1	15	14	3	11	*o*	11067.083574	0	0	0	14	14	0	14	*p*	2073.514207	8993.569367	1.92×10^{-31}
1	1	1	15	15	2	13	*p*	11067.089122	0	0	0	14	13	1	12	*o*	2042.309821	9024.779300	2.04×10^{-31}

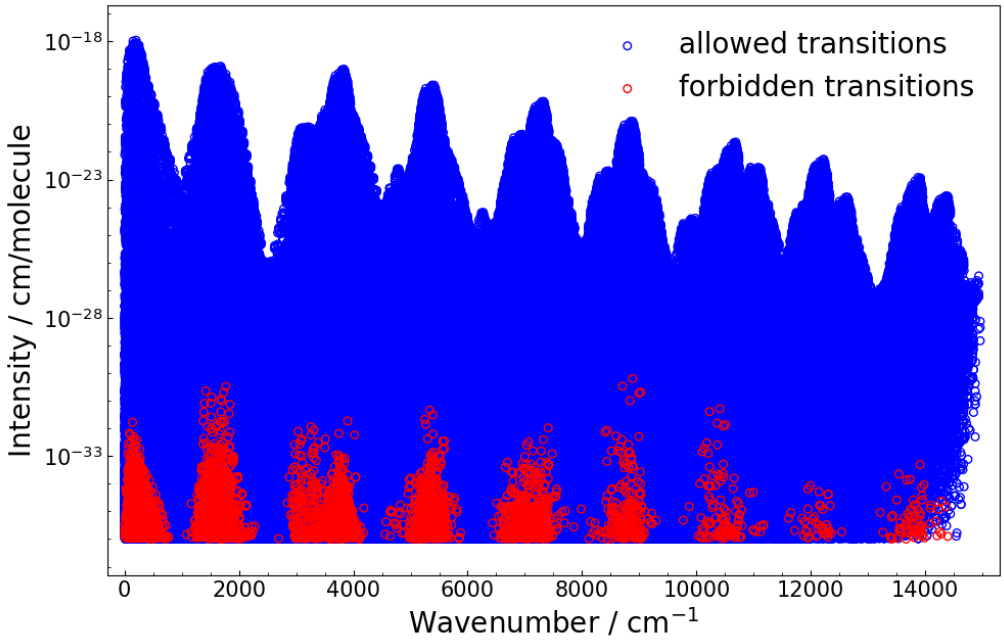

Figure 4.1. Overview of the $H_2^{16}O$ dipole absorption spectrum at $T = 296$ K. The *ortho-ortho* and *para-para* transitions are marked with blue circles, whereas the *ortho-para* transitions are given by red circles.

the sensitivity threshold of modern cavity ring-down spectroscopic techniques [224–226]. All predicted *ortho-para* transitions with line intensity larger than 10^{-31} cm/molecule are listed in Table 4.1. These transitions all occur in the fundamental ν_2 bending and the overtone $2\nu_1 + \nu_2$ and $\nu_1 + \nu_2 + \nu_3$ bands. The off-diagonal elements of molecular-frame spin-rotation tensor $\bar{M}_{\alpha\beta,n}$, which lead to *ortho-para* interaction, are highly dependent on the bending vibrational coordinate, indicating significance of the ν_2 band in *ortho-para* transitions. The size of the off-diagonal spin-rotation matrix elements increases for bending angles close to 180°, i. e., the linear geometry of the molecule. This leads to an increase in the *ortho-para* interaction for rovibrationa energies close to the linearity barrier at ∼8254 cm^{-1} above the zero-point energy. The spin-rotation coupling in these vibrationally excited states is responsible for the *ortho-para* transitions. For example, the final transition state $F = 3$, $J_{k_a,k_c} = 4_{2,3}$ (*ortho*) with energy $E = 1908.016319$ cm^{-1} is mixed with the state $F = 3$, $J_{k_a,k_c} = 3_{3,1}$ (*para*) with energy $E = 1907.450231$ cm^{-1}. The size of the rovibrational

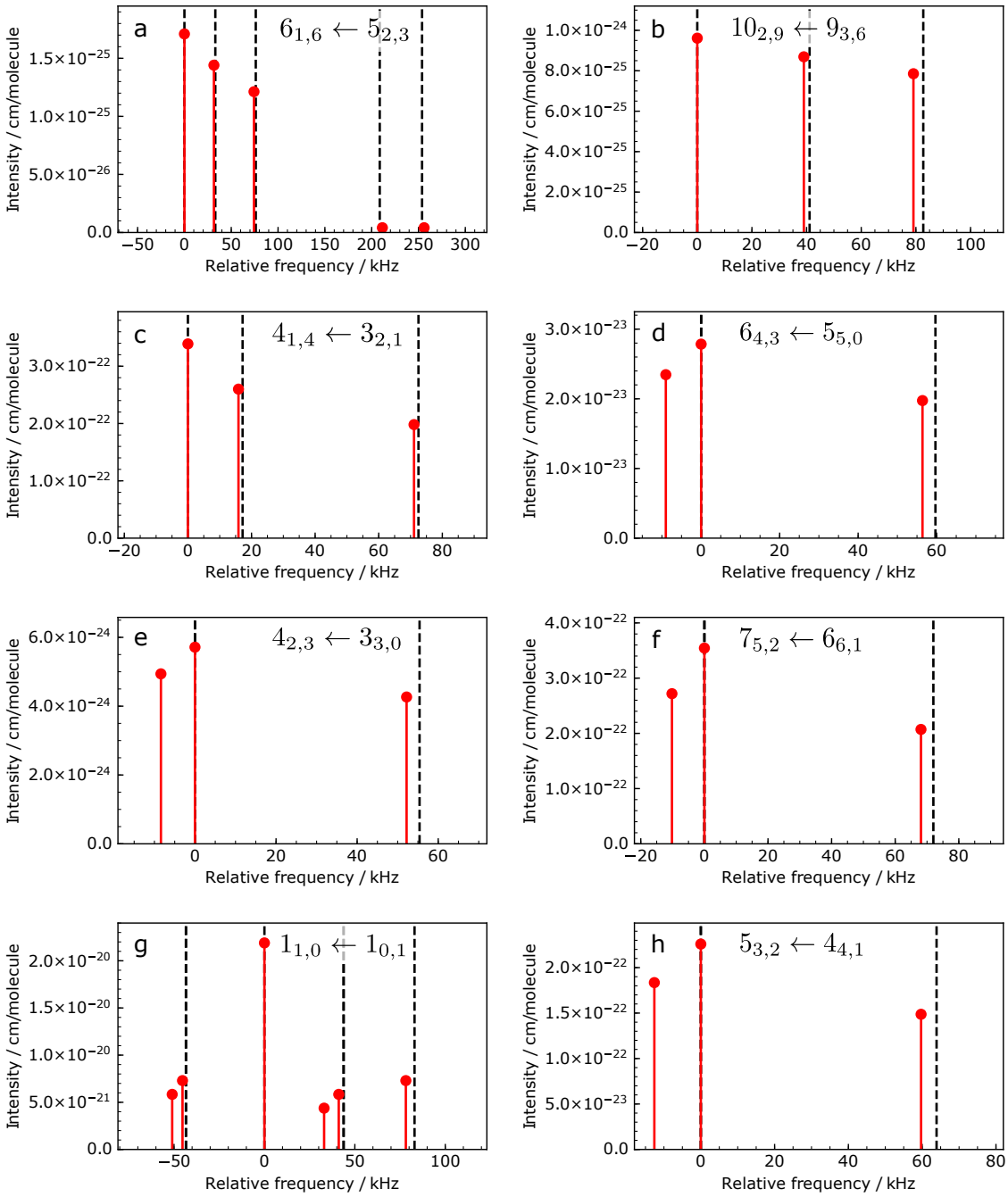

Figure 4.2. Comparison of calculated hyperfine transitions (red stems) with experimental data (dashed lines) from [223] (a) and [214] (b-h). Different panels show hyperfine transitions for different rotational bands $J'_{k'_a,k'_c} \leftarrow J_{k_a,k_c}$. The measured (calculated) zero-crossing frequencies, in MHz, are 22235.0447 (22235.0322), 321225.6363 (321225.6311), 380197.3303 (380197.3361), 439150.7746 (439150.7857), 443018.3358 (443018.4016), 448001.0538 (448001.0359), 556935.9776 (556935.9849), 620700.9334 (620700.8889) for panels (a)–(h), respectively.

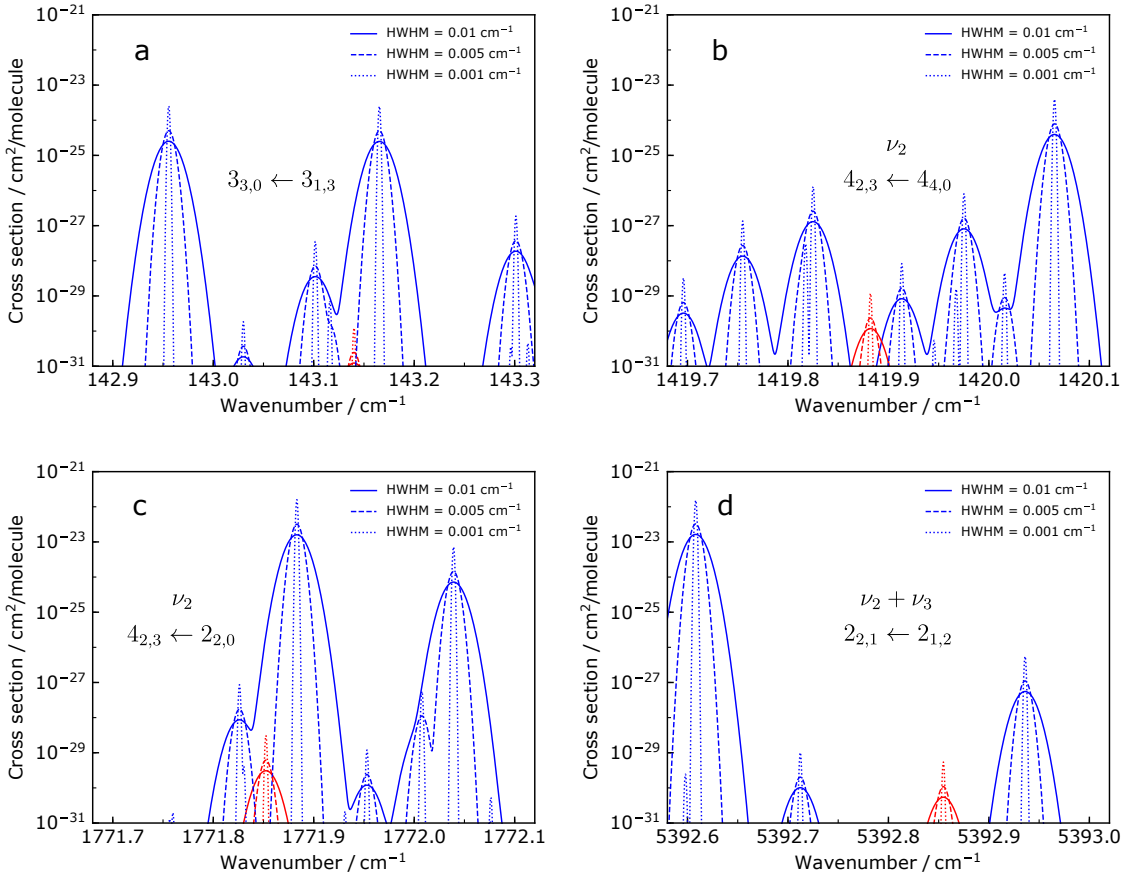

Figure 4.3. Absorption cross sections computed at $T = 296$ K for selected rotational bands, using Gaussian lineshapes with HWHMs of 0.01 cm^{-1} (solid lines), 0.005 cm^{-1} (dashed lines), and 0.001 cm^{-1} (dotted lines). The cross sections for allowed *ortho-ortho* and *para-para* transitions are plotted with blue colour lines and cross sections for forbidden *ortho-para* transitions are plotted with red colour lines.

matrix element of spin-rotation tensor, $\mathcal{M}^{(J'I',JI)}_{\omega,n}$ in (4.9) for this transitions is ± 0.95 kHz and ± 6.3 kHz ($\pm$ for $n = 1,2$) for $\omega = 1$ and 2, respectively. Note that following (4.5) only the spin-rotation tensor with $\omega = 1$ contributes to the *ortho-para* coupling. Allowed transitions into these states from the ground state are quite strong, 2.07×10^{-20} and 3.52×10^{-20} cm/molecule, respectively. Accordingly, intensity borrowing as a result of the spin-rotation interaction of excited states leads to non-zero intensities of the two corresponding forbidden transitions on the order of 10^{-31} molecule/cm. Similarly for other of the strongest forbidden transitions listed in Table 4.1, the enhancement occurs due to intensity borrowing effect from strongly allowed transitions with coincident near resonance between the excited states, accompanied by a relatively large value of the spin-rotation matrix element $\mathcal{M}^{(J'I',JI)}_{\omega=1,n}$.

Though *ortho-para* transitions are yet to be observed in H_2O, there are several spectroscopic studies of the allowed hyperfine transitions in the pure rotational spectrum of $H_2^{16}O$ [214, 223, 227, 228]. We used these data to validate the accuracy of our predictions. In Figure 4.2 the calculated transitions (stems) are compared with the available experimental data (dashed lines), demonstrating an excellent agreement, within 1–4 kHz, for the hyperfine splittings. For example, the root-mean square (rms) deviation of the predicted

hyperfine splittings from experiment is 2.1 kHz in Figure 4.2 a, while for the absolute line positions it is 12.3 kHz. The latter can be explained by the discrepancies in predictions of the pure rotational transitions. The errors in predictions of the hyperfine splittings can be attributed to the level of electronic structure theory, in particular the basis set, employed in the calculations of spin-rotation tensor surface. The basis set convergence of the equilibrium spin-rotation constants of H_2O was investigated elsewhere [214]. According to the results, the employed aug-cc-pwCVTZ basis set produces an average error of 1.3 kHz with a maximum of 1.8 kHz for one of the off-diagonal elements, when compared with the results obtained with the aug-cc-pwCV6Z basis set. There are several predicted splittings in Figure 4.2 d–h that are less than 12 kHz and were not resolved in the experiment [214]. Indeed, by visual inspection of the Lamb-dip spectrum plotted in Fig. 1 of [214], which was provided as an example of the experimental resolution achieved in that work, the transition profiles' full width at a half maximum is about 13 kHz.

The sensitivity and resolution required to observe the *ortho-para* transitions in a prospective experiment can be estimated from the simulated absorption spectrum, shown Figure 4.3 for selected wavenumber ranges with strong *ortho-para* transitions. Since the Doppler linewidth would be around 0.01 cm^{-1} at room temperature and even much higher-resolution spectroscopy was demonstrated [229], we used simple Gaussian line profiles with half-width at half-maximum (HWHM) fixed at 0.01, 0.005, and 0.001 cm^{-1} and computed absorption cross sections at $T = 296$ K using `ExoCross` [230] to predict the experimental spectra. The *ortho-para* transitions In Figure 4.3 a,c (red) show considerable overlap with the allowed transitions (blue) for purely rotational transitions and in the fundamental ν_2 excitation band and could only be detected with an experimental HWHM below 0.005 cm^{-1} at an experimental sensitivity of 10^{-30} and 10^{-29} cm^2/molecule, respectively. In Figure 4.3 b,d, showing parts of the ν_2 and $\nu_2 + \nu_3$ bands, the predicted *ortho-para* transitions are better separated from the allowed transitions and should already be detectable at lower resolution, i. e., at HWHM of 0.01 cm^{-1}, but demand a greater sensitivity of 10^{-30} and 10^{-31} cm^2/molecule, respectively. Such high-sensitivity measurements of intensities on the scale of 10^{-30} cm^2/molecule are currently within reach, for example, using continuous wave laser cavity ring down spectroscopy [218, 231].

4.4 Conclusions

We developed and performed comprehensive variational calculations of the room temperature linelist of H_2O with hyperfine resolution, including forbidden *ortho-para* transitions. The calculations were based on accurate rovibrational energy levels and wavefunctions produced using the variational approach TROVE. The nuclear hyperfine effects were modeled as spin-rotation and direct spin-spin interactions, with the spin-rotation coupling surface calculated at a high level of the electronic-structure theory. We found excellent agreement between the calculated transition frequencies and available hyperfine-resolved spectroscopic data of allowed transitions.

The predicted *ortho-para* transitions are useful for guiding future experimental spectroscopic studies in search of these forbidden transitions in the laboratory as well as in astrophysical environments. Our accurate predictions of hyperfine effects complement the spectroscopic data for water.

The variational approach we developed for computing these hyperfine effects is general. It includes nuclear quadrupole [199, 200], spin-rotation, and spin-spin interactions, and can be applied to other molecular systems without restrictions on the number and values of nuclear spins.

4.5 Supplementary material

The computed hyperfine-linelist data for H_2O are available at https://doi.org/10.5281/zenodo.6337130. The computer codes used in this work are available from git repositories at https://github.com/Trovemaster/TROVE and https://github.com/CFEL-CMI/richmol. The symmetry-adapted nuclear spin functions, character table and direct product table of $C_{2v}(M)$ group for water are all listed in Appendix A.

5 Self-broadening and self-shift in the $3\nu_2$ band of ammonia from mid-infrared frequency-comb spectroscopy *

"I may not have gone where I intended to go, but I think I have ended up where I intended to be."

— Douglas Adams

5.1 Introduction

Ammonia is one of the spectroscopically most-studied molecules due to its importance in the atmosphere, astrophysics, chemistry, medicine and biology. Ammonia exists in a wide range of astrophysical environments and was the first polyatomic molecule detected in the interstellar medium [232]. It was used as one of the most accurate "molecular thermometers" to measure the temperature of C/2001 Q4(Neat) [26], 9P/Tempel 1 [27] and other comets by detecting the *ortho-para* ratio. Ammonia also formed the basis for modern laser technology through the original demonstration of the MASER [233]. Ammonia spectra have been extensively studied and disentangled, both in theory and experiment.

The spectra of ammonia were extensively measured from the microwave to the ultra-violet [234–244]. Yurchenko et al. [116] calculated the spectra for ammonia covering a large part of the infrared region using a variational approach. Recently, we calculated hyperfine-resolved rotation-vibration line lists of ammonia [199, 245], which agree very well with experimental results [246]. The rotation-vibration-spectroscopy data were all critically reviewed and included in the "Measured Active Rotational-Vibrational Energy Levels (MARVEL)" database [247]. The high-resolution transmission (HITRAN) molecular absorption database [129] summarizes the ammonia rotation-vibration spectra, but still has many of the transitions unassigned or absent, especially in the molecular fingerprint region in the mid-infrared (MIR). For instance, there are only two experiments in the 4 µm region, obtained using a Globar source [239] and a synchrotron source [240].

The development of frequency combs (FC) extended the traditional gas-phase-absorption spectroscopy to broadband, which allows for the simultaneous detection of multiple transition regions of multiple species in a short acquisition time [248]. Coherent MIR-FC light sources allow to precisely measure molecular fingerprints which are useful, e. g., in breath analysis, atmospheric measurements, and astrochemistry [248]. Taking breath analysis for an example, ammonia sensing in exhaled human breath could be an indicator of liver and renal diseases [249]. Nonlinear frequency conversion approaches utilizing optical parametric oscillators (OPO) [158, 163, 164], optical parametric amplification (OPA) [165], supercontinuum generation [250, 251], or difference frequency generation (DFG) [166, 167] provide an alternative approach to generate optical frequencies in MIR regions which are not covered by laser gain media. MIR FC sources based on DFG are widely used due to their simplicity, single-pass configuration, broad tunability, and full cancellation of the carrier-envelop offset. The combination of a MIR FC with a Fourier transform spectrometer (FTS) offers capabilities to record spectra over a broadband range and with high resolution,

*This chapter is based on a draft of manuscript: "*Self-broadening and self-shift in the $3\nu_2$ band of ammonia from mid-infrared frequency-comb spectroscopy*" by Guang Yang, Vinicius Silva de Oliveira, Dominic Laumer, Christoph Heyl, Andrey Yachmenev, Ingmar Hartl and Jochen Küpper, **submitted to** *J. Mol. Spectrosc.* (2022), arXiv:2205.04088 [physics]. I contributed to setting up the experiment, recording and analyzing the data, and writing the manuscript.

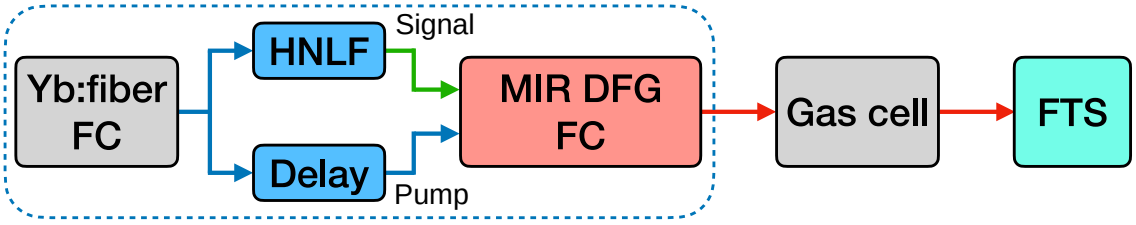

Figure 5.1. Generic schematic of experimental setup. FC: frequency comb, HNLF: highly-nonlinear suspended-core fiber, MIR DFG FC: DFG-based mid-infrared FC, FTS: Fourier transform spectrometer.

high sensitivity, and especially a high signal-to-noise ratio (SNR) due to the high spectral brightness and temporal coherence of FCs [158, 163, 164].

Here, we report the absorption spectrum of the $3\nu_2$ band of $^{14}NH_3$ near 4 µm by a homebuilt FTS coupled to a DFG-based MIR FC covering the range 3–6 µm. We extract the transition wavenumbers and intensities for 6 typical R branch rovibrational lines through a multipeak Voigt fit at room temperature (296 K). We also retrieve self-broadening- and self-shift-parameters of the pressure interactions in the gas at nine different pressures ranging from 10.00 mbar to 700.00 mbar.

5.2 Experiment

A schematic diagram of the experimental setup is shown in Figure 5.1. It consists of three parts: the DFG-based MIR FC source, the gas cell, and the FTS. The MIR FC source consists of a Yb:fiber FC and a DFG setup [167, 170]. The Yb:fiber FC is mode-locked by a saturable absorber with the repetition rate of 150 MHz and phase-locked to a CW laser (Coherent Mephisto) with kHz-level linewidth at ∼1064 nm and frequency stability to 1 MHz/minute. Using chirped-pulse amplification, 1.5 W average power is deliverd in pulses of 130 fs duration with a center wavelength of 1050 nm and a bandwidth of 25 nm. The Yb:fiber FC is split into pump and signal driver of the DFG process, with the signal generated as the longest Raman soliton from the supercontinuum process in a highly-nonlinear suspended-core fiber [169]. By controlling the input power, we could adjust the wavelength of the longest Raman soliton from 1.2 µm to 1.6 µm. The signal and pump pulse are temporally overlapped in a fan-out periodically poled Lithium Niobate (PPLN) crystal (HCPhotonics) for DFG by locking a mechanical delay-line in the pump arm [170]. This yielded MIR radiation ranging from 3 µm to 6 µm. The MIR FC was tuned to near 4 µm (2390 cm^{-1} to 2510 cm^{-1}) and the light passed through the gas cell together with a frequency stabilized (1 MHz/minute) HeNe laser (SIOS SL4), which was used to calibrate the absolute freqyency of the spectroscopic signals.

Ammonia ($^{14}NH_3$, Linde HiQ 6.0) was contained in a 35.4646(12) mm long gas cell with wedged CaF_2 windows (30 arcmin) at 296 K. The optical path length was determined by using low-coherence interferometry [172] with the residual 1050 nm laser from DFG process served as the input signal, which the optical path difference (OPD) of the four reflected light from the two gas cell windows are detected by interfering the reflection with a reference laser. Before the measurements, the reservoir was pumped (HiCube 80 Eco) to 3.1×10^{-4} mbar, filled to 699.75 mbar of ammonia, and then pumped to 543.85 mbar, 500.01 mbar, 400.50 mbar, 300.70 mbar, 199.90 mbar, 98.90 mbar, 50.00 mbar, and 10.00 mbar, respectively. All pressures were measured using calibrated ceramic capacitance gauges (Pfeiffer Vacuum CMR 361 and CMR 364) with a relative accuracy of 0.2%.

The two laser were both directed to our homebuilt FTS, which is based on a Michelson interferometer with two liquid-nitrogen-cooled indium antimonide (InSb) detector (InfraRed Associates IRA 20-00060). The interferograms of both MIR FC and HeNe laser were acquired at 5 MSa/s sampling rate with 20 bit resolution by a computer-controlled data acquisition board (National Instruments PCI-5922). The interferogram of the HeNe laser was used to measure the OPD and provides steps to resample the MIR FC interferogram by determining the positions of the zero-crossings. By matching the delay range of the FTS to the repetation rate of the MIR FC, we overcame the resolution limitation of conventional FTS given by the maximum delay range and removed the instrumental line shape oscillations, which allowed a reduction of the instrument size and acquisition time [185]. The grid spacing was equal to the comb spacing of 150 MHz, yielding a resolution of the FTS of 0.00501 cm^{-1}. After performing a fast Fourier transform (FFT) to MIR FC interferograms, we obtained MIR absorption spectra of ammonia at the different specified pressures. To extract the transmittance, we first measured the reference spectra before filling ammonia when the reservoir was under vacuum.

The top panel of Figure 5.2 a shows the raw spectrum in the range 2434 to 2459 cm^{-1} at 98.90 mbar and at 296 K. The recorded spectra had oscillatory background signals (black curve in Figure 5.2 a) that not only decreased the SNR of the spectra, but also changed the center and linewidth of the absorption line profiles. We assigned this regular signal to etalon effects of the optical components in the experimental setup. In order to remove this etalon signal, we used a numerical approach based on FFT analysis. Firstly, we calculated the power spectral density (PSD) for different FFT sample frequencies of the spectra, shown in Figure 5.2 b. The unit of sample frequencies was in cm, which exactly corresponded to the OPD of the FTS. Then we set the FFT values for the four sample frequencies between 4.10 cm and 4.18 cm to be zero, and performed an inverse FFT, resulting in the filtered spectrum shown in Figure 5.2 a, middle panel. Analyzing the sample frequencies of the filtered signal, Figure 5.2 a, bottom panel, we suppose that the etalon signal most likely comes from an Germanium (Ge) filter in the experimental setup; the length and refractive index of the Ge filter at 4 µm are around 5 mm and 4, resulting in a 4 cm OPD that matches the free spectral range of these oscillations. The FFT filtering might have introduced some small errors as the filtered frequencies also included real spectral information. Nevertheless, these errors should be smaller than profile fitting error and the approach clearly improved the precision and SNR. In the future, the Ge filter shall be replaced by wedged optics.

5.3 Results and discussion

Direct multipeak Voigt fit for the transmittance data was performed to retrieve spectral information. Voigt profile was still valid because the transmittance was more than 90% for all transitions due to the low sensitivity with the short gas cell and the pressures of gas sample were relatively high [252]. The four basic spectroscopic line parameters – the pressure-broadening $\gamma_{p,t}$, the Doppler-broadening α_D, line transition frequency ν_{ij}, and the spectral line intensity I_{ij} – were determined from individual spectra to extract details on the molecular motions and collisions through a non-linear least-squares fit. Since α_D depends on ν_{ij} and temperature, which was 296 K here, we could reduce the Voigt fit to the three other parameters, as shown in (5.1).

$$T(\nu) = e^{I_{ij}(T)Nl_{path}V(\nu-\nu_{ij},\gamma_{p,t})} + a_0 \tag{5.1}$$

Here, N is the number density of ammonia, equals to p/k_bT assuming the ideal gas law,

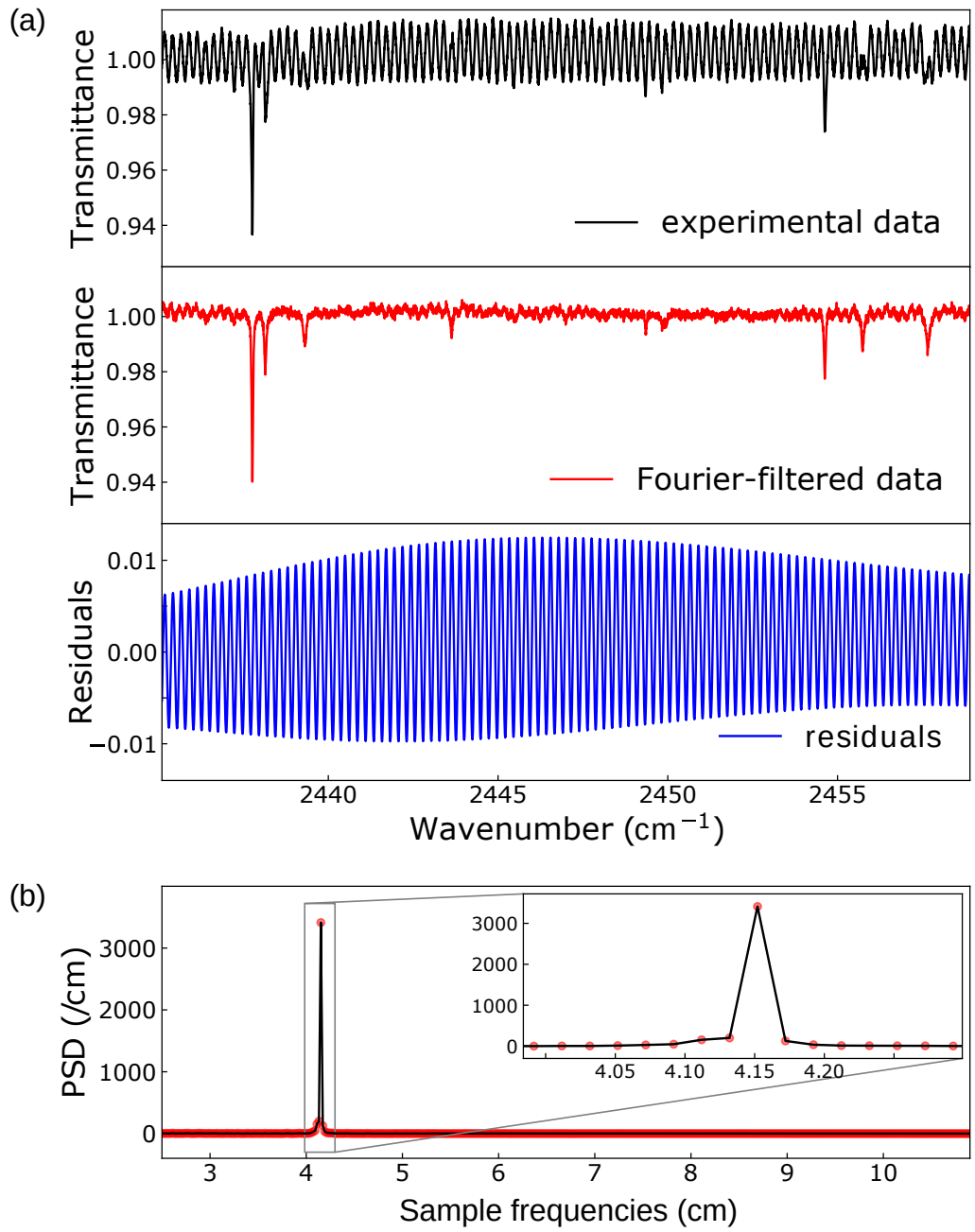

Figure 5.2. (a) The absorption spectra at 98.90 mbar and at room temperature (296 K). The top panel shows the experimentally recorded original spectrum. The middle plot shows the spectra after FFT-filtering. The bottom plot shows the residual differences of the two upper spectra. (b) Partial Power Spectral Density (PSD) of the absorption spectrum in (a).

and l_{path} is the optical path length (35.4646 mm in our experiment). In addition, small instrumental baseline a_0 was added in the fit. We assumed a_0 to be a constant value around 0 since the low sensitivity, more general baseline fitting process could be found from [252].

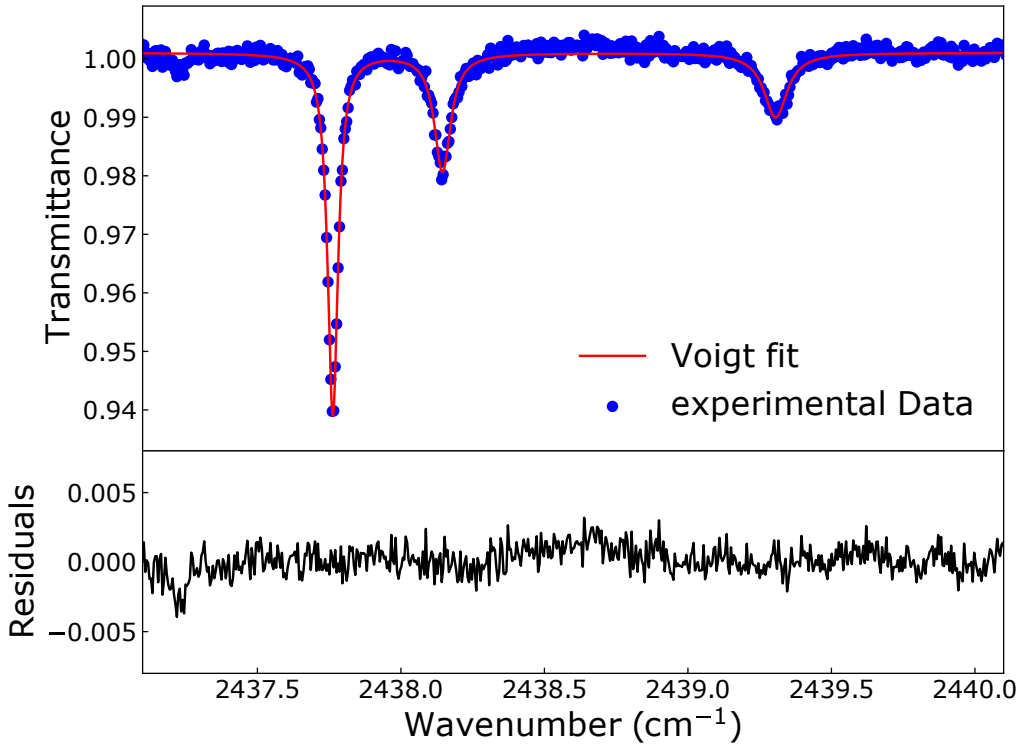

Figure 5.3. Results of the non-linear least-squares fit of the $aR(2,K)$ multiplet assuming Voigt line profiles; $K = 0 \ldots 2$ correspond to the peaks from left to right. Blue dots depict the experimental spectrum, the red line depicts our multipeak Voigt fit. The lower panel shows the residual difference between experiment and simulation, the noise level is around 0.001.

For the fit we chose six typical peaks with high absorption, corresponding to the $aR(2,K)$ and $aR(3,K)$ multiplets in the $3\nu_2$ band. In order to show the performance of the fit, we show the $aR(2,K)$ multiplet in Figure 5.3, which fit very well. The small dip at the low-wavenumber end of the residual difference corresponds to a $sP(6,1)$ transition in $\nu_2 + \nu_4$ band. From the fit, we obtained the line-transition frequencies ν_{ij}, line intensities I_{ij}, and the pressure-broadening component $\gamma_{p,t}$, specifically the self-broadening component γ_{self} since the gas cell only contained pure $^{14}NH_3$.

We recorded and averaged 25 spectra at each of the nine different pressures ranging from 10.00 mbar to 700.00 mbar. It took around 1 minute for recording the spectra and pressures stayed the same during the 25 measurements. Figure 5.4 shows the performance of the global multipeak Voigt fit and the extraction of self-broadening and self-shift coefficients for the $aR(2,0)$ transition. For each pressure, ν_{ij}, I_{ij} and γ_{self} were determined as described above. The mean value of I_{ij} and γ_{self} was extracted. From a linear regression of the line transition wavenumbers ν_{ij} as a function of pressure, see Figure 5.4, the vacuum transition wavenumber ν_{ij}^0 was determined as the y intercept and its self-shift parameter γ_{self} as the slope k.

Line wavenumbers ν_{ij}^0, line intensities I_{ij}, self-broadening γ_{self}, and self-shift δ_{self} components of the $aR(2,K)$ and $aR(3,K)$ multiplet in the $3\nu_2$ band of $^{14}NH_3$ are presented in Table 5.1. Specified uncertainties for line wavenumbers and self-shifts are their standard

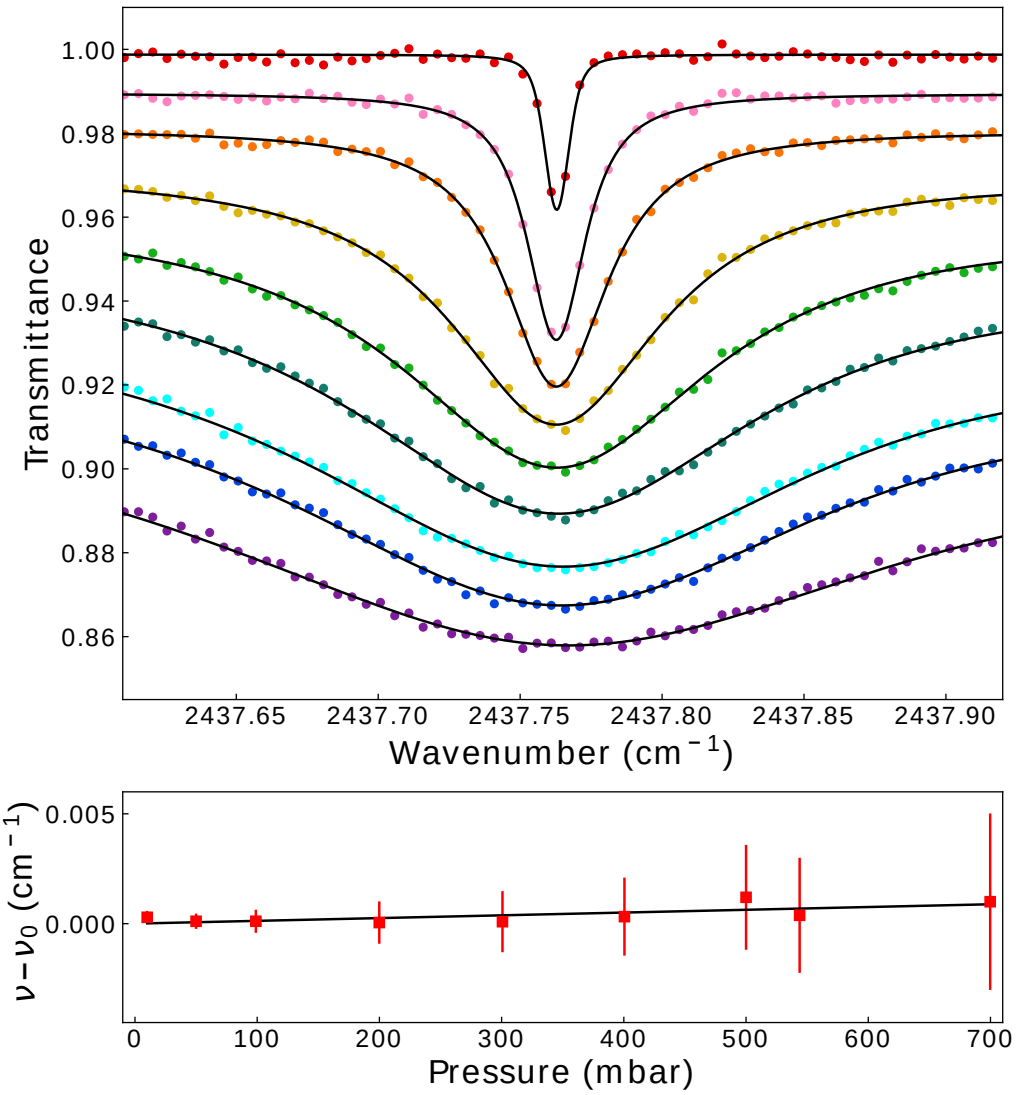

Figure 5.4. Extraction of the self-broadening and self-shift parameters from the lineshape of the $aR(2,0)$ transition at various pressures, i. e., from top to bottom 10.00 mbar, 50.00 mbar, 98.90 mbar, 199.90 mbar, 300.70 mbar, 400.50 mbar, 500.01 mbar, 543.85 mbar, and 699.75 mbar, respectively. The black curves show the fitted Voigt profiles. For clarity, all lines are successively offset by -0.01 from top to bottom. The bottom panel shows the relative line transition wavenumbers (red squares) with respect to the vacuum line transition. Error bars depict the standard deviation from the multipeak Voigt fit. The black line is a linear fit of these transition frequencies from which the vacuum transition wavenumber and the self-shift are derived.

Table 5.1: Line transitions, line intensities, self-broadening, and self-shift coefficients for the $3\nu_2$ band of $^{14}NH_3$ at 296 K.

Transition (R branch)	$\nu^0_{ij,\text{exp.}}$ (cm^{-1})	$\nu_{ij,\text{ref.}}$ * (cm^{-1})	$I_{ij,\text{exp.}}$ (cm/molec.)	$I_{ij,\text{ref.}}$ * (cm/molec.)	$\gamma_{\text{self,exp.}}$ (cm^{-1}/atm)	$\gamma_{\text{self,ref.}}$ * (cm^{-1}/atm)	δ_{self} (cm^{-1}/atm)
$aR(2,0)$	2437.76258(18)	2437.7655	$5.12(19)\times10^{-22}$	4.590×10^{-22}	0.225(13)	0.302	0.0016(5)
$aR(2,1)$	2438.14454(106)	2438.1475	$2.35(21)\times10^{-22}$	2.078×10^{-22}	0.320(33)	0.396	−0.0112(28)
$aR(2,2)$	2439.31026(421)	2439.3148	$1.70(20)\times10^{-22}$	1.372×10^{-22}	0.445(63)	0.496	−0.0139(110)
$aR(3,1)$	2454.62688(68)	2454.6298	$2.26(16)\times10^{-22}$	2.323×10^{-22}	0.263(31)	0.36	−0.0073(18)
$aR(3,2)$	2455.73934(231)	2455.7392	$1.93(15)\times10^{-22}$	1.963×10^{-22}	0.397(43)	0.448	0.0006(62)
$aR(3,3)$	2457.66341(317)	2457.6615	$2.27(21)\times10^{-22}$	2.508×10^{-22}	0.464(62)	0.541	−0.0351(83)

* Data from the HITRAN 2016 database [129, 239, 253], the uncertainty range for ν_0, I_{ij} and γ_{self} are 0.0001 cm^{-1} to 0.001 cm^{-1}, 10% to 20% and 2% to 5%, respectively.

deviations from the fit, the uncertainties for line intensities and self-broadenings were the combination of statistical errors from the averaging of multiple scans and the standard deviations from the fit. Other systematic errors such as misalignments of the HeNe laser and MIR FC, the line mixing, the FFT fliter etc. were neglected because they were relatively small in relation to the errors from the fit. Line-transition wavenumbers and intensities show good agreement with the HITRAN database values [129]. Our retrieved self-broadening parameters were around 20% smaller than in the HITRAN database, which were derived from measurements at 10 µm [253]. Our results provide new laboratory data allowing to improve pressure-self-broadening models.

5.4 Conclusions

We recorded the broadband absorption spectra of the $3\nu_2$ band of ammonia ($^{14}NH_3$) near 4 µm using a MIR-FC-based FTS system. Spectra were background corrected by FFT-filtering raw spectra for experimental etalon. A global multipeak Voigt fit allowed us to determine transition wavenumbers and intensities, pressure self-broadening and self-shift parameters at room temperature ($T = 296$ K) for 6 prototypical R branch rovibrational transitions.

The recorded line wavenumbers and line intensities are in good agreement with the HITRAN database. As no literature values were available for the self-broadening and self-shift parameters, our new experimental data on these parameters provide useful information about the molecular motions and collisions, which could help to improve their theoretical modeling.

Our experimental system is capable of trace-gas detection of different molecular species in the spectral range of 3…6 µm with a current resolution of 0.00501 cm^{-1}. We plan to implement a liquid-nitrogen-cooled multi-pass-cell cryostat to increase the sensitivity.

6 Further improvements on Fourier transform spectrometer

"Measure what is measurable, and make measurable what is not so."

— Galileo Galilei

6.1 Liquid-nitrogen-cooled multi-pass-cell cryostat

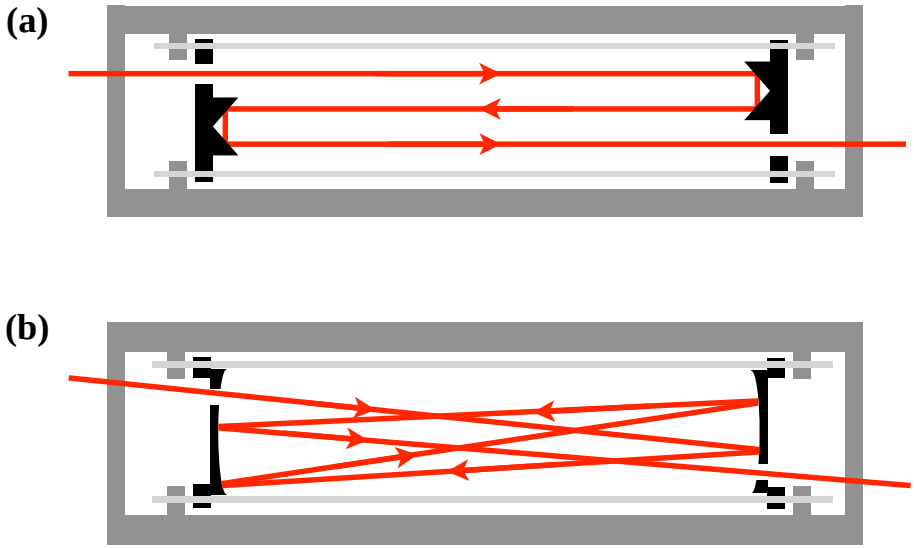

Figure 6.1. Third-pass and multi-pass configurations of the gas cell.

Due to the low sensitivity of and etalon signal from the Fourier transform spectrometer (FTS), we cannot resolve the hyperfine structure, and observe the nuclear-spin-forbidden transitions for water or ammonia. A liquid-nitrogen-cooled multi-pass-cell cryostat has been designed to improve the sensitivity of FTS. According to the Beer-Lambert law as mentioned in (2.40), we can improve the sensitivity of FTS by increasing the optical path length of the gas sample and spectral absorption cross-section. For increasing the optical path length, the third-pass roof-mirror configuration (around 1 m) and multi-pass Herriott-cell configuration (around 10 m) will be applied as illustrated in Figure 6.1. Compared to our existing gas cell which is 35.4646 mm long, the multi-pass configurations can increase the sensitivity by about 2–3 orders of magnitude. For increasing the absorption cross-sections, the new gas cell is hanging below a Dewar bottle filled with liquid nitrogen. The gas samples can be cooled down to 77 K, which yields more molecules populated on the ground states. For the transitions from these states, the increasing spectral absorption cross-sections increase the sensitivity by 2–3 orders of magnitude. Another advantage of our cryostat is that the Doppler width will decrease at low temperature, which allows us to resolve more transitions.

Figure 6.2 shows the top view of the cryostat. The wedge windows with Brewster angle and the double-side pump will be performed to eliminate the etalon signal and make the position of the inner cell fixed, respectively. Since there are no data about the vapor pressure for water and ammonia at 77 K, a flexible magnetic-field-free resist heater will be circled around the two sides of the inner cell to adjust the temperature of the gas sample. We will also apply the similar resist heater on the flanges of inner cell windows to avoid samples

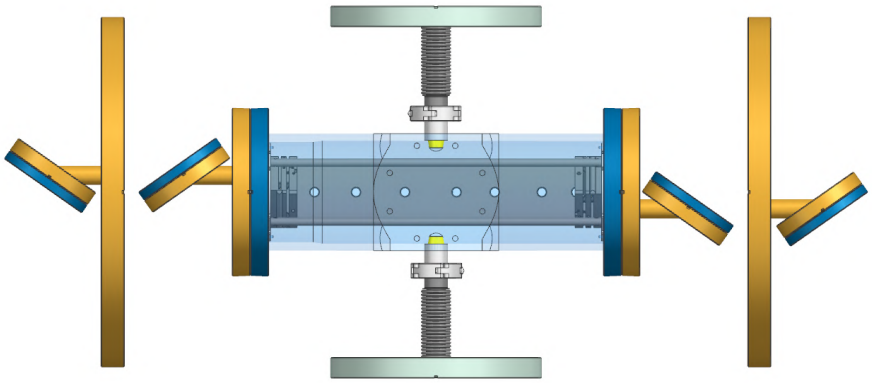

Figure 6.2. Topview of the liquid-nitrogen-cooled multi-pass-cell cryostat.

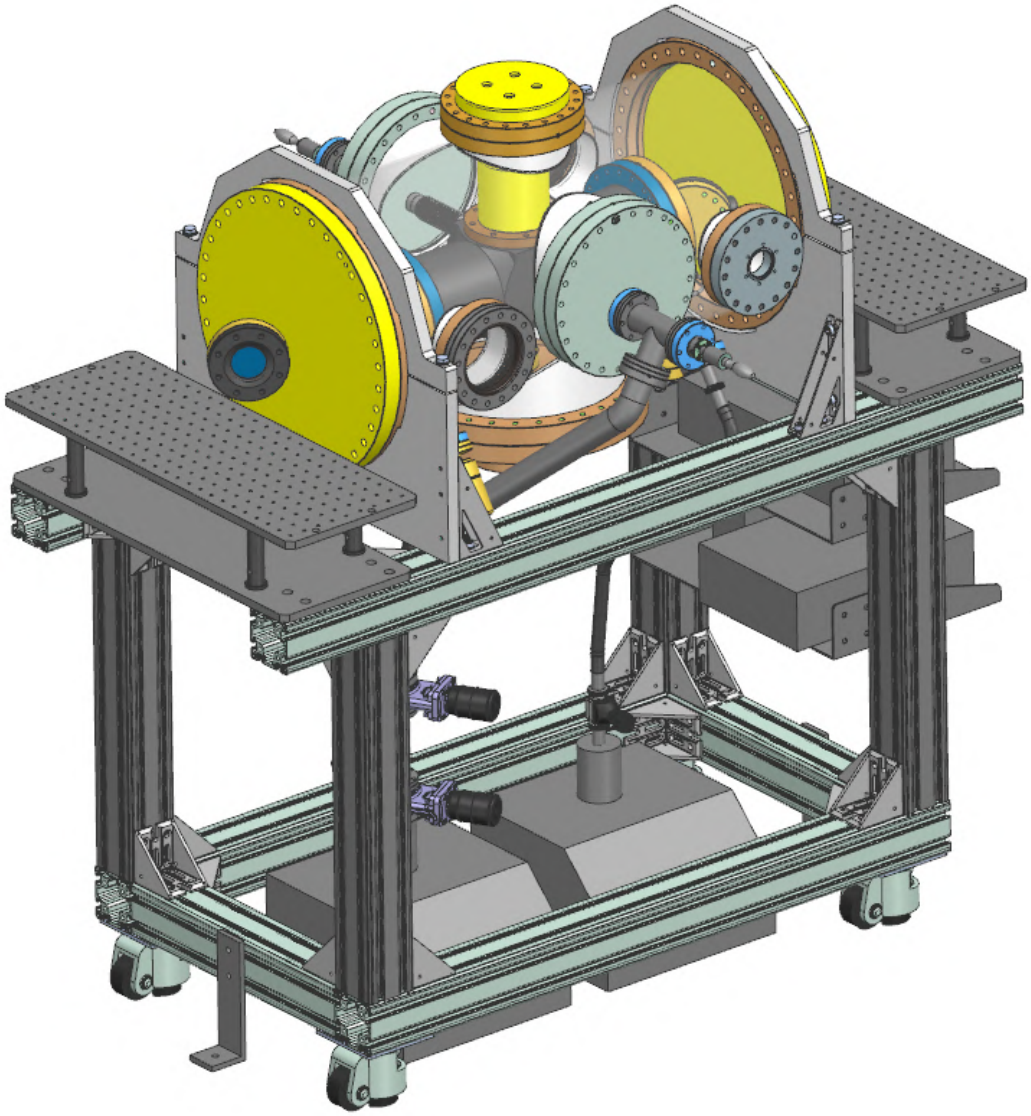

Figure 6.3. Overview of the liquid-nitrogen-cooled multi-pass-cell cryostat.

from solidating on the window. The total design of the cryostat is shown in Figure 6.3. The gas cell is held inside a vacuum chamber, which is placed on an aluminum frame. To isolate the vibration from the environment, we apply the vibration canceling rollers, and the two pump stations will lay on silicone rubber. With the liquid-nitrogen-cooled multi-pass-cell cryostat, we can detect the transitions with line intensities higher than 10^{-28} cm/molecule.

6.2 Doppler free spectroscopy

The second improvement in our FTS is the application of Doppler free spectroscopy [254]. The Doppler free spectroscopy can reveal spectra feature smaller than the Doppler width such as hyperfine structure, Coriolis effects, and so on. Many experimental techniques have already been developed to overcome the Doppler width limitation and achieve sub-Doppler resolution. These techniques can be organized as follows: saturation spectroscopy, Doppler-free multiphoton spectroscopy, spectroscopy in molecular beams, coherent spectroscopy, and spectroscopy of ultracold molecules. Among these methods, saturation spectroscopy is more widely used due to the simplicity of the experimental setup. The principle of saturation spectroscopy is to select the zero velocity components of a group of molecules in the direction of the laser beam. The selection is performed by pump and probe beam from the same laser, propagating in opposite directions. Lamb dips will exhibit on the Doppler-broadened line profile.

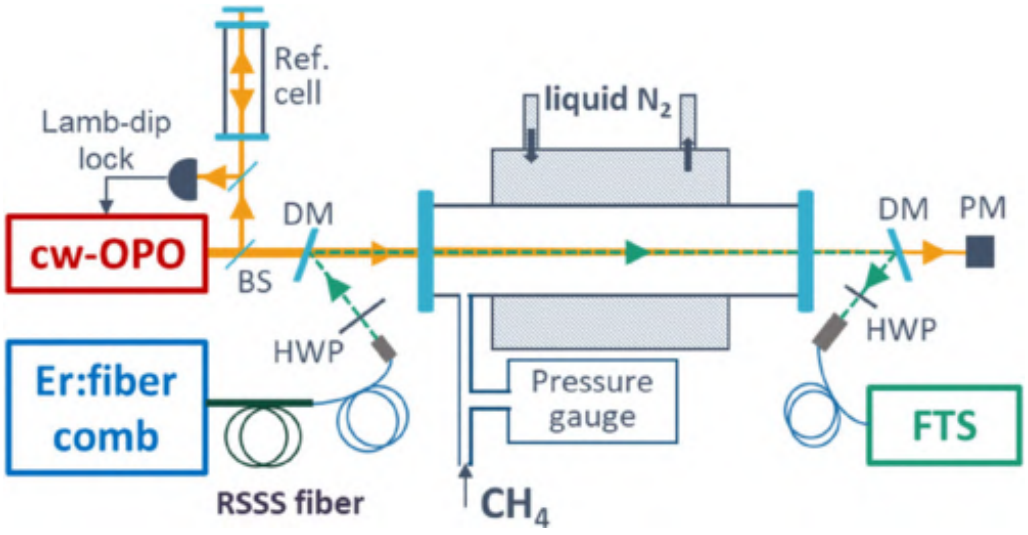

Figure 6.4. Experimental setup of the optical-optical double-resonance spectroscopy with a frequency comb probe, reprint from [255].

The pump and probe beams can also be from two different lasers, which is called the optical-optical double-resonance (OODR) spectroscopy [256]. The OODR spectroscopy provides a powerful method for the assignment of highly excited energy levels by detecting the population of ground states through V-type excitations, and excited states through ladder-type or Λ-type excitations. Recently, Aleksandra et al. [255] firstly performed OODR spectroscopy of methane with a frequency comb (FC) probe realizing sub-Doppler resolution. The pump and probe beams were 3 µm CW laser and 1.67 µm FC, respectively. The two beams were aligned and propagated together to a liquid-nitrogen-cooled gas cell as shown in Figure 6.4. The pump laser was stabilized to the center of the addressed transition by a Lamb-dip locking system with a reference cell. The probe was applied by shifting 1.55 µm Er:fiber comb to cover 55 nm with Raman soliton self-frequency shift microstructured silica

fiber. The FTS setup was similar to our system and the nominal resolution was set to 250 MHz, the same as the repetition rate of the FC. The transmittance of a V-type OODR spectrum is shown in Figure 6.5. The inset shows the transition with sub-Doppler free width in the $2\nu_3$ band of methane.

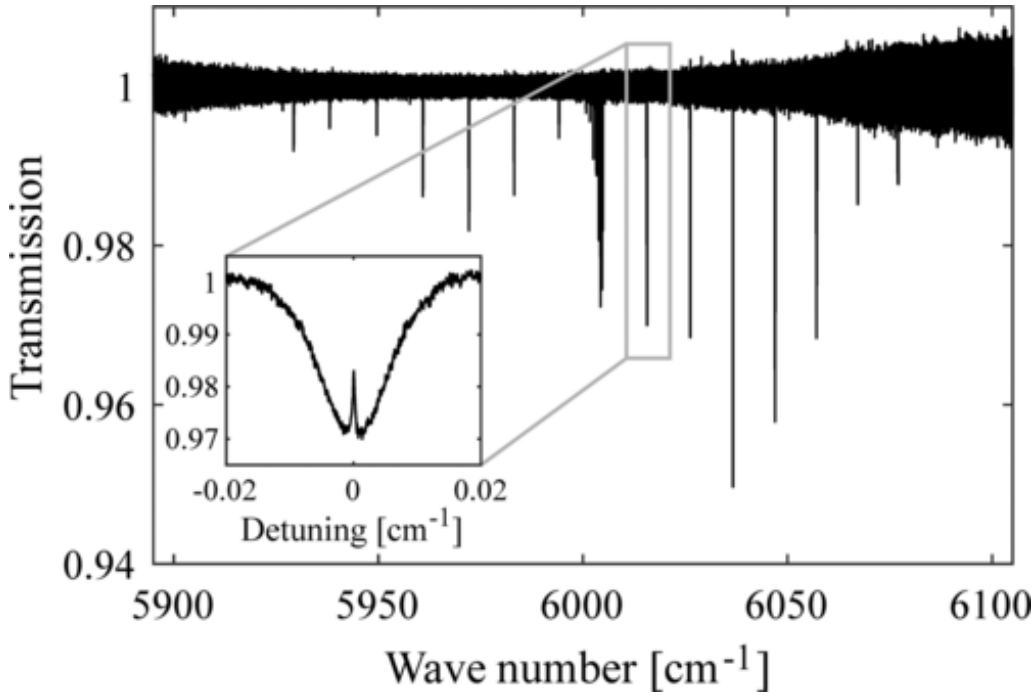

Figure 6.5. V-type optical-optical double-resonance spectrum with a frequency comb probe of the $2\nu_3$ band for methane molecule, reprint from [255]

OODR spectroscopy with a FC probe provides a way to measure broadband spectrum with sub-Doppler width, which allows for accurate assignment of the high excited states and verification of the theoretical prediction. With our newly designed liquid-nitrogen-cooled multi-pass-cell cryostat and the OODR spectroscopy with a FC probe, we can resolve the hyperfine structure of water and ammonia, and possibly observe some isolated *ortho-para* transitions.

7 Conclusions and outlook

> *"The most incomprehensible fact of nature is the fact that nature is comprehensible."*
>
> — Albert Einstein

The main purpose of this thesis is to predict and observe the nuclear-spin-forbidden transitions of the water and ammonia molecules. I have reported the new high-accuracy hyperfine linelist including the *ortho-para* transitions of the water molecule at room temperature, and rovibrational spectra of the ammonia molecule measured from the mid-infrared frequency-comb-based Fourier transform spectrometer.

The theoretical investigation of the *ortho-para* transitions of $H_2{}^{16}O$ is presented in chapter 4, which are driven by the nuclear spin-rotation and spin-spin interactions. This was achieved by using the `hyfor` module of the Python software package Richmol. The rovibrational molecular states calculated in TROVE were treated as a variational basis. Comparisons with several spectroscopic experiments of the allowed pure rotational hyperfine transitions prove the accuracy of the theoretical calculation. The results suggest that the strongest spectral line intensities of *ortho-para* transitions at room temperature are on the order of 10^{-31} cm/molecule. Several transitions are relatively isolated from the allowed transitions, and should be possibly observed in experiments as predicted in Figure 4.3 ranging from microwave to mid-infrared. This general approach applies to XY_2-type molecules, for example, H_2S. As described in Appendix B, the linelist of hyperfine rovibrational transitions for H_2S has already been computed with an energy cutoff at 40 000 cm^{-1}, and the total angular momentum quantum number up to $F = 59$. For XY_3-type molecules, especially NH_3, the symmetry-adapted nuclear spin functions have been derived as shown in Appendix A, and will be employed in Richmol soon.

Fourier transform spectrometer based on a mid-infrared frequency comb with a resolution of 0.00501 cm^{-1} has been performed to measure the spectra of water and ammonia as described in chapter 3. The broadband absorption spectra of the $3\nu_2$ band of $^{14}NH_3$ near 4 µm was recorded after numerical filtering of the etalon signal as shown in chapter 5. This numerical approach can predict the possible optical components causing the etalon signal by monitoring the power spectral density of the sample frequencies. Line positions, line intensities, self-broadening, and self-shift parameters for six rovibrational lines were determined by direct multipeak Voigt fit at room temperature. Owing to the sensitivity limitation of the short-length gas cell, we can only resolve the transitions with spectral line intensity stronger than 10^{-22} cm/molecule. A liquid-nitrogen-cooled multi-pass-cell cryostat (Section 6.1) will be applied to increase the sensitivity of the Fourier transform spectrometer by 4–6 orders of magnitude. Plus the optical-optical double-resonance spectroscopy (Section 6.2) with a frequency comb probe, the hyperfine structure can be resolved, and the *ortho-para* transitions can be possibly observed.

Since the spectral line intensities of *ortho-para* transitions are very low as shown in Figure 4.1. It is still difficult to observe the nuclear-spin-forbidden transitions even with the best-performance cavity-enhanced spectroscopy. The problem now moves to the enhancements of the *ortho-para* transitions. Two approaches have been proposed and investigated.

The first approach is applying the external electric field or field gradient. For the molecules presented in an external electric field, the Stark effect happens. This effect mixes the *ortho* and *para* states between the *ortho-para* electric dipole transitions. It also enhances the *ortho-para* mixing when the energy differences between *ortho* and *para* states become smaller. These two benefits can enhance the *ortho-para* transitions. One order of magnitude of enhancement has been found in our recent study. For the electric field gradient, the same

benefits can be realized by coupling with the electric quadrupole moment. In astrophysics, the dominant interstellar solid surface is amorphous solid water with giant electric fields (10^{10}–10^{11} V·m^{-1}) and steep atomic-scale gradients (10^{20}–10^{21} V·m^{-2}) [257]. Because of these giant and steep fields and field gradients, the *ortho-para* transitions can get great enhancement, and the hyperfine effects should be the second mechanism of *ortho-para* conversion in outer space besides the collisions. Further investigations still need to be done by optimizing the values of the external fields or field gradients for suitable transitions.

The second approach is populating to the rotational cluster states. A good case will be H_2S. Appendix B shows the line strengths of the *ortho-para* transitions between the cluster states can be 10^{-3} Debye^2. They are on the same order of magnitude as the corresponding *ortho-ortho* and *para-para* transitions due to the stronger *ortho-para* mixing among the rotational cluster states. By the optical centrifuge, the *ortho-para* transitions for H_2S can be possibly observed in the rotational cluster states. In addition, the nuclear spin symmetry breaks due to the stronger *ortho-para* mixing in the rotational chiral states, which provides a way of producing nuclear-spin-polarized molecules for parity violation study.

Appendices

A Symmetry-adapted nuclear spin functions for water and ammonia

> *"The root of all symmetry principles lies in the assumption that it is impossible to observe certain basic quantities; these will be called 'non-observables'."*
>
> — T. D. Lee

For the $H_2^{16}O$ molecule in $C_{2v}(M)$ symmetry group, there are two identical protons and one ^{16}O nucleus. For the two protons with nuclear spin quantum number of $1/2$, we denote α for "spin-up" ($|\frac{1}{2},\frac{1}{2}\rangle$) nuclear spin function and β for "spin-down" ($|\frac{1}{2},-\frac{1}{2}\rangle$) nuclear spin function. A ^{16}O nucleus has nuclear spin quantum number of 0, we write the nuclear spin function as $\delta = |0,0\rangle$. The four coupled nuclear spin functions [75] are

$$|1,1\rangle = \alpha\alpha\delta \qquad A_1 \tag{A.1}$$

$$|1,-1\rangle = \beta\beta\delta \qquad A_1 \tag{A.2}$$

$$|1,0\rangle = \frac{\sqrt{2}}{2}(\alpha\beta+\beta\alpha)\delta \qquad A_1 \tag{A.3}$$

$$|0,0\rangle = \frac{\sqrt{2}}{2}(\alpha\beta-\beta\alpha)\delta \qquad B_2, \tag{A.4}$$

generating the representation

$$\Gamma_{ns}^{H_2O} = 3A_1 \oplus B_2. \tag{A.5}$$

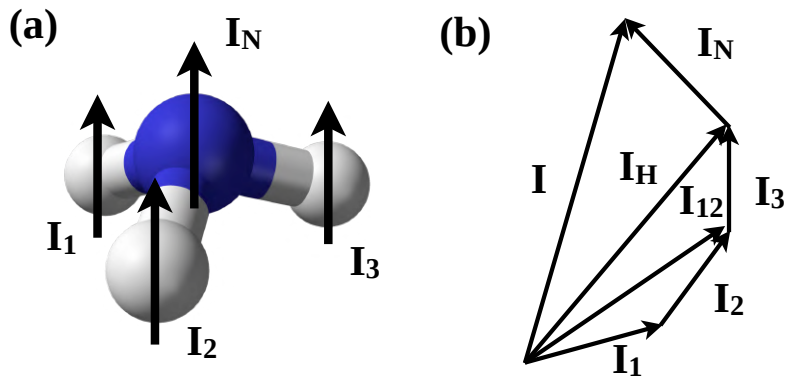

Figure A.1. Coupling scheme of nuclear spins for NH_3 molecule.

The nuclear spin functions for ammonia in $D_{3h}(M)$ symmetry group are a little bit complex compared to water since the ammonia molecule has three identical protons and one N nucleus with nuclear spin quantum number of 1. To derive the total nuclear spin functions for ammonia, we first couple the three hydrogen spins as shown in Figure A.1:

$$\begin{aligned}|I_{12}I_3I_Hm_{I_H}\rangle = \sum_{m_{I_1},m_{I_2},m_{I_3},m_{I_{12}}} &\langle I_{12}m_{I_{12}},I_3m_{I_3}|I_Hm_{I_H}\rangle \\ &\langle I_1m_{I_1},I_2m_{I_2}|I_{12}m_{I_{12}}\rangle|I_1m_{I_1},I_2m_{I_2},I_3m_{I_3}\rangle,\end{aligned} \tag{A.6}$$

here $I_1 = I_2 = I_3 = \frac{1}{2}$, $m_{I_1} = m_{I_2} = m_{I_3} = \pm\frac{1}{2}$, $I_{12} = 1,0$, $m_{I_{12}} = 0,\pm1$, $I_H = \frac{3}{2},\frac{1}{2}$, and $m_{I_H} =$

$\pm\frac{3}{2}, \pm\frac{1}{2}$. We get the eight coupled nuclear spin functions of three protons by calculating the Clebsch-Gordan coefficients:

$$|\frac{3}{2}, \frac{3}{2}\rangle = \alpha\alpha\alpha \qquad A_1^{'} \tag{A.7}$$

$$|\frac{3}{2}, \frac{1}{2}\rangle = \frac{\sqrt{3}}{3}(\alpha\beta\alpha + \beta\alpha\alpha + \alpha\alpha\beta) \qquad A_1^{'} \tag{A.8}$$

$$|\frac{3}{2}, -\frac{1}{2}\rangle = \frac{\sqrt{3}}{3}(\beta\beta\alpha + \alpha\beta\beta + \beta\alpha\beta) \qquad A_1^{'} \tag{A.9}$$

$$|\frac{3}{2}, -\frac{3}{2}\rangle = \beta\beta\beta \qquad A_1^{'} \tag{A.10}$$

$$|\frac{1}{2}, \frac{1}{2}\rangle = \frac{\sqrt{6}}{6}(2\alpha\alpha\beta - \alpha\beta\alpha - \beta\alpha\alpha) \qquad E'(\phi_a) \tag{A.11}$$

$$|\frac{1}{2}, -\frac{1}{2}\rangle = \frac{\sqrt{6}}{6}(\alpha\beta\beta + \beta\alpha\beta - 2\beta\beta\alpha) \qquad E'(\phi_a) \tag{A.12}$$

$$|\frac{1}{2}, \frac{1}{2}\rangle = \frac{\sqrt{2}}{2}(\alpha\beta\alpha - \beta\alpha\alpha) \qquad E'(\phi_b) \tag{A.13}$$

$$|\frac{1}{2}, -\frac{1}{2}\rangle = \frac{\sqrt{2}}{2}(\alpha\beta\beta - \beta\alpha\beta) \qquad E'(\phi_b). \tag{A.14}$$

Then we couple the total proton spin with nuclear spin of N nucleus,

$$|I_H I_N I m_I\rangle = \sum_{m_{I_H}, m_{I_N}} \langle I_H m_{I_H}, I_N m_{I_N} | I m_I\rangle |I_H m_{I_H}, I_N m_{I_N}\rangle, \tag{A.15}$$

here $I_N = 1$ and $m_{I_N} = 1, 0$. For N nucleus, we construct γ for $|1,1\rangle$ nuclear spin function, δ for $|1,0\rangle$ nuclear spin function, and ϵ for $|1,-1\rangle$ nuclear spin function. With the same procedure aforementioned, we get the 24 coupled nuclear spin functions for NH_3 molecules:

$$|\frac{5}{2}, \frac{5}{2}\rangle = \alpha\alpha\alpha\gamma \qquad A_1^{'} \tag{A.16}$$

$$|\frac{5}{2}, \frac{3}{2}\rangle = \frac{\sqrt{5}}{5}(\alpha\beta\alpha\gamma + \beta\alpha\alpha\gamma + \alpha\alpha\beta\gamma + \sqrt{2}\alpha\alpha\alpha\delta) \qquad A_1^{'} \tag{A.17}$$

$$|\frac{5}{2}, \frac{1}{2}\rangle = \frac{\sqrt{10}}{10}(\beta\beta\alpha\gamma + \alpha\beta\beta\gamma + \beta\alpha\beta\gamma + \sqrt{2}\alpha\beta\alpha\delta + \sqrt{2}\beta\alpha\alpha\delta + \sqrt{2}\alpha\alpha\beta\delta + \alpha\alpha\alpha\epsilon) \qquad A_1^{'} \tag{A.18}$$

$$|\frac{5}{2}, -\frac{1}{2}\rangle = \frac{\sqrt{10}}{10}(\alpha\beta\alpha\epsilon + \beta\alpha\alpha\epsilon + \alpha\alpha\beta\epsilon + \sqrt{2}\beta\beta\alpha\delta + \sqrt{2}\alpha\beta\beta\delta + \sqrt{2}\beta\alpha\beta\delta + \beta\beta\beta\gamma) \qquad A_1^{'} \tag{A.19}$$

$$|\frac{5}{2}, -\frac{3}{2}\rangle = \frac{\sqrt{5}}{5}(\beta\beta\alpha\epsilon + \alpha\beta\beta\epsilon + \beta\alpha\beta\epsilon + \sqrt{2}\beta\beta\beta\delta) \qquad A_1^{'} \tag{A.20}$$

$$|\frac{5}{2}, -\frac{5}{2}\rangle = \beta\beta\beta\epsilon \qquad A_1^{'} \tag{A.21}$$

$$|\frac{3}{2}, \frac{3}{2}\rangle = \frac{\sqrt{15}}{15}(3\alpha\alpha\alpha\delta - \sqrt{2}\alpha\beta\alpha\gamma - \sqrt{2}\beta\alpha\alpha\gamma - \sqrt{2}\alpha\alpha\beta\gamma) \qquad A_1^{'} \tag{A.22}$$

$$|\frac{3}{2}, \frac{1}{2}\rangle = \frac{\sqrt{5}}{15}(\alpha\beta\alpha\delta + \beta\alpha\alpha\delta + \alpha\alpha\beta\delta + 3\sqrt{2}\alpha\alpha\alpha\epsilon - 2\sqrt{2}\beta\beta\alpha\gamma - 2\sqrt{2}\alpha\beta\beta\gamma - 2\sqrt{2}\beta\alpha\beta\gamma) \qquad A_1^{'} \tag{A.23}$$

$$|\frac{3}{2},-\frac{1}{2}\rangle = \frac{\sqrt{5}}{15}(2\sqrt{2}\alpha\beta\alpha\epsilon + 2\sqrt{2}\beta\alpha\alpha\epsilon + 2\sqrt{2}\alpha\alpha\beta\epsilon - \beta\beta\alpha\delta - \alpha\beta\beta\delta - \beta\alpha\beta\delta - 3\sqrt{2}\beta\beta\beta\gamma) \quad A_1^{'} \quad (A.24)$$

$$|\frac{3}{2},-\frac{3}{2}\rangle = \frac{\sqrt{15}}{15}(\sqrt{2}\beta\beta\alpha\epsilon + \sqrt{2}\alpha\beta\beta\epsilon + \sqrt{2}\beta\alpha\beta\epsilon - 3\beta\beta\beta\delta) \quad A_1^{'} \quad (A.25)$$

$$|\frac{3}{2},\frac{3}{2}\rangle = \frac{\sqrt{6}}{6}(2\alpha\alpha\beta\gamma - \alpha\beta\alpha\gamma - \beta\alpha\alpha\gamma) \quad E'(\phi_a) \quad (A.26)$$

$$|\frac{3}{2},\frac{1}{2}\rangle = \frac{\sqrt{2}}{6}(\alpha\beta\beta\gamma + \beta\alpha\beta\gamma - 2\beta\beta\alpha\gamma + 2\sqrt{2}\alpha\alpha\beta\delta - \sqrt{2}\alpha\beta\alpha\delta - \sqrt{2}\beta\alpha\alpha\delta) \quad E'(\phi_a) \quad (A.27)$$

$$|\frac{3}{2},-\frac{1}{2}\rangle = \frac{\sqrt{2}}{6}(2\alpha\alpha\beta\epsilon - \alpha\beta\alpha\epsilon - \beta\alpha\alpha\epsilon + \sqrt{2}\alpha\beta\beta\delta + \sqrt{2}\beta\alpha\beta\delta - 2\sqrt{2}\beta\beta\alpha\delta) \quad E'(\phi_a) \quad (A.28)$$

$$|\frac{3}{2},-\frac{3}{2}\rangle = \frac{\sqrt{6}}{6}(\alpha\beta\beta\epsilon + \beta\alpha\beta\epsilon - 2\beta\beta\alpha\epsilon) \quad E'(\phi_a) \quad (A.29)$$

$$|\frac{3}{2},\frac{3}{2}\rangle = \frac{\sqrt{2}}{2}(\alpha\beta\alpha\gamma - \beta\alpha\alpha\gamma) \quad E'(\phi_b) \quad (A.30)$$

$$|\frac{3}{2},\frac{1}{2}\rangle = \frac{\sqrt{6}}{6}(\alpha\beta\beta\gamma - \beta\alpha\beta\gamma + \sqrt{2}\alpha\beta\alpha\delta - \sqrt{2}\beta\alpha\alpha\delta) \quad E'(\phi_b) \quad (A.31)$$

$$|\frac{3}{2},-\frac{1}{2}\rangle = \frac{\sqrt{6}}{6}(\alpha\beta\alpha\epsilon - \beta\alpha\alpha\epsilon + \sqrt{2}\alpha\beta\beta\delta - \sqrt{2}\beta\alpha\beta\delta) \quad E'(\phi_b) \quad (A.32)$$

$$|\frac{3}{2},-\frac{3}{2}\rangle = \frac{\sqrt{2}}{2}(\alpha\beta\beta\epsilon - \beta\alpha\beta\epsilon) \quad E'(\phi_b) \quad (A.33)$$

$$|\frac{1}{2},\frac{1}{2}\rangle = \frac{\sqrt{2}}{6}(3\alpha\alpha\alpha\epsilon + \beta\beta\alpha\gamma + \alpha\beta\beta\gamma + \beta\alpha\beta\gamma - \sqrt{2}\alpha\beta\alpha\delta - \sqrt{2}\beta\alpha\alpha\delta - \sqrt{2}\alpha\alpha\beta\delta) \quad A_1^{'} \quad (A.34)$$

$$|\frac{1}{2},-\frac{1}{2}\rangle = \frac{\sqrt{2}}{6}(3\beta\beta\beta\gamma + \alpha\beta\alpha\epsilon + \beta\alpha\alpha\epsilon + \alpha\alpha\beta\epsilon - \sqrt{2}\beta\beta\alpha\delta - \sqrt{2}\alpha\beta\beta\delta - \sqrt{2}\beta\alpha\beta\delta) \quad A_1^{'} \quad (A.35)$$

$$|\frac{1}{2},\frac{1}{2}\rangle = \frac{\sqrt{2}}{6}(2\alpha\alpha\beta\delta - \alpha\beta\alpha\delta - \beta\alpha\alpha\delta - \sqrt{2}\alpha\beta\beta\gamma - \sqrt{2}\beta\alpha\beta\gamma + 2\sqrt{2}\beta\beta\alpha\gamma) \quad E'(\phi_a) \quad (A.36)$$

$$|\frac{1}{2},-\frac{1}{2}\rangle = \frac{\sqrt{2}}{6}(2\beta\beta\alpha\delta - \alpha\beta\beta\delta - \beta\alpha\beta\delta + 2\sqrt{2}\alpha\alpha\beta\epsilon - \sqrt{2}\alpha\beta\alpha\epsilon - \sqrt{2}\beta\alpha\alpha\epsilon) \quad E'(\phi_a) \quad (A.37)$$

$$|\frac{1}{2},\frac{1}{2}\rangle = \frac{\sqrt{6}}{6}(\alpha\beta\alpha\delta - \beta\alpha\alpha\delta - \sqrt{2}\alpha\beta\beta\gamma + \sqrt{2}\beta\alpha\beta\gamma) \quad E'(\phi_b) \quad (A.38)$$

$$|\frac{1}{2},-\frac{1}{2}\rangle = \frac{\sqrt{6}}{6}(\beta\alpha\beta\delta - \alpha\beta\beta\delta + \sqrt{2}\alpha\beta\alpha\epsilon - \sqrt{2}\beta\alpha\alpha\epsilon) \quad E'(\phi_b), \quad (A.39)$$

generating the representation

$$\Gamma_{ns}^{NH_3} = 12A_1' \oplus 6E'. \quad (A.40)$$

The character and direct product tables of $C_{2v}(M)$ and $D_{3h}(M)$ group are shown below.

Table A.1: Character table of $C_{2v}(M)$ group

	E	E^*	(1,2)	$(1,2)^*$
A_1	1	1	1	1
A_2	1	1	-1	-1
B_1	1	-1	-1	1
B_2	1	-1	1	-1

Table A.2: Direct product table of $C_{2v}(M)$ group

	A_1	A_2	B_1	B_2
A_1	A_1	A_2	B_1	B_2
A_2	A_2	A_1	B_2	B_1
B_1	B_1	B_2	A_1	A_2
B_2	B_2	B_1	A_2	A_1

Table A.3: Character table of $D_{3h}(M)$ group

	E	(123)	(23)	E^*	$(123)^*$	$(23)^*$
A_1'	1	1	1	1	1	1
A_1''	1	1	1	-1	-1	-1
A_2'	1	1	-1	1	1	-1
A_2''	1	1	-1	-1	-1	1
E'	2	-1	0	2	-1	0
E''	2	-1	0	-2	1	0

Table A.4: Direct product table of $D_{3h}(M)$ group

	A_1'	A_1''	A_2'	A_2''	E'	E''
A_1'	A_1'	A_1''	A_2'	A_2''	E'	E''
A_1''	A_1''	A_1'	A_2''	A_2'	E''	E'
A_2'	A_2'	A_2''	A_1'	A_1''	E'	E''
A_2''	A_2''	A_2'	A_1''	A_1'	E''	E'
E'	E'	E''	E'	E''	$A_1' \oplus A_2' \oplus E'$	$A_1'' \oplus A_2'' \oplus E''$
E''	E''	E'	E''	E'	$A_1'' \oplus A_2'' \oplus E''$	$A_1' \oplus A_2' \oplus E'$

B Hyperfine interaction in rotational chiral states of hydrogen sulfide

"The exception proves the rule."

— Marcus Tullius Cicero

B.0.1 *Ortho-para* transitions in rotational cluster states

Like water, hydrogen sulfide has two different nuclear spin isomers, *ortho*-H_2S and *para*-H_2S. Our theoretical approach can be easily extended to H_2S for calculating the *ortho-para* transitions as described in chapter 4. But for H_2S, we care more about the high rotational cluster states, in which the fourfold high rotational levels with different symmetry aspects are degenerate form dynamic chirality [258–260]. The top panel of Figure B.1 shows the rotational energy level of the ground vibrational state up to the rotational angular moment quantum number $J = 55$. The energy differences $E_{Jk} - E_{Jk}^{max}$ has been plotted for all rotational states in the lower panel of Figure B.1, relative to the maximum energy E_{Jk}^{max} in their J multiplet. As J increases, the energy differences between energy levels start to decrease and the cluster states form after a certain J value.

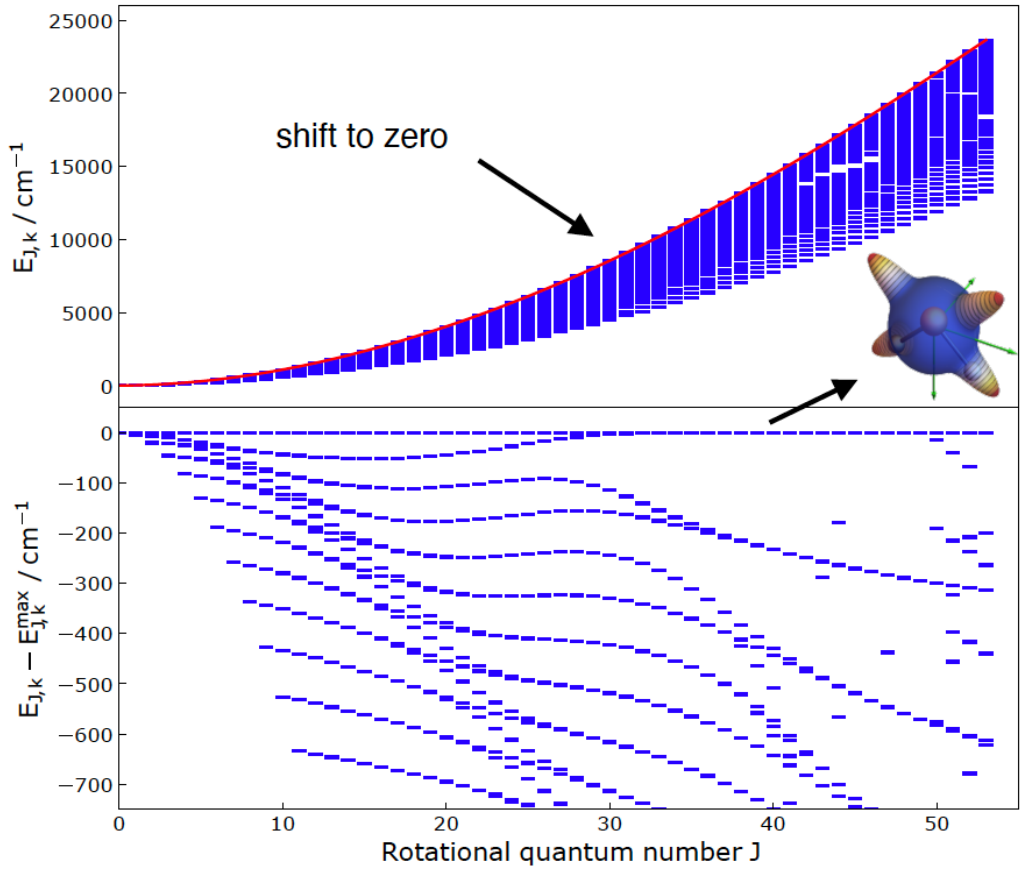

Figure B.1. Rotaional energy level clustering in the ground vibrational state of H_2S.

The linelist of hyperfine rovibrational transitions for H_2S has been computed with an energy cutoff at 40 000 cm^{-1}, and includes transitions up to $F = 59$ ($J = 60$). Line strengths are given in the linelist instead of line intensities because of the lower population of the rotational cluster states. The *ortho-para* transitions with line position cutoff at 1000 cm^{-1}

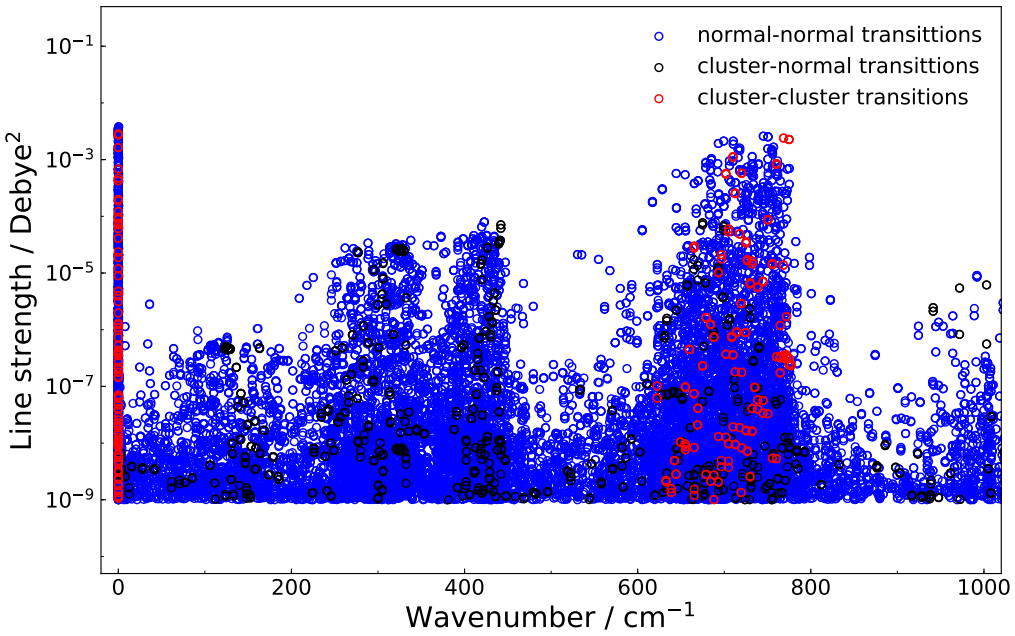

Figure B.2. *Ortho-para* transitions of $H_2^{16}S$ with line position cutoff at 1000 cm^{-1} and line strength cutoff at 10^{-9} Debye^2. Here we select only one set of cluster states with the lowest energies for each J. The cluster-cluster, cluster-normal, and normal-normal *ortho-para* transitions are marked with red, black, and blue circles, respectively.

and line strength cutoff at 10^{-9} Debye^2 are plotted and shown in Figure B.2. Since the strong *ortho-para* mixing in rotational cluster states, the line strengths for the *ortho-para* transitions are quite high on the order of 10^{-3} Debye^2. The red circles corresponding to the cluster-cluster *ortho-para* transitions are distributed in two ranges as shown in Figure B.2. The first range is near 0 cm^{-1} belonging to the internal *ortho-para* transitions among one set of cluster states, and the second range are *ortho-para* transitions between two different sets of cluster states. Here we select only one set of cluster states with the lowest energies for each J, which are easier to realize in experiments by applying an optical centrifuge [260–262]. More cluster-cluster and cluster-normal *ortho-para* transitions are hidden inside the normal-normal *ortho-para* transitions.

Figure B.3 shows the cluster-cluster *ortho-para* transitions with line strength cutoff at 10^{-3} Debye^2. The line strength of the cluster-cluster *ortho-para* transitions between $J = 46$ and $J = 47$ are on the same order of magnitude with the corresponding *ortho-ortho* and *para-para* transitions. Because of this great enhancement, the *ortho-para* transitions for H_2S can possibly be observed in the rotational cluster states achieved by the optical centrifuge.

B.0.2 Nuclear spin density

Because of the strong *ortho-para* mixing in rotational chiral states, the nuclear spin symmetry breaks. Nuclear-spin-polarized molecules can be produced with an optical centrifuge. It will be useful for studying the parity violation in molecules [263–265]. The nuclear spin density for H_2S can be defined as

$$\rho = \sum_{I,I'} \sum_{\gamma,\gamma'} a_{JI\gamma}^{Fm_F l *} a_{JI\gamma}^{Fm_F l} \langle Fm_F, JI\gamma | \delta(\Omega - \Omega_1) I_0^{(1)}{}_1 + \delta(\Omega - \Omega_1) I_0^{(1)}{}_2) | Fm_F, JI'\gamma' \rangle, \quad \text{(B.1)}$$

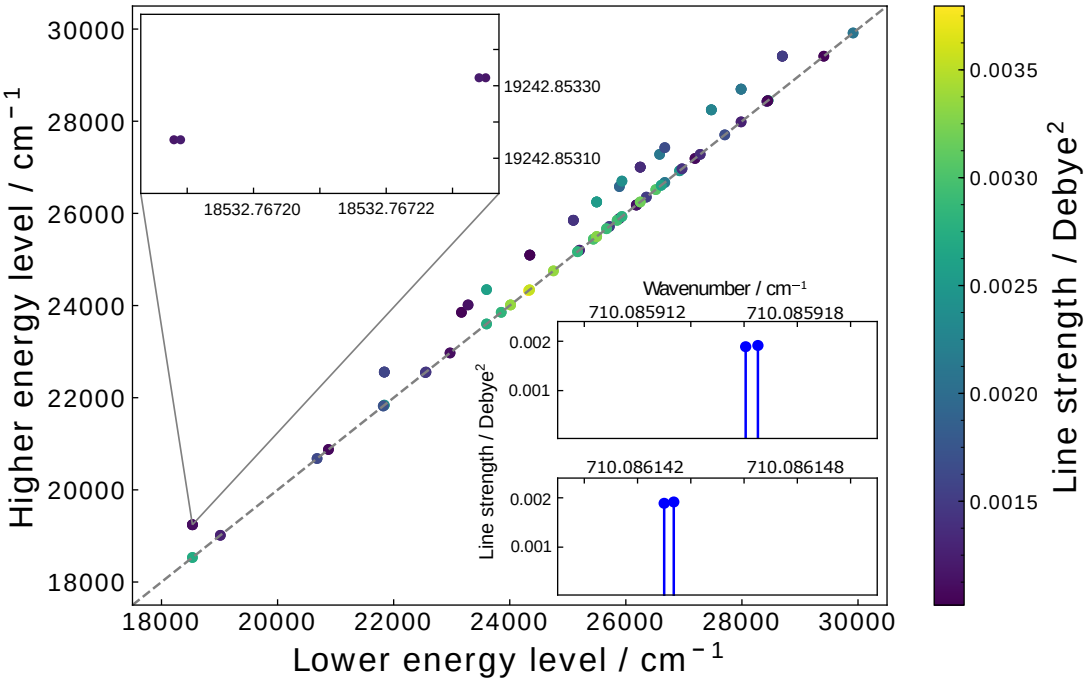

Figure B.3. The cluster-cluster *ortho-para* transitions with line strength cutoff at 10^{-3} Debye^2. The top-left panel shows the cluster-cluster *ortho-para* transitions between $J = 46$ and $J = 47$. The lower-right panel shows the corresponding *ortho-ortho* and *para-para* transitions with the line strength on the same order of magnitude.

where Ω_1 and Ω_2 are the Euler angles for positions of H_1 and H_2 atom, $a_{JI\gamma}^{Fm_Fl}$ is the ortho-para mixing coefficients. The hyperfine basis functions are given by

$$|Fm_F, JI\gamma\rangle = \sqrt{2F+1}\cdot(-1)^{J-I+m_F}\begin{pmatrix} J & I & F \\ m & m_I & -m_F \end{pmatrix}|Jm\gamma\rangle|Im_I\rangle, \tag{B.2}$$

with rovibrational basis function from TROVE

$$|Jm\gamma\rangle = \sum_k \sum_v C_{kv}^{Jm\gamma}|Jkm\rangle|v\rangle, \tag{B.3}$$

and the derived nuclear spin functions

$$|Im_I\rangle = \sqrt{2I+1}\cdot(-1)^{m_I}\sum_{m_{I_1},m_{I_2}}\begin{pmatrix} I_1 & I_2 & I \\ m_{I_1} & m_{I_2} & -m_I \end{pmatrix}|I_1,m_{I_1}\rangle|I_2,m_{I_2}\rangle. \tag{B.4}$$

The nuclear spin density has the final form of

$$\begin{aligned}\rho = &\sqrt{6}\cdot\frac{2J+1}{16\pi^2}\sum_{I,I'}\sum_{\gamma,\gamma'}\sum_{m_I,m_{I'}}\sum_{k,k'} a_{JI\gamma}^{Fm_Fl\,*}\, a_{JI\gamma}^{Fm_Fl}\cdot(-1)^{I+I'}(2F+1)\sqrt{(2I+1)(2I'+1)} \\ &\begin{pmatrix} J & I & F \\ m & m_I & -m_F \end{pmatrix}\begin{pmatrix} J & I' & F \\ m & m_{I'} & -m_F \end{pmatrix}\begin{pmatrix} I & 1 & I' \\ -m_I & 0 & m_{I'} \end{pmatrix} \\ &\Bigg(C_{kk'}^{Jmm'\gamma\gamma'} D_{mk}^{J}(\Omega_1) {D_{m'k'}^{J}}^{*}(\Omega_1)(-1)^{I+I'-m_I}\begin{Bmatrix} I_1 & I & I_2 \\ I' & I_1' & 1 \end{Bmatrix} \\ &\quad + C_{kk'}^{Jmm'\gamma\gamma'} D_{mk}^{J}(\Omega_2) {D_{m'k'}^{J}}^{*}(\Omega_2)(-1)^{2I-m_I}\begin{Bmatrix} I_2 & I & I_1 \\ I' & I_2' & 1 \end{Bmatrix}\Bigg),\end{aligned} \tag{B.5}$$

where $C_{kk'}^{Jmm'\gamma\gamma'} = \sum_v C_{kv}^{Jm\gamma\,*} C_{k'v'}^{Jm'\gamma'}$, and D_{mk}^{J} is the Wigner rotation matrix elements.

Bibliography

[1] Sin-itiro Tomonaga (translated by Takeshi Oka). *The Story of Spin*. The University of Chicago Press, Chicago and London, 1997. ISBN 0-226-80793-2.

[2] Martin Gardner. *The New Ambidextrous Universe: Symmetry and Asymmetry from Mirror Reflections to Superstrings*. Dover Publications, Mineola, New York, 2005. ISBN 0-486-44244-6.

[3] Alison Wright. The spinning electron. *Nat. Phys.*, 4(1):S6–S7, 2008. doi: 10.1038/nphys8587. URL https://doi.org/10.1038/nphys858.

[4] C. Runge and F. Paschen. On the spectrum of clèveite gas. *Astrophys. J.*, 3:4–28, 1896. doi: 10.1086/140172. URL https://ui.adsabs.harvard.edu/abs/1896ApJ....3....4R.

[5] Takeshi Oka. *Orders of Magnitude and Symmetry in Molecular Spectroscopy*. John Wiley & Sons, 2011. ISBN 9780470749593. doi: https://doi.org/10.1002/9780470749593.hrs074. URL https://onlinelibrary.wiley.com/doi/abs/10.1002/9780470749593.hrs074.

[6] E. Rutherford. The scattering of α and β particles by matter and the structure of the atom. *The London, Edinburgh, and Dublin Philosophical Magazine and Journal of Science*, 21(125):669–688, 1911. doi: 10.1080/14786440508637080. URL https://doi.org/10.1080/14786440508637080.

[7] N. Bohr. I. On the constitution of atoms and molecules. *The London, Edinburgh, and Dublin Philosophical Magazine and Journal of Science*, 26(151):1–25, 1913. doi: 10.1080/14786441308634955. URL https://doi.org/10.1080/14786441308634955.

[8] W. Gerlach and O. Stern. Der experimentelle Nachweis der Richtungsquantelung im Magnetfeld. *Z. Phys.*, 9:349–352, 1922. doi: 10.1007/BF01326983. URL http://dx.doi.org/10.1007/BF01326983.

[9] Arnold Eucken. Die Molekularwärme des Wasserstoffs bei tiefen Temperaturen. *Sitzungsberichte der Königlich Preussischen Akademie der Wissenschaften zu Berlin*, pages 141–151, 1912. URL https://www.biodiversitylibrary.org/item/126475#page/1/mode/1up.

[10] Takeo Hori. Über die Analyse des Wasserstoffbandenspektrums im äußersten Ultraviolett. *Z. Phys.*, 44:834–854, 1927. doi: 10.1007/BF013908573. URL https://doi.org/10.1007/BF01390857.

[11] L. De Broglie. Wave and quanta. *Nature*, 112:540, 1923. doi: 10.1038/112540a0. URL https://doi.org/10.1038/112540a0.

[12] W. Pauli. Über den Zusammenhang des Abschlusses der Elektronengruppen im Atom mit der Komplexstruktur der Spektren. *Z. Phys.*, 31:765–783, 1925. doi: 10.1007/BF02980631. URL https://doi.org/10.1007/BF02980631.

[13] S. Goudsmit G. Uhlenbeck. Ersetzung der Hypothese vom unmechanischen Zwang durch eine Forderung bezüglich des inneren Verhaltens jedes einzelnen Elektrons. *Die Naturwissenschaften*, 13:953–954, 1925. doi: 10.1007/BF01558878. URL https://doi.org/10.1007/BF01558878.

[14] Werner Heisenberg. Mehrkörperprobleme und Resonanz in der Quantenmechanik. II. *Z. Phys.*, 41:239–267, 1927. doi: 10.1007/BF01391241. URL https://doi.org/10.1007/BF01391241.

[15] F. Hund. Zur Deutung der Molekelspektren. II. *Z. Phys.*, 42:93–120, 1927. doi: 10.1007/BF01397124. URL https://doi.org/10.1007/BF01397124.

[16] David M. Dennison. A note on the specific heat of the hydrogen molecule. *Proc. Royal Soc. London A*, 115:483–486, 1927. doi: 10.1098/rspa.1927.0105. URL https://doi.org/10.1098/rspa.1927.0105.

[17] P. Harteck K. F. Bonhoeffer. Experimente über Para- und Orthowasserstoff. *Die Naturwissenschaften*, 17:182, 1929. doi: 10.1007/BF01506559. URL https://doi.org/10.1007/BF01506559.

[18] W. Pauli. The connection between spin and statistics. *Phys. Rev.*, 58:716–722, 1940. doi: 10.1103/PhysRev.58.716. URL https://link.aps.org/doi/10.1103/PhysRev.58.716.

[19] Tetsuya Hama, Akira Kouchi, and Naoki Watanabe. The ortho-to-para ratio of water molecules desorbed from ice made from para-water monomers at 11 K. *Astrophys. J. Lett.*, 857(2):L13, 2018. doi: 10.3847/2041-8213/aabc0c. URL https://doi.org/10.3847/2041-8213/aabc0c.

[20] A. G. G. M. Tielens. The molecular universe. *Rev. Mod. Phys.*, 85(3):1021–1081, 2013. doi: 10.1103/RevModPhys.85.1021. URL http://link.aps.org/doi/10.1103/RevModPhys.85.1021.

[21] Martin Quack. Detailed symmetry selection rules for reactive collisions. *Mol. Phys.*, 34 (2):477–504, 1977. doi: 10.1080/00268977700101861. URL http://dx.doi.org/10.1080/00268977700101861.

[22] Takeshi Oka. Nuclear spin selection rules in chemical reactions by angular momentum algebra. *J. Mol. Spectrosc.*, 228(2):635–639, 2004. doi: 10.1016/j.jms.2004.08.015. URL http://www.sciencedirect.com/science/article/pii/S0022285204002693.

[23] Dairene Uy, Michel Cordonnier, and Takeshi Oka. Observation of ortho-para H_3^+ selection rules in plasma chemistry. *Phys. Rev. Lett.*, 78(20):3844–3847, 1997. doi: 10.1103/PhysRevLett.78.3844. URL http://link.aps.org/doi/10.1103/PhysRevLett.78.3844.

[24] Dalgarno A., Black J. H., and Weisheit J. C. Ortho-para transitions in H_2 and the fractionation of HD. *Astrophys. Lett.*, 14:77, 1973. URL https://adsabs.harvard.edu/pdf/1973ApL....14...77D.

[25] J. Le Bourlot. Ammonia formation and the ortho-to-para ratio of H_2 in dark clouds. *Astron. Astrophys.*, 242:235, 1991. URL https://ui.adsabs.harvard.edu/abs/1991A&A...242..235L.

[26] Hideyo Kawakita, Neil Dello Russo, Reiko Furusho, Tetsuharu Fuse, Jun-ichi Watanabe, D. C. Boice, Kozo Sadakane, Nobuo Arimoto, Michiko Ohkubo, and Takashi Ohnishi. Ortho-to-para ratios of water and ammonia in comet C/2001 Q4 (NEAT): Comparison of nuclear spin temperatures of water, ammonia, and methane. *Astrophys. J.*, 643(2):1337–1344, 2006. doi: 10.1086/503185. URL https://doi.org/10.1086%2F503185.

[27] Hideyo Kawakita, Emmanuel Jehin, Jean Manfroid, and Damien Hutsemékers. Nuclear spin temperature of ammonia in comet 9P/Tempel 1 before and after the deep impact event. *Icarus*, 191:513–516, 2007. doi: 10.1016/j.icarus.2006.10.044. URL http://www.sciencedirect.com/science/article/pii/S0019103507004289.

[28] M. J. Mumma, H. A. Weaver, and H. P. Larson. The ortho-para ratio of water vapor in comet P/Halley. *Astron. Astrophys.*, 187:419–424, 1987. URL https://ui.adsabs.harvard.edu/abs/1987A&A...187..419M.

[29] E. F. van Dishoeck, E. A. Bergin, D. C. Lis, and J. I. Lunine. *Water: From Clouds to Planets*, pages 835–858. University of Arizona Press, Tucson, 2014. ISBN 9780816598762. URL https://muse.jhu.edu/book/35621.

[30] K. Willacy, C. Alexander, M. Ali-Dib, C. Ceccarelli, S. B. Charnley, M. Doronin, Y. Ellinger, P. Gast, E. Gibb, S. N. Milam, O. Mousis, F. Pauzat, C. Tornow, E. S. Wirström, and E. Zicler. The composition of the protosolar disk and the formation conditions for comets. *Space Science Reviews*, 197(1-4):151–190, 2015. doi: 10.1007/s11214-015-0167-6. URL https://doi.org/10.1007/s11214-015-0167-6.

[31] T. Putaud, X. Michaut, F. Le Petit, E. Roueff, and D. C. Lis. The water line emission and ortho-to-para ratio in the Orion Bar photon-dominated region. *Astron. Astrophys.*, 632:A8, 2019. doi: 10.1051/0004-6361/201935402. URL https://doi.org/10.1051/0004-6361/201935402.

[32] Jon T. Hougen and Takeshi Oka. Nuclear spin conversion in molecules. *Science*, 310(5756):1913–1914, 2005. doi: 10.1126/science.1122110. URL http://www.sciencemag.org/content/310/5756/1913.short.

[33] Pierre-Alexandre Turgeon, Jonathan Vermette, Gil Alexandrowicz, Yoann Peperstraete, Laurent Philippe, Mathieu Bertin, Jean-Hugues Fillion, Xavier Michaut, and Patrick Ayotte. Confinement effects on the nuclear spin isomer conversion of H_2O. *J. Phys. Chem. A*, 121(8):1571–1576, 2017. doi: 10.1021/acs.jpca.7b00893. URL https://doi.org/10.1021/acs.jpca.7b00893.

[34] C. Beduz, M. Carravetta, J. Y.-C. Chen, M. Concistre, M. Denning, M. Frunzi, A. J. Horsewill, O. G. Johannessen, R. Lawler, X. Lei, M. H. Levitt, Y. Li, S. Mamone, Y. Murata, U. Nagel, T. Nishida, J. Ollivier, S. Rols, T. Room, R. Sarkar, N. J. Turro, and Y. Yang. Quantum rotation of ortho and para-water encapsulated in a fullerene cage. *PNAS*, 109(32):12894–12898, 2012. doi: 10.1073/pnas.1210790109. URL https://doi.org/10.1073/pnas.1210790109.

[35] R. F. Curl Jr., Jerome V. V. Kasper, and Kenneth S. Pitzer. Nuclear spin state equilibration through nonmagnetic collisions. *J. Chem. Phys.*, 46(8):3220–3228, 1967. doi: 10.1063/1.1841193. URL https://doi.org/10.1063/1.1841193.

[36] P. L. Chapovsky and L. J. F. Hermans. Nuclear spin conversion in polyatomic molecules. *Annu. Rev. Phys. Chem.*, 50(1):315–345, 1999. doi: 10.1146/annurev.physchem.50.1.315. URL http://arjournals.annualreviews.org/doi/abs/10.1146/annurev.physchem.50.1.315.

[37] P. L. Chapovsky. Conversion of nuclear spin isomers of water molecules under ultracold conditions of space. *Quantum Electron.*, 49(5):473–478, 2019. doi: 10.1070/qel17006. URL https://doi.org/10.1070/qel17006.

[38] P. Cacciani, J. Cosléou, and M. Khelkhal. Nuclear spin conversion in H_2O. *Phys. Rev. A*, 85(1):012521, 2012. doi: 10.1103/PhysRevA.85.012521. URL http://link.aps.org/doi/10.1103/PhysRevA.85.012521.

[39] P. L. Chapovsky. Nuclear spin conversion in formaldehyde. *J. Mol. Struct.*, 599(1-3):337–345, 2001. doi: 10.1016/s0022-2860(01)00854-7. URL https://doi.org/10.1016/s0022-2860(01)00854-7.

[40] P. L. Chapovsky. Hyperfine spectra of CH_3F nuclear spin conversion. *J. Phys. B*, 33(5):1001–1011, 2000. doi: 10.1088/0953-4075/33/5/314. URL https://doi.org/10.1088%2F0953-4075%2F33%2F5%2F314.

[41] P. Cacciani, J. Cosléou, M. Khelkhal, M. Tudorie, C. Puzzarini, and P. Pracna. Nuclear spin conversion in NH_3. *Phys. Rev. A*, 80(4):042507, 2009. doi: 10.1103/physreva.80.042507. URL https://doi.org/10.1103/physreva.80.042507.

[42] Zhen-Dong Sun, Meihua Ge, and Yujun Zheng. Separation and conversion dynamics of nuclear-spin isomers of gaseous methanol. *Nat. Commun.*, 6(1):6877, 2015. doi: 10.1038/ncomms7877. URL https://doi.org/10.1038/ncomms7877.

[43] Li-Sha Ma, Zhen-Dong Sun, and Pavel L. Chapovsky. Nuclear spin conversion

in gaseous methanol. *Phys. Rev. A*, 102:032810, 2020. doi: 10.1103/PhysRevA.102.032810. URL https://link.aps.org/doi/10.1103/PhysRevA.102.032810.

[44] P. L. Chapovsky, J. Cosléou, F. Herlemont, M. Khelkhal, and J. Legrand. Separation and conversion of nuclear spin isomers of ethylene. *Chem. Phys. Lett.*, 322(5):424–428, 2000. doi: 10.1016/s0009-2614(00)00445-0. URL https://doi.org/10.1016/s0009-2614(00)00445-0.

[45] Zhen-Dong Sun, Kojiro Takagi, and Fusakazu Matsushima. Separation and conversion dynamics of four nuclear spin isomers of ethylene. *Science*, 310(5756):1938–1941, 2005. doi: 10.1126/science.1120037. URL http://www.sciencemag.org/content/310/5756/1938.abstract.

[46] F. Kh. Gel'Mukhanov and A. M. Shalagin. Light-induced diffusion of gases. *JETP Lett.*, 29(12):711–713, 1979. URL https://ui.adsabs.harvard.edu/abs/1979ZhPmR..29..773G.

[47] Pierre-Alexandre Turgeon, Patrick Ayotte, Elina Lisitsin, Yossi Meir, Tatyana Kravchuk, and Gil Alexandrowicz. Preparation, isolation, storage, and spectroscopic characterization of water vapor enriched in the ortho-H_2O nuclear spin isomer. *Phys. Rev. A*, 86(6):062710, 2012. doi: 10.1103/PhysRevA.86.062710. URL http://link.aps.org/doi/10.1103/PhysRevA.86.062710.

[48] L. Abouaf-Marguin, A.-M. Vasserot, C. Pardanaud, and X. Michaut. Nuclear spin conversion of water diluted in solid argon at 4.2 K: Environment and atmospheric impurities effects. *Chem. Phys. Lett.*, 447(4):232–235, 2007. doi: 10.1016/j.cplett.2007.09.014. URL http://www.sciencedirect.com/science/article/pii/S0009261407012377.

[49] Russell Sliter, Melissa Gish, and Andrey F. Vilesov. Fast nuclear spin conversion in water clusters and ices: A matrix isolation study. *J. Phys. Chem. A*, 115(34):9682–9688, 2011. doi: 10.1021/jp201125k. URL http://dx.doi.org/10.1021/jp201125k.

[50] B. Gauthier-Roy, L. Abouaf-Marguin, and P. Boissel. Dipolar interactions between NH_3 molecules trapped in solid argon. I. Kinetics of the nuclear spin species conversion. *J. Chem. Phys.*, 98(9):6827–6834, 1993. doi: 10.1063/1.464774. URL https://doi.org/10.1063/1.464774.

[51] P. Boissel, B. Gauthier-Roy, and L. Abouaf-Marguin. Dipolar interactions between NH_3 molecules trapped in solid argon. II. Line narrowing during nuclear spin species conversion. *J. Chem. Phys.*, 98(9):6835–6842, 1993. doi: 10.1063/1.464775. URL https://doi.org/10.1063/1.464775.

[52] Llewellyn H. Jones, Scott A. Ekberg, and Basil I. Swanson. Hindered rotation and site structure of methane trapped in rare gas solids. *J. Chem. Phys.*, 85(6):3203–3210, 1986. doi: 10.1063/1.450988. URL https://doi.org/10.1063/1.450988.

[53] M. Miki and T. Momose. Rovibrational transitions and nuclear spin conversion of methane in parahydrogen crystals. *Low. Temp. Phys.*, 26:661–668, 2000. doi: 10.1063/1.1312392. URL https://doi.org/10.1063/1.1312392.

[54] T. Momose, M. Fushitani, and H. Hoshina. Chemical reactions in quantum crystals. *Int. Rev. Phys. Chem.*, 24:533–552, 2005. doi: 10.1080/01442350500444107. URL https://doi.org/10.1080/01442350500444107.

[55] Yuan-Pern Lee, Yu-Jong Wu, R. M. Lees, Li-Hong Xu, and Jon T. Hougen. Internal rotation and spin conversion of CH_3OH in solid para-Hydrogen. *Science*, 311(5759):365–368, 2006. doi: 10.1126/science.1121300. URL https://www.science.org/doi/abs/10.1126/science.1121300.

[56] J. P. Perchard. The torsion-vibration spectrum of methanol trapped in neon matrix. *Chem. Phys.*, 332(1):86–94, 2007. doi: https://doi.org/10.1016/j.chemphys.2006.11.030. URL https://www.sciencedirect.com/science/article/pii/S0301010406006306.

[57] K. Kurotobi and Y. Murata. A single molecule of water encapsulated in fullerene C_{60}. *Science*, 333(6042):613–616, 2011. doi: 10.1126/science.1206376. URL https://doi.org/10.1126/science.1206376.

[58] D. Mitra, K. H. Leung, and T. Zelevinsky. Quantum control of molecules for fundamental physics. *Phys. Rev. A*, 105:040101, 2022. doi: 10.1103/PhysRevA.105.040101. URL https://link.aps.org/doi/10.1103/PhysRevA.105.040101.

[59] Wolfgang P. Schleich, Kedar S. Ranade, Christian Anton, Markus Arndt, Markus Aspelmeyer, Manfred Bayer, Gunnar Berg, Tommaso Calarco, Harald Fuchs, Elisabeth Giacobino, Markus Grassl, Peter Hänggi, Wolfgang M. Heckl, Ingolf-Volker Hertel, Susana Huelga, Fedor Jelezko, Bernhard Keimer, Jörg P. Kotthaus, Gerd Leuchs, Norbert Lütkenhaus, Ueli Maurer, Tilman Pfau, Martin B. Plenio, Ernst Maria Rasel, Ortwin Renn, Christine Silberhorn, Jörg Schiedmayer, Doris Schmitt-Landsiedel, Kurt Schönhammer, Alexey Ustinov, Philip Walther, Harald Weinfurter, Emo Welzl, Roland Wiesendanger, Stefan Wolf, Anton Zeilinger, and Peter Zoller. Quantum technology: from research to application. *Appl. Phys. B*, 122(5):130, 2016. doi: 10.1007/s00340-016-6353-8. URL https://doi.org/10.1007/s00340-016-6353-8.

[60] T. Kravchuk, M. Reznikov, P. Tichonov, N. Avidor, Y. Meir, A. Bekkerman, and G. Alexandrowicz. A magnetically focused molecular beam of ortho-water. *Science*, 331(6015):319–321, 2011. doi: 10.1126/science.1200433. URL http://www.sciencemag.org/cgi/doi/10.1126/science.1200433.

[61] Daniel A. Horke, Yuan-Pin Chang, Karol Długołęcki, and Jochen Küpper. Separating para and ortho water. *Angew. Chem. Int. Ed.*, 53:11965–11968, 2014. doi: 10.1002/anie.201405986. URL http://onlinelibrary.wiley.com/doi/10.1002/anie.201405986/abstract.

[62] Ardita Kilaj, Hong Gao, Daniel Rösch, Uxia Rivero, Jochen Küpper, and Stefan Willitsch. Observation of different reactivities of para- and ortho-water towards trapped diazenylium ions. *Nat. Commun.*, 9:2096, 2018. doi: 10.1038/s41467-018-04483-3. URL https://dx.doi.org/10.1038/s41467-018-04483-3.

[63] Debayan Mitra, Nathaniel B. Vilas, Christian Hallas, Benjamin L. Augenbraun Loïc Anderegg, Louis Baum, Calder Miller, Shivam Raval, and John M. Doyle. Direct laser cooling of a symmetric top molecule. *Science*, 369:1366–1369, 2020. doi: 10.1126/science.abc5357. URL https://www.science.org/doi/10.1126/science.abc5357.

[64] Nathaniel B. Vilas, Christian Hallas, Loïc Anderegg, Paige Robichaud, Andrew Winnicki, Debayan Mitra, and John M. Doyle. Magneto-optical trapping and sub-Doppler cooling of a polyatomic molecule. *Nature*, 606:70–74, 2022. doi: 10.1038/s41586-022-04620-5. URL https://doi.org/10.1038/s41586-022-04620-5.

[65] J. C. Raich and Jr. Good, R. H. Ortho-Para Transition in Molecular Hydrogen. *Astrophys. J.*, 139:1004, 1964. doi: 10.1086/147835. URL https://ui.adsabs.harvard.edu/abs/1964ApJ...139.1004R.

[66] Krzysztof Pachucki and Jacek Komasa. Ortho-para transition in molecular hydrogen. *Phys. Rev. A*, 77:030501, 2008. doi: 10.1103/PhysRevA.77.030501. URL https://link.aps.org/doi/10.1103/PhysRevA.77.030501.

[67] Irving Ozier, Pon-nyong Yi, Ashok Khosla, and Norman F. Ramsey. Direct observation of ortho-para transitions in methane. *Phys. Rev. Lett.*, 24:642–646, 1970. doi: 10.1103/PhysRevLett.24.642. URL https://link.aps.org/doi/10.1103/PhysRevLett.24.642.

[68] J. Bordé, Ch. J. Bordé, C. Salomon, A. Van Lerberghe, M. Ouhayoun, and C. D. Cantrell. Breakdown of the point-group symmetry of vibration-rotation states and optical observation of ground-state octahedral splittings of $^{32}SF_6$ using saturation spectroscopy. *Phys. Rev. Lett.*, 45:14–17, 1980. doi: 10.1103/PhysRevLett.45.14. URL https://link.aps.org/doi/10.1103/PhysRevLett.45.14.

[69] Hideto Kanamori, Zeinab T. Dehghani, Asao Mizoguchi, and Yasuki Endo. Detection of microwave transitions between ortho and para states in a free isolated molecule. *Phys. Rev. Lett.*, 119(17):173401, 2017. doi: 10.1103/PhysRevLett.119.173401. URL https://link.aps.org/doi/10.1103/PhysRevLett.119.173401.

[70] Frank Jensen. *Introduction to Computational Chemistry*. John Wiley & Sons, Chichester, West Sussex, UK, 3rd edition, 2016. ISBN 978-1-118-82599-0.

[71] Trygve Helgaker, Wim Klopper, and David P. Tew. Quantitative quantum chemistry. *Mol. Phys.*, 106(16-18):2107–2143, 2008. doi: 10.1080/00268970802258591. URL https://doi.org/10.1080/00268970802258591.

[72] Sergei N. Yurchenko, Walter Thiel, and Per Jensen. Theoretical ROVibrational Energies (TROVE): A robust numerical approach to the calculation of rovibrational energies for polyatomic molecules. *J. Mol. Spectrosc.*, 245(2):126–140, 2007. doi: 10.1016/j.jms.2007.07.009. URL https://doi.org/10.1016%2Fj.jms.2007.07.009.

[73] S. N. Yurchenko, A. Yachmenev, and R. I. Ovsyannikov. Symmetry adapted ro-vibrational basis functions for variational nuclear motion calculations: TROVE approach. *J. Chem. Theory Comput.*, 13:4368, 2017. doi: 10.1021/acs.jctc.7b00506. URL https://doi.org/10.1021/acs.jctc.7b00506.

[74] Philip R. Bunker and Per Jensen. *Molecular Symmetry and Spectroscopy*. NRC Research Press, Ottawa, Ontario, Canada, 2nd edition, 1998.

[75] Philip R. Bunker and Per Jensen. *Fundamentals of Molecular Symmetry*. Series in Chemical Physics. Institute of Physics Publishing, Bristol, UK, 2005. URL http://www.crcpress.com/product/isbn/9780750309417.

[76] Wolfgang Demtröder. *Laser Spectroscopy 1: Basic Principles*. Springer Verlag, Berlin, 2008. ISBN 978-3-540-73418-5. doi: 10.1007/978-3-540-73418-5.

[77] J. Tennyson and S. N. Yurchenko. The ExoMol project: Software for computing large molecular line lists. *Int. J. Quantum Chem.*, 117:92–103, 2017. doi: 10.1002/qua.25190. URL https://doi.org/10.1002/qua.25190.

[78] M. Born and R. Oppenheimer. Zur Quantentheorie der Molekeln. *Ann. Physik*, 84:457–484, 1927. doi: 10.1002/andp.19273892002. URL https://doi.org/10.1002/andp.19273892002.

[79] Richard N. Zare. *Angular Momentum*. John Wiley & Sons, New York, NY, USA, 1988. ISBN 0471858927.

[80] William G. Harter and Chris W. Patterson. Theory of hyperfine and superfine levels in symmetric polyatomic molecules. Trigonal and tetrahedral molecules: Elementary spin-$\frac{1}{2}$ cases in vibronic ground states. *Phys. Rev. A*, 19:2277–2303, 1979. doi: 10.1103/PhysRevA.19.2277. URL https://link.aps.org/doi/10.1103/PhysRevA.19.2277.

[81] William G. Harter. Theory of hyperfine and superfine levels in symmetric polyatomic molecules. II. Elementary cases in octahedral hexafluoride molecules. *Phys. Rev. A*,

24:192–263, 1981. doi: 10.1103/PhysRevA.24.192. URL https://link.aps.org/doi/10.1103/PhysRevA.24.192.

[82] R. O. Jones. Density functional theory: Its origins, rise to prominence, and future. *Rev. Mod. Phys.*, 87:897–923, 2015. doi: 10.1103/RevModPhys.87.897. URL https://link.aps.org/doi/10.1103/RevModPhys.87.897.

[83] Werner Kutzelnigg. How many-body perturbation theory (MBPT) has changed quantum chemistry. *Int. J. Quantum Chem.*, 109(15):3858–3884, 2009. doi: https://doi.org/10.1002/qua.22384. URL https://onlinelibrary.wiley.com/doi/abs/10.1002/qua.22384.

[84] D. R. Hartree. The wave mechanics of an atom with a non-Coulomb central field. Part I. Theory and methods. *Math. Proc. Camb. Philos. Soc.*, 24(1):89–110, 1928. doi: 10.1017/S0305004100011919. URL https://ui.adsabs.harvard.edu/abs/1928PCPS...24...89H.

[85] V. Fock. Näherungsmethode zur Lösung des quantenmechanischen Mehrkörperproblems. *Z. Phys.*, 61(1):126–148, 1930. doi: 10.1007/BF01340294. URL https://doi.org/10.1007/BF01340294.

[86] Dieter Cremer. From configuration interaction to coupled cluster theory: The quadratic configuration interaction approach. *Wiley Interdiscip. Rev. Comput. Mol. Sci.*, 3(5):482–503, 2013. doi: https://doi.org/10.1002/wcms.1131. URL https://wires.onlinelibrary.wiley.com/doi/abs/10.1002/wcms.1131.

[87] Rodney J. Bartlett and Monika Musiał. Coupled-cluster theory in quantum chemistry. *Rev. Mod. Phys.*, 79:291–352, 2007. doi: 10.1103/RevModPhys.79.291. URL https://link.aps.org/doi/10.1103/RevModPhys.79.291.

[88] Krishnan Raghavachari, Gary W. Trucks, John A. Pople, and Martin Head-Gordon. A fifth-order perturbation comparison of electron correlation theories. *Chem. Phys. Lett.*, 157(6):479–483, 1989. doi: https://doi.org/10.1016/S0009-2614(89)87395-6. URL https://www.sciencedirect.com/science/article/pii/S0009261489873956.

[89] Gustavo E. Scuseria and Timothy J. Lee. Comparison of coupled-cluster methods which include the effects of connected triple excitations. *J. Chem. Phys.*, 93(8):5851–5855, 1990. doi: 10.1063/1.459684. URL https://doi.org/10.1063/1.459684.

[90] John F. Stanton. Why CCSD(T) works: a different perspective. *Chem. Phys. Lett.*, 281(1):130–134, 1997. doi: https://doi.org/10.1016/S0009-2614(97)01144-5. URL https://www.sciencedirect.com/science/article/pii/S0009261497011445.

[91] Christof Hättig, Wim Klopper, Andreas Köhn, and David P. Tew. Explicitly correlated electrons in molecules. *Chem. Rev.*, 112(1):4–74, 2012. doi: 10.1021/cr200168z. URL https://doi.org/10.1021/cr200168z.

[92] Liguo Kong, Florian A. Bischoff, and Edward F. Valeev. Explicitly correlated R12/F12 methods for electronic structure. *Chem. Rev.*, 112(1):75–107, 2012. doi: 10.1021/cr200204r. URL https://doi.org/10.1021/cr200204r.

[93] Thomas B. Adler, Gerald Knizia, and Hans-Joachim Werner. A simple and efficient CCSD(T)-F12 approximation. *J. Chem. Phys.*, 127(22):221106, 2007. doi: 10.1063/1.2817618. URL https://doi.org/10.1063/1.2817618.

[94] J. C. Slater. Atomic shielding constants. *Phys. Rev.*, 36:57–64, 1930. doi: 10.1103/PhysRev.36.57. URL https://link.aps.org/doi/10.1103/PhysRev.36.57.

[95] S. F. Boys and Alfred Charles Egerton. Electronic wave functions I. A general method

of calculation for the stationary states of any molecular system. *Proc. Royal Soc. London A*, 200(1063):542–554, 1950. doi: 10.1098/rspa.1950.0036. URL https://royalsocietypublishing.org/doi/abs/10.1098/rspa.1950.0036.

[96] Richard C. Raffenetti. General contraction of gaussian atomic orbitals: Core, valence, polarization, and diffuse basis sets; Molecular integral evaluation. *J. Chem. Phys.*, 58 (10):4452–4458, 1973. doi: 10.1063/1.1679007. URL https://doi.org/10.1063/1.1679007.

[97] Thom H. Dunning. Gaussian basis functions for use in molecular calculations. I. Contraction of (9s5p) atomic basis sets for the first-row atoms. *J. Chem. Phys.*, 53 (7):2823–2833, 1970. doi: 10.1063/1.1674408. URL https://doi.org/10.1063/1.1674408.

[98] J. Grant Hill. Gaussian basis sets for molecular applications. *Int. J. Quantum Chem.*, 113(1):21–34, 2013. doi: https://doi.org/10.1002/qua.24355. URL https://onlinelibrary.wiley.com/doi/abs/10.1002/qua.24355.

[99] T. H. Dunning. Gaussian basis sets for use in correlated molecular calculations. I. The atoms boron through neon and hydrogen. *J. Chem. Phys.*, 90:1007, 1989. doi: 10.1063/1.456153. URL https://dx.doi.org/10.1063/1.456153.

[100] Rick A. Kendall, Thom H. Dunning, Jr., and Robert J. Harrison. Electron affinities of the first-row atoms revisited. Systematic basis sets and wave functions. *J. Chem. Phys.*, 96(9):6796–6806, 1992. doi: 10.1063/1.462569. URL http://dx.doi.org/10.1063/1.462569.

[101] Kirk A. Peterson and Thom H. Dunning. Accurate correlation consistent basis sets for molecular core–valence correlation effects: The second row atoms Al–Ar, and the first row atoms B–Ne revisited. *J. Chem. Phys.*, 117(23):10548–10560, 2002. doi: 10.1063/1.1520138. URL https://doi.org/10.1063/1.1520138.

[102] Werner Kutzelnigg and Wim Klopper. Wave functions with terms linear in the interelectronic coordinates to take care of the correlation cusp. I. General theory. *J. Chem. Phys.*, 94(3):1985–2001, 1991. doi: 10.1063/1.459921. URL https://doi.org/10.1063/1.459921.

[103] Volker Termath, Wim Klopper, and Werner Kutzelnigg. Wave functions with terms linear in the interelectronic coordinates to take care of the correlation cusp. II. Second-order Møller–Plesset (MP2-R12) calculations on closed-shell atoms. *J. Chem. Phys.*, 94(3):2002–2019, 1991. doi: 10.1063/1.459922. URL https://doi.org/10.1063/1.459922.

[104] Wim Klopper and Werner Kutzelnigg. Wave functions with terms linear in the interelectronic coordinates to take care of the correlation cusp. III. Second-order Møller–Plesset (MP2-R12) calculations on molecules of first row atoms. *J. Chem. Phys.*, 94(3):2020–2030, 1991. doi: 10.1063/1.459923. URL https://doi.org/10.1063/1.459923.

[105] J. Grant Hill, Shivnath Mazumder, and Kirk A. Peterson. Correlation consistent basis sets for molecular core-valence effects with explicitly correlated wave functions: The atoms B–Ne and Al–Ar. *J. Chem. Phys.*, 132(5):054108, 2010. doi: 10.1063/1.3308483. URL https://doi.org/10.1063/1.3308483.

[106] Kirk A. Peterson, Thomas B. Adler, and Hans-Joachim Werner. Systematically convergent basis sets for explicitly correlated wavefunctions: The atoms H, He, B–Ne, and Al–Ar. *J. Chem. Phys.*, 128(8):084102, 2008. doi: 10.1063/1.2831537. URL https://doi.org/10.1063/1.2831537.

[107] Kirk A. Peterson, Manoj K. Kesharwani, and Jan M. L. Martin. The cc-pV5Z-F12 basis set: reaching the basis set limit in explicitly correlated calculations. *Mol.*

Phys., 113(13-14):1551–1558, 2015. doi: 10.1080/00268976.2014.985755. URL https://doi.org/10.1080/00268976.2014.985755.

[108] Kirk A. Peterson, David Feller, and David A. Dixon. Chemical accuracy in ab initio thermochemistry and spectroscopy: current strategies and future challenges. *Theor. Chem. Acc.*, 131(1):1079, 2012. doi: 10.1007/s00214-011-1079-5. URL https://doi.org/10.1007/s00214-011-1079-5.

[109] David Feller, Kirk A. Peterson, and T. Daniel Crawford. Sources of error in electronic structure calculations on small chemical systems. *J. Chem. Phys.*, 124(5):054107, 2006. doi: 10.1063/1.2137323. URL https://doi.org/10.1063/1.2137323.

[110] Xinchuan Huang, David W. Schwenke, and Timothy J. Lee. An accurate global potential energy surface, dipole moment surface, and rovibrational frequencies for NH_3. *J. Chem. Phys.*, 129(21):214304, 2008. doi: 10.1063/1.3025885. URL https://doi.org/10.1063/1.3025885.

[111] G. Tarczay, A. G. Császár, W. Klopper, and H. M. Quiney. Anatomy of relativistic energy corrections in light molecular systems. *Mol. Phys.*, 99(21):1769–1794, 2001. doi: 10.1080/00268970110073907. URL https://doi.org/10.1080/00268970110073907.

[112] Max Born and Kun Huang. *Dynamical Theory of Crystal Lattices*. Clarendon Press, London, UK, 1954. ISBN 9780198503699.

[113] Ove Christiansen. Vibrational structure theory: new vibrational wave function methods for calculation of anharmonic vibrational energies and vibrational contributions to molecular properties. *Phys. Chem. Chem. Phys.*, 9:2942–2953, 2007. doi: 10.1039/B618764A. URL http://dx.doi.org/10.1039/B618764A.

[114] Ove Christiansen. Selected new developments in vibrational structure theory: potential construction and vibrational wave function calculations. *Phys. Chem. Chem. Phys.*, 14:6672–6687, 2012. doi: 10.1039/C2CP40090A. URL http://dx.doi.org/10.1039/C2CP40090A.

[115] Andrey Yachmenev and Sergei N. Yurchenko. Automatic differentiation method for numerical construction of the rotational-vibrational Hamiltonian as a power series in the curvilinear internal coordinates using the Eckart frame. *J. Chem. Phys.*, 143 (1):014105, 2015. doi: 10.1063/1.4923039. URL https://doi.org/10.1063/1.4923039.

[116] Sergei N. Yurchenko, Robert J. Barber, Andrey Yachmenev, Walter Thiel, Per Jensen, and Jonathan Tennyson. A variationally computed $T = 300$ K line list for NH_3. *J. Phys. Chem. A*, 113(43):11845–11855, 2009. doi: 10.1021/jp9029425. URL https://doi.org/10.1021/jp9029425.

[117] Sergei N. Yurchenko, Walter Thiel, and Per Jensen. Rotational energy cluster formation in XY_3 molecules: Excited vibrational states of BiH_3 and SbH_3. *J. Mol. Spectrosc.*, 240(2):174–187, 2006. doi: 10.1016/j.jms.2006.10.002. URL https://doi.org/10.1016/j.jms.2006.10.002.

[118] Sergei N. Yurchenko, Miguel Carvajal, Walter Thiel, and Per Jensen. Ab initio dipole moment and theoretical rovibrational intensities in the electronic ground state of PH_3. *J. Mol. Spectrosc.*, 239(1):71–87, 2006. doi: 10.1016/j.jms.2006.06.001. URL http://www.sciencedirect.com/science/article/pii/S0022285206001755.

[119] Andrey Yachmenev, Sergei N. Yurchenko, Per Jensen, Oliver Baum, Thomas F. Giesen, and Walter Thiel. Theoretical rotation–torsion spectra of HSOH. *Phys. Chem. Chem. Phys.*, 12:8387–8397, 2010. doi: https://doi.org/10.1016/j.jms.2009.06.010. URL https://pubs.rsc.org/en/content/articlehtml/2010/cp/c002803g.

[120] Sergei N. Yurchenko, Andrey Yachmenev, Walter Thiel, Oliver Baum, Thomas F.

Giesen, Vladlen V. Melnikov, and Per Jensen. An ab initio calculation of the vibrational energies and transition moments of HSOH. *J. Mol. Spectrosc.*, 257(1): 57–65, 2009. doi: 10.1039/c002803g. URL https://www.sciencedirect.com/science/article/pii/S0022285209001507.

[121] Andrey Yachmenev, Sergei N. Yurchenko, Tristan Ribeyre, and Walter Thiel. High-level *ab initio* potential energy surfaces and vibrational energies of H_2CS. *J. Chem. Phys.*, 135(7):074302, 2011. doi: 10.1063/1.3624570. URL https://doi.org/10.1063/1.3624570.

[122] Sergei N. Yurchenko, Jonathan Tennyson, Robert J. Barber, and Walter Thiel. Vibrational transition moments of CH_4 from first principles. *J. Mol. Spectrosc.*, 291: 69–76, 2013. doi: https://doi.org/10.1016/j.jms.2013.05.014. URL https://www.sciencedirect.com/science/article/pii/S0022285213000866.

[123] C. Eckart. Some studies concerning rotating axes and polyatomic molecules. *Phys. Rev.*, 47:552, 1935. doi: 10.1103/PhysRev.47.552. URL https://link.aps.org/doi/10.1103/PhysRev.47.552.

[124] B. V. Noumerov. A method of extrapolation of perturbations. *Mon. Not. R. Astron. Soc.*, 84(8):592–602, 1924. doi: 10.1093/mnras/84.8.592. URL https://doi.org/10.1093/mnras/84.8.592.

[125] J. W. Cooley. An improved eigenvalue corrector formula for solving the Schrödinger equation for central fields. *Math. Comput.*, 15(76):363–374, 1961. doi: 10.2307/2003025. URL https://doi.org/10.2307/2003025.

[126] Sergei N. Yurchenko, Robert J. Barber, Jonathan Tennyson, Walter Thiel, and Per Jensen. Towards efficient refinement of molecular potential energy surfaces: Ammonia as a case study. *J. Mol. Spectrosc.*, 268(1-2):123–129, 2011. doi: 10.1016/j.jms.2011.04.005. URL https://doi.org/10.1016/j.jms.2011.04.005.

[127] V. P. Kochanov. On systematic errors in spectral line parameters retrieved with the Voigt line profile. *J. Quant. Spectrosc. Radiat. Transf.*, 113(12):1635–1641, 2012. doi: https://doi.org/10.1016/j.jqsrt.2012.03.024. URL https://www.sciencedirect.com/science/article/pii/S0022407312001471.

[128] Jonathan Tennyson, Peter F. Bernath, Alain Campargue, Attila G. Császár, Ludovic Daumont, Robert R. Gamache, Joseph T. Hodges, Daniel Lisak, Olga V. Naumenko, Laurence S. Rothman, Ha Tran, Nikolai F. Zobov, Jeanna Buldyreva, Chris D. Boone, Maria Domenica De Vizia, Livio Gianfrani, Jean-Michel Hartmann, Robert McPheat, Damien Weidmann, Jonathan Murray, Ngoc Hoa Ngo, and Oleg L. Polyansky. Recommended isolated-line profile for representing high-resolution spectroscopic transitions (IUPAC technical report). *Pure Appl. Chem.*, 86(12):1931–1943, 2014. doi: doi: 10.1515/pac-2014-0208. URL https://doi.org/10.1515/pac-2014-0208.

[129] I.E. Gordon, L.S. Rothman, C. Hill, R.V. Kochanov, Y. Tan, P.F. Bernath, M. Birk, V. Boudon, A. Campargue, K.V. Chance, B.J. Drouin, J.-M. Flaud, R.R. Gamache, J.T. Hodges, D. Jacquemart, V.I. Perevalov, A. Perrin, K.P. Shine, M.-A.H. Smith, J. Tennyson, G.C. Toon, H. Tran, V.G. Tyuterev, A. Barbe, A.G. Császár, V.M. Devi, T. Furtenbacher, J.J. Harrison, J.-M. Hartmann, A. Jolly, T.J. Johnson, T. Karman, I. Kleiner, A.A. Kyuberis, J. Loos, O.M. Lyulin, S.T. Massie, S.N. Mikhailenko, N. Moazzen-Ahmadi, H.S.P. Müller, O.V. Naumenko, A.V. Nikitin, O.L. Polyansky, M. Rey, M. Rotger, S.W. Sharpe, K. Sung, E. Starikova, S.A. Tashkun, J. Vander Auwera, G. Wagner, J. Wilzewski, P. Wcisło, S. Yu, and E.J. Zak. The HITRAN2016 molecular spectroscopic database. *J. Quant. Spectrosc. Radiat. Transf.*, 203:3–69, 2017. doi: 10.1016/j.jqsrt.2017.06.038. URL http://www.sciencedirect.com/science/article/pii/S0022407317301073.

[130] Christian P. Endres, Stephan Schlemmer, Peter Schilke, Jürgen Stutzki, and Holger S.P. Müller. The Cologne Dtabase for Molecular Spectroscopy, CDMS, in the Virtual Atomic and Molecular Data Centre, VAMDC. *J. Mol. Spectrosc.*, 327:95–104, 2016. doi: https://doi.org/10.1016/j.jms.2016.03.005. URL https://www.sciencedirect.com/science/article/pii/S0022285216300340.

[131] H. M. Pickett, R. L. Poybter, E. A. Cohen, M. L. Delitsky, J. C. Pearson, and H. S. P. Müller. Submillimeter, millimeter, and microwave spectral line catalog. *J. Quant. Spectrosc. Radiat. Transf.*, 60(5):883–890, 1998. doi: https://doi.org/10.1016/S0022-4073(98)00091-0. URL https://www.sciencedirect.com/science/article/pii/S0022407398000910.

[132] S. W. Sharpe, T. J. Johnson, R. L. Sams, P. M. Chu, G. C. Rhoderick, and P. A. Johnson. Gas-phase databases for quantitative infrared spectroscopy. *Appl. Spectrosc.*, 58(12):1452–1461, 2004. doi: 10.1366/0003702042641281. URL https://doi.org/10.1366/0003702042641281.

[133] N. Jacquinet-Husson, L. Crepeau, R. Armante, C. Boutammine, A. Chédin, N.A. Scott, C. Crevoisier, V. Capelle, C. Boone, N. Poulet-Crovisier, A. Barbe, A. Campargue, D. Chris Benner, Y. Benilan, B. Bézard, V. Boudon, L.R. Brown, L.H. Coudert, A. Coustenis, V. Dana, V.M. Devi, S. Fally, A. Fayt, J.-M. Flaud, A. Goldman, M. Herman, G.J. Harris, D. Jacquemart, A. Jolly, I. Kleiner, A. Kleinböhl, F. Kwabia-Tchana, N. Lavrentieva, N. Lacome, Li-Hong Xu, O.M. Lyulin, J.-Y. Mandin, A. Maki, S. Mikhailenko, C.E. Miller, T. Mishina, N. Moazzen-Ahmadi, H.S.P. Müller, A. Nikitin, J. Orphal, V. Perevalov, A. Perrin, D.T. Petkie, A. Predoi-Cross, C.P. Rinsland, J.J. Remedios, M. Rotger, M.A.H. Smith, K. Sung, S. Tashkun, J. Tennyson, R.A. Toth, A.-C. Vandaele, and J. Vander Auwera. The 2009 edition of the GEISA spectroscopic database. *J. Quant. Spectrosc. Radiat. Transf.*, 112(15):2395–2445, 2011. doi: https://doi.org/10.1016/j.jqsrt.2011.06.004. URL https://www.sciencedirect.com/science/article/pii/S0022407311002160.

[134] Steven T. Cundiff and Jun Ye. Colloquium: Femtosecond optical frequency combs. *Rev. Mod. Phys.*, 75(1):325, 2003. URL http://link.aps.org/abstract/RMP/v75/p325.

[135] Scott A. Diddams, Kerry Vahala, and Thomas Udem. Optical frequency combs: Coherently uniting the electromagnetic spectrum. *Science*, 369(6501):3676, 2020. doi: 10.1126/science.aay3676. URL https://www.science.org/doi/abs/10.1126/science.aay3676.

[136] Theodor W Hänsch. Nobel lecture: Passion for precision. *Rev. Mod. Phys.*, 78(4):1297–1309, 2006. doi: 10.1103/RevModPhys.78.1297. URL https://link.aps.org/doi/10.1103/RevModPhys.78.1297.

[137] John Hall. Nobel lecture: Defining and measuring optical frequencies. *Rev. Mod. Phys.*, 78(4):1279–1295, 2006. doi: 10.1103/RevModPhys.78.1279. URL http://link.aps.org/doi/10.1103/RevModPhys.78.1279.

[138] T. M. Fortier, A. Bartels, and S. A. Diddams. Octave-spanning Ti:sapphire laser with a repetition rate > 1 GHz for optical frequency measurements and comparisons. *Opt. Lett.*, 31(7):1011–1013, 2006. doi: 10.1364/OL.31.001011. URL http://opg.optica.org/ol/abstract.cfm?URI=ol-31-7-1011.

[139] Feng-Lei Hong, Kaoru Minoshima, Atsushi Onae, Hajime Inaba, Hideyuki Takada, Akiko Hirai, Hirokazu Matsumoto, Toshiharu Sugiura, and Makoto Yoshida. Broad-spectrum frequency comb generation and carrier-envelope offset frequency measurement by second-harmonic generation of a mode-locked fiber laser. *Opt. Lett.*, 28(17):1516–1518, 2003. doi: 10.1364/OL.28.001516. URL http://opg.optica.org/

ol/abstract.cfm?URI=ol-28-17-1516.

[140] I. Pupeza, S. Holzberger, T. Eidam, H. Carstens, D. Esser, J. Weitenberg, P. Rußbüldt, J. Rauschenberger, J. Limpert, Th. Udem, A. Tünnermann, T. W. Hänsch, A. Apolonski, F. Krausz, and E. Fill. Compact high-repetition-rate source of coherent 100 eV radiation. *Nat. Photon.*, 7(8):608–612, 2013. doi: 10.1038/nphoton.2013.156. URL https://doi.org/10.1038/nphoton.2013.156.

[141] R. Jason Jones, Kevin D. Moll, Michael J. Thorpe, and Jun Ye. Phase-coherent frequency combs in the vacuum ultraviolet via high-harmonic generation inside a femtosecond enhancement cavity. *Phys. Rev. Lett.*, 94(19):193201, 2005. doi: 10.1103/PhysRevLett.94.193201. URL http://link.aps.org/abstract/PRL/v94/e193201.

[142] Christoph Gohle, Thomas Udem, Maximilian Herrmann, Jens Rauschenberger, Ronald Holzwarth, Hans A. Schuessler, Ferenc Krausz, and Theodor W. Hänsch. A frequency comb in the extreme ultraviolet. *Nature*, 436(7048):234–237, 2005. doi: 10.1038/nature03851. URL http://dx.doi.org/10.1038/nature03851.

[143] Arman Cingöz, Dylan C. Yost, Thomas K. Allison, Axel Ruehl, Martin E. Fermann, Ingmar Hartl, and Jun Ye. Direct frequency comb spectroscopy in the extreme ultraviolet. *Nature*, 482(7383):68–71, 2012. doi: 10.1038/nature10711. URL https://doi.org/10.1038/nature10711.

[144] Andrew J. Metcalf, Victor Torres-Company, Daniel E. Leaird, and Andrew M. Weiner. High-power broadly tunable electrooptic frequency comb generator. *IEEE J. Sel. Top. Quantum. Electron.*, 19(6):231–236, 2013. doi: 10.1109/JSTQE.2013.2268384. URL https://ieeexplore.ieee.org/document/6553388.

[145] Mian Zhang, Brandon Buscaino, Cheng Wang, Amirhassan Shams-Ansari, Christian Reimer, Rongrong Zhu, Joseph M. Kahn, and Marko Lončar. Broadband electro-optic frequency comb generation in a lithium niobate microring resonator. *Nature*, 568 (7752):373–377, 2019. doi: 10.1038/s41586-019-1008-7. URL https://doi.org/10.1038/s41586-019-1008-7.

[146] Scott A. Diddams, Long-Sheng Ma, Jun Ye, and John L. Hall. Broadband optical frequency comb generation with a phase-modulated parametric oscillator. *Opt. Lett.*, 24(23):1747–1749, 1999. doi: 10.1364/OL.24.001747. URL http://opg.optica.org/ol/abstract.cfm?URI=ol-24-23-1747.

[147] Martin E. Fermann and Ingmar Hartl. Ultrafast fibre lasers. *Nat. Photon.*, 7(11):868–874, 2013. doi: 10.1038/nphoton.2013.280. URL https://doi.org/10.1038/nphoton.2013.280.

[148] Mengjie Yu, Yoshitomo Okawachi, Austin G. Griffith, Nathalie Picqué, Michal Lipson, and Alexander L. Gaeta. Silicon-chip-based mid-infrared dual-comb spectroscopy. *Nat. Commun.*, 9(1):1869, 2018. doi: 10.1038/s41467-018-04350-1. URL https://doi.org/10.1038/s41467-018-04350-1.

[149] Yang He, Qi-Fan Yang, Jingwei Ling, Rui Luo, Hanxiao Liang, Mingxiao Li, Boqiang Shen, Heming Wang, Kerry Vahala, and Qiang Lin. Self-starting bichromatic $LiNbO_3$ soliton microcomb. *Optica*, 6(9):1138–1144, 2019. doi: 10.1364/OPTICA.6.001138. URL http://opg.optica.org/optica/abstract.cfm?URI=optica-6-9-1138.

[150] Xu Yi, Qi-Fan Yang, Ki Youl Yang, Myoung-Gyun Suh, and Kerry Vahala. Soliton frequency comb at microwave rates in a high-Q silica microresonator. *Optica*, 2(12): 1078–1085, 2015. doi: 10.1364/OPTICA.2.001078. URL http://opg.optica.org/optica/abstract.cfm?URI=optica-2-12-1078.

[151] Qing Li, Travis C. Briles, Daron A. Westly, Tara E. Drake, Jordan R. Stone, B. Robert

Ilic, Scott A. Diddams, Scott B. Papp, and Kartik Srinivasan. Stably accessing octave-spanning microresonator frequency combs in the soliton regime. *Optica*, 4(2):193–203, 2017. doi: 10.1364/OPTICA.4.000193. URL http://opg.optica.org/optica/abstract.cfm?URI=optica-4-2-193.

[152] T. J. Kippenberg, R. Holzwarth, and S. A. Diddams. Microresonator-based optical frequency combs. *Science*, 332(6029):555–559, 2011. doi: 10.1126/science.1193968. URL https://www.science.org/doi/abs/10.1126/science.1193968.

[153] V. Brasch, M. Geiselmann, T. Herr, G. Lihachev, M. H. P. Pfeiffer, M. L. Gorodetsky, and T. J. Kippenberg. Photonic chip-based optical frequency comb using soliton Cherenkov radiation. *Science*, 351(6271):357–360, 2016. doi: 10.1126/science.aad4811. URL https://www.science.org/doi/abs/10.1126/science.aad4811.

[154] P. Trocha, M. Karpov, D. Ganin, M. H. P. Pfeiffer, A. Kordts, S. Wolf, J. Krockenberger, P. Marin-Palomo, C. Weimann, S. Randel, W. Freude, T. J. Kippenberg, and C. Koos. Ultrafast optical ranging using microresonator soliton frequency combs. *Science*, 359(6378):887–891, 2018. doi: 10.1126/science.aao3924. URL https://www.science.org/doi/abs/10.1126/science.aao3924.

[155] Ian A. Finneran, Jacob T. Good, Daniel B. Holland, P. Brandon Carroll, Marco A. Allodi, and Geoffrey A. Blake. Decade-spanning high-precision terahertz frequency comb. *Phys. Rev. Lett.*, 114:163902, 2015. doi: 10.1103/PhysRevLett.114.163902. URL https://link.aps.org/doi/10.1103/PhysRevLett.114.163902.

[156] Takeshi Yasui, Yasuhiro Kabetani, Eisuke Saneyoshi, Shuko Yokoyama, and Tsutomu Araki. Terahertz frequency comb by multifrequency-heterodyning photoconductive detection for high-accuracy, high-resolution terahertz spectroscopy. *Appl. Phys. Lett.*, 88(24):241104, 2006. doi: 10.1063/1.2209718. URL https://doi.org/10.1063/1.2209718.

[157] Abijith S. Kowligy, Henry Timmers, Alexander J. Lind, Ugaitz Elu, Flavio C. Cruz, Peter G. Schunemann, Jens Biegert, and Scott A. Diddams. Infrared electric field sampled frequency comb spectroscopy. *Science Advances*, 5(6):8794, 2019. doi: 10.1126/sciadv.aaw8794. URL https://www.science.org/doi/abs/10.1126/sciadv.aaw8794.

[158] Florian Adler, Piotr Masłowski, Aleksandra Foltynowicz, Kevin C. Cossel, Travis C. Briles, Ingmar Hartl, and Jun Ye. Mid-infrared fourier transform spectroscopy with a broadband frequency comb. *Opt. Exp.*, 18(21):21861–21872, 2010. doi: 10.1364/OE.18.021861. URL http://www.opticsexpress.org/abstract.cfm?URI=oe-18-21-21861.

[159] I. Hartl, G. Imeshev, L. Dong, G. C. Cho, and M. E. Fermann. Ultra-compact dispersion compensated femtosecond fiber oscillators and amplifiers. In *(CLEO). Conference on Lasers and Electro-Optics, 2005.*, volume 3, pages 1641–1643, 2005. doi: 10.1109/CLEO.2005.202226. URL https://ieeexplore.ieee.org/document/1573292.

[160] Donna Strickland and Gerard Mourou. Compression of amplified chirped optical pulses. *Opt. Comm.*, 55(6):447–449, 1985. doi: https://doi.org/10.1016/0030-4018(85)90151-8. URL https://www.sciencedirect.com/science/article/pii/0030401885901518.

[161] Roland E. Best. *Phase-Locked Loops: Design, Simulation, and Applications*. McGraw-Hill, New York, USA, 6th edition, 2007. ISBN 9780071493758. URL https://www.accessengineeringlibrary.com/content/book/9780071493758.

[162] H. R. Telle, G. Steinmeyer, A. E. Dunlop, J. Stenger, D. H. Sutter, and U. Keller. Carrier-envelope offset phase control: A novel concept for absolute optical frequency

measurement and ultrashort pulse generation. *Appl. Phys. B*, 69:327–332, 1999. doi: 10.1007/s003400050813. URL https://doi.org/10.1007/s003400050813.

[163] K. A. Tillman, R. R. J. Maier, D. T. Reid, and E. D. McNaghten. Mid-infrared absorption spectroscopy across a 14.4 THz spectral range using a broadband femtosecond optical parametric oscillator. *Appl. Phys. Lett.*, 85(16):3366–3368, 2004. doi: 10.1063/1.1808239. URL https://doi.org/10.1063/1.1808239.

[164] Ł. Kornaszewski, N. Gayraud, J. M. Stone, W. N. MacPherson, A. K. George, J. C. Knight, D. P. Hand, and D. T. Reid. Mid-infrared methane detection in a photonic bandgap fiber using a broadband optical parametric oscillator. *Opt. Exp.*, 15(18):11219–11224, 2007. doi: 10.1364/OE.15.011219. URL http://www.opticsexpress.org/abstract.cfm?URI=oe-15-18-11219.

[165] Zsuzsanna Heiner, Valentin Petrov, Günter Steinmeyer, Marc J. J. Vrakking, and Mark Mero. 100-kHz, dual-beam OPA delivering high-quality, 5-cycle angular-dispersion-compensated mid-infrared idler pulses at 3.1 µm. *Opt. Express*, 26(20):25793–25804, 2018. doi: 10.1364/OE.26.025793. URL http://www.opticsexpress.org/abstract.cfm?URI=oe-26-20-25793.

[166] Grzegorz Soboń, Tadeusz Martynkien, Paweł Mergo, Lucile Rutkowski, and Aleksandra Foltynowicz. High-power frequency comb source tunable from 2.7 to 4.2 µm based on difference frequency generation pumped by an Yb-doped fiber laser. *Opt. Lett.*, 42(9):1748–1751, 2017. doi: 10.1364/OL.42.001748. URL http://ol.osa.org/abstract.cfm?URI=ol-42-9-1748.

[167] Axel Ruehl, Alessio Gambetta, Ingmar Hartl, Martin E. Fermann, Kjeld S. E. Eikema, and Marco Marangoni. Widely-tunable mid-infrared frequency comb source based on difference frequency generation. *Opt. Lett.*, 37(12):2232–2234, 2012. doi: 10.1364/OL.37.002232. URL http://ol.osa.org/abstract.cfm?URI=ol-37-12-2232.

[168] Marcus Zimmermann, Christoph Gohle, Ronald Holzwarth, Thomas Udem, and Theodor W. Hänsch. Optical clockwork with an offset-free difference-frequency comb: accuracy of sum- and difference-frequency generation. *Opt. Lett.*, 29(3):310–312, 2004. doi: 10.1364/OL.29.000310. URL http://opg.optica.org/ol/abstract.cfm?URI=ol-29-3-310.

[169] Liang Dong, Brian K. Thomas, and Libin Fu. Highly nonlinear silica suspended core fibers. *Opt. Exp.*, 16(21):16423–16430, 2008. doi: 10.1364/OE.16.016423. URL http://www.opticsexpress.org/abstract.cfm?URI=oe-16-21-16423.

[170] Vinicius Silva de Oliveira, Axel Ruehl, Piotr Masłowski, and Ingmar Hartl. Intensity noise optimization of a mid-infrared frequency comb difference-frequency generation source. *Opt. Lett.*, 45(7):1914–1917, 2020. doi: 10.1364/OL.391195. URL http://ol.osa.org/abstract.cfm?URI=ol-45-7-1914.

[171] R. S. Hughes. *Logarithmic Amplification: With Application to Radar and EW*. Artech House, Dedham, MA, USA, 1986. ISBN 9780890061824. URL https://books.google.de/books?id=2Q9TAAAAMAAJ.

[172] I. Hartl, X. D. Li, C. Chudoba, R. K. Ghanta, T. H. Ko, J. G. Fujimoto, J. K. Ranka, and R. S. Windeler. Ultrahigh-resolution optical coherence tomography using continuum generation in an air-silica microstructure optical fiber. *Opt. Lett.*, 26(9):608–610, 2001. doi: 10.1364/OL.26.000608. URL http://opg.optica.org/ol/abstract.cfm?URI=ol-26-9-608.

[173] Pierre Connes. Early history of Fourier transform spectroscopy. *Infrared Physics*, 24 (2):69–93, 1984. doi: https://doi.org/10.1016/0020-0891(84)90052-6. URL https://www.sciencedirect.com/science/article/pii/0020089184900526.

[174] Melvin B. Comisarow and Alan G. Marshall. Fourier transform ion cyclotron

resonance spectroscopy. *Chem. Phys. Lett.*, 25(2):282–283, 1974. doi: https://doi.org/10.1016/0009-2614(74)89137-2. URL https://www.sciencedirect.com/science/article/pii/0009261474891372.

[175] R. R. Ernst and W. A. Anderson. Application of Fourier transform spectroscopy to magnetic resonance. *Rev. Sci. Instrum.*, 37(1):93–102, 1966. doi: 10.1063/1.1719961. URL https://doi.org/10.1063/1.1719961.

[176] Peter R. Griffiths and James A. de Haseth. *Fourier Transform Infrared Spectrometry*. John Wiley & Sons, Hoboken, New Jersey, USA, 2nd edition, 2007. ISBN 978-0-471-19404-0.

[177] Sieghard Albert, Karen Keppler Albert, and Martin Quack. *High-Resolution Fourier Transform Infrared Spectroscopy*. John Wiley & Sons, 2011. ISBN 9780470749593. doi: https://doi.org/10.1002/9780470749593.hrs042. URL https://onlinelibrary.wiley.com/doi/abs/10.1002/9780470749593.hrs042.

[178] Julien Mandon, Guy Guelachvili, and Nathalie Picqué. Fourier transform spectroscopy with a laser frequency comb. *Nat. Photon.*, 3:99–102, 2009. URL https://www.nature.com/articles/nphoton.2008.293#citeas.

[179] C. R. Phillips, J. Jiang, C. Mohr, A. C. Lin, C. Langrock, M. Snure, D. Bliss, M. Zhu, I. Hartl, J. S. Harris, M. E. Fermann, and M. M. Fejer. Widely tunable midinfrared difference frequency generation in orientation-patterned GaAs pumped with a femtosecond Tm-fiber system. *Opt. Lett.*, 37(14):2928–2930, 2012. doi: 10.1364/OL.37.002928. URL http://opg.optica.org/ol/abstract.cfm?URI=ol-37-14-2928.

[180] Ben Spaun, P. Bryan Changala, David Patterson, Bryce J. Bjork, Oliver H. Heckl, John M. Doyle, and Jun Ye. Continuous probing of cold complex molecules with infrared frequency comb spectroscopy. *Nature*, 533(7604):517–520, 2016. doi: 10.1038/nature17440. URL https://doi.org/10.1038/nature17440.

[181] C. Erny, K. Moutzouris, J. Biegert, D. Kühlke, F. Adler, A. Leitenstorfer, and U. Keller. Mid-infrared difference-frequency generation of ultrashort pulses tunable between 3.2 and 4.8 µm from a compact fiber source. *Opt. Lett.*, 32(9):1138–1140, 2007. doi: 10.1364/OL.32.001138. URL http://opg.optica.org/ol/abstract.cfm?URI=ol-32-9-1138.

[182] H. R. Carleton and W. T. Maloney. A balanced optical heterodyne detector. *Appl. Opt.*, 7(6):1241–1243, 1968. doi: 10.1364/AO.7.001241. URL http://opg.optica.org/ao/abstract.cfm?URI=ao-7-6-1241.

[183] Horace P. Yuen and Vincent W. S. Chan. Noise in homodyne and heterodyne detection. *Opt. Lett.*, 8(3):177–179, 1983. doi: 10.1364/OL.8.000177. URL http://opg.optica.org/ol/abstract.cfm?URI=ol-8-3-177.

[184] Philip E. Ciddor. Refractive index of air: new equations for the visible and near infrared. *Appl. Opt.*, 35(9):1566–1573, 1996. doi: 10.1364/AO.35.001566. URL http://opg.optica.org/ao/abstract.cfm?URI=ao-35-9-1566.

[185] Piotr Maslowski, Kevin F. Lee, Alexandra C. Johansson, Amir Khodabakhsh, Grzegorz Kowzan, Lucile Rutkowski, Andrew A. Mills, Christian Mohr, Jie Jiang, Martin E. Fermann, and Aleksandra Foltynowicz. Surpassing the path-limited resolution of Fourier-transform spectrometry with frequency combs. *Phys. Rev. A*, 93:021802, 2016. doi: 10.1103/PhysRevA.93.021802. URL https://link.aps.org/doi/10.1103/PhysRevA.93.021802.

[186] Lucile Rutkowski, Piotr Masłowski, Alexandra C. Johansson, Amir Khodabakhsh, and Aleksandra Foltynowicz. Optical frequency comb fourier transform spectroscopy with sub-nominal resolution and precision beyond the Voigt profile. *J. Quant.*

Spectrosc. Radiat. Transf., 204:63–73, 2018. doi: https://doi.org/10.1016/j.jqsrt.2017.09.001. URL https://www.sciencedirect.com/science/article/pii/S0022407317300201.

[187] Andrea Miani and Jonathan Tennyson. Can ortho–para transitions for water be observed? *J. Chem. Phys.*, 120(6):2732–2739, 2004. doi: 10.1063/1.1633261. URL https://doi.org/10.1063/1.1633261.

[188] Michiel R. Hogerheijde, Edwin A. Bergin, Christian Brinch, L. Ilsedore Cleeves, Jeffrey K. J. Fogel, Geoffrey A. Blake, Carsten Dominik, Dariusz C. Lis, Gary Melnick, David Neufeld, Olja Panić, John C Pearson, Lars Kristensen, Umut A. Yıldız, and Ewine F. van Dishoeck. Detection of the water reservoir in a forming planetary system. *Science*, 334(6054):338–340, 2011. doi: 10.1126/science.1208931. URL http://www.sciencemag.org/content/334/6054/338.abstract.

[189] Dariusz C. Lis, Edwin A. Bergin, Peter Schilke, and Ewine F. van Dishoeck. *Ortho*-to-*Para* ratio in interstellar water on the sightline toward sagittarius B2(N). *J. Phys. Chem. A*, 117(39):9661–9665, 2013. doi: 10.1021/jp312333n. URL http://dx.doi.org/10.1021/jp312333n.

[190] N. Flagey, P. F. Goldsmith, D. C. Lis, M. Gerin, D. Neufeld, P. Sonnentrucker, M. De Luca, B. Godard, J. R. Goicoechea, R. Monje, and T. G. Phillips. Water absorption in galactic translucent clouds: Conditions and history of the gas derived from *Herschel*/HIFI PRISMAS observations. *Astrophys. J.*, 762(1):11, 2012. doi: 10.1088/0004-637x/762/1/11. URL https://doi.org/10.1088%2F0004-637x%2F762%2F1%2F11.

[191] Ewine F. van Dishoeck, Eric Herbst, and David A. Neufeld. Interstellar water chemistry: From laboratory to observations. *Chem. Rev.*, 113(12):9043–9085, 2013. doi: 10.1021/cr4003177. URL http://pubs.acs.org/doi/abs/10.1021/cr4003177.

[192] Ernest Ilisca. Ortho-para conversion of hydrogen molecules physisorbed on surfaces. *Prog. Surf. Sci.*, 41(3):217–335, 1992. doi: 10.1016/0079-6816(92)90019-e. URL https://doi.org/10.1016/0079-6816(92)90019-e.

[193] David Hollenbach, Michael J. Kaufman, Edwin A. Bergin, and Gary J. Melnick. Water, O_2, and ice in molecular clouds. *Astrophys. J.*, 690(2):1497–1521, 2008. doi: 10.1088/0004-637x/690/2/1497. URL https://doi.org/10.1088/0004-637x/690/2/1497.

[194] T. Hama, N. Watanabe, A. Kouchi, and M. Yokoyama. Spin temperature of water molecules desorbed from the surfaces of amorphous solid water, vapor-deposited and produced from photolysis of a CH_4/O_2 solid mixture. *Astrophys. J.*, 738(1):L15, 2011. doi: 10.1088/2041-8205/738/1/l15. URL https://doi.org/10.1088/2041-8205/738/1/l15.

[195] T. Hama, A. Kouchi, and N. Watanabe. Statistical ortho-to-para ratio of water desorbed from ice at 10 kelvin. *Science*, 351(6268):65–67, 2015. doi: 10.1126/science.aad4026. URL https://doi.org/10.1126/science.aad4026.

[196] Yang Liu and Le Luo. Molecular collisions: From near-cold to ultra-cold. *Front. Phys.*, 16(4):42300, 2021. doi: 10.1007/s11467-020-1037-6. URL https://doi.org/10.1007/s11467-020-1037-6.

[197] Katy L. Chubb, Andrey Yachmenev, Jonathan Tennyson, and Sergei N. Yurchenko. Treating linear molecule HCCH in calculations of rotation-vibration spectra. *J. Chem. Phys.*, 149(1):014101, 2018. doi: 10.1063/1.5031844. URL https://doi.org/10.1063/1.5031844.

[198] Irina I. Mizus, Aleksandra A. Kyuberis, Nikolai F. Zobov, Vladimir Yu. Makhnev,

Oleg L. Polyansky, and Jonathan Tennyson. High-accuracy water potential energy surface for the calculation of infrared spectra. *Philosophical Transactions of the Royal Society A: Mathematical, Physical and Engineering Sciences*, 376:20170149, 2018. doi: 10.1098/rsta.2017.0149. URL https://doi.org/10.1098/rsta.2017.0149.

[199] Andrey Yachmenev and Jochen Küpper. Communication: General variational approach to nuclear-quadrupole coupling in rovibrational spectra of polyatomic molecules. *J. Chem. Phys.*, 147(14):141101, 2017. doi: 10.1063/1.5002533. URL https://doi.org/10.1063/1.5002533.

[200] Andrey Yachmenev, Linda V. Thesing, and Jochen Küpper. Laser-induced dynamics of molecules with strong nuclear quadrupole coupling. *J. Chem. Phys.*, 151(24):244118, 2019. doi: 10.1063/1.5133837. URL https://doi.org/10.1063/1.5133837.

[201] W. H. Flygare. Magnetic interactions in molecules and an analysis of molecular electronic charge distribution from magnetic parameters. *Chem. Rev.*, 74(6):653–687, 1974. doi: 10.1021/cr60292a003. URL https://doi.org/10.1021/cr60292a003.

[202] Alec Owens and Andrey Yachmenev. RichMol: A general variational approach for rovibrational molecular dynamics in external electric fields. *J. Chem. Phys.*, 148 (12):124102, 2018. doi: 10.1063/1.5023874. URL https://doi.org/10.1063/1.5023874.

[203] Cem Saribal, Guang Yang, Emil Zak, Yahya Saleh, Jannik Eggers, Vishnu Sanjay, Andrey Yachmenev, and Jochen Küpper. Richmol: Python package for variational simulations of molecular nuclear motion dynamics in fields. *Comp. Phys. Comm.*, in preparation, 2021. The current version of the software is available at https://github.com/CFEL-CMI/richmol.

[204] James K. G. Watson. Aspects of quartic and sextic centrifugal effects on rotational energy levels. In J. R. Durig, editor, *Vibrational Spectra and Structure*, volume 6, page 1. Marcel Dekker, 1977.

[205] Benjamin P. Pritchard, Doaa Altarawy, Brett Didier, Tara D. Gibson, and Theresa L. Windus. New basis set exchange: An open, up-to-date resource for the molecular sciences community. *J. Chem. Inf. Model.*, 59(11):4814–4820, 2019. doi: 10.1021/acs.jcim.9b00725. URL https://doi.org/10.1021/acs.jcim.9b00725.

[206] David Feller. The role of databases in support of computational chemistry calculations. *J. Comput. Chem.*, 17(13):1571–1586, 1996. doi: 10.1002/(sici)1096-987x(199610)17:13<1571::aid-jcc9>3.0.co;2-p. URL https://doi.org/10.1002/(sici)1096-987x(199610)17:13<1571::aid-jcc9>3.0.co;2-p.

[207] Karen L. Schuchardt, Brett T. Didier, Todd Elsethagen, Lisong Sun, Vidhya Gurumoorthi, Jared Chase, Jun Li, and Theresa L. Windus. Basis set exchange: A community database for computational sciences. *J. Chem. Inf. Model.*, 47(3):1045–1052, 2007. doi: 10.1021/ci600510j. URL https://doi.org/10.1021/ci600510j.

[208] Gustavo E. Scuseria. Analytic evaluation of energy gradients for the singles and doubles coupled cluster method including perturbative triple excitations: Theory and applications to FOOF and Cr_2. *J. Chem. Phys.*, 94(1):442–447, 1991. doi: 10.1063/1.460359. URL https://doi.org/10.1063/1.460359.

[209] Jürgen Gauss, Kenneth Ruud, and Trygve Helgaker. Perturbation-dependent atomic orbitals for the calculation of spin-rotation constants and rotational g tensors. *J. Chem. Phys.*, 105(7):2804–2812, 1996. doi: 10.1063/1.472143. URL https://doi.org/10.1063/1.472143.

[210] Jurgen Gauss and Dage Sundholm. Coupled-cluster calculations of spin-rotation constants. *Mol. Phys.*, 91(3):449–458, 1997. doi: 10.1080/002689797171346. URL https://doi.org/10.1080/002689797171346.

[211] J. F. Stanton, J. Gauss, L. Cheng, M. E. Harding, D. A. Matthews, and P. G. Szalay. CFOUR, Coupled-Cluster techniques for Computational Chemistry, a quantum-chemical program package. With contributions from A.A. Auer, R.J. Bartlett, U. Benedikt, C. Berger, D.E. Bernholdt, S. Blaschke, Y. J. Bomble, S. Burger, O. Christiansen, D. Datta, F. Engel, R. Faber, J. Greiner, M. Heckert, O. Heun, M. Hilgenberg, C. Huber, T.-C. Jagau, D. Jonsson, J. Jusélius, T. Kirsch, K. Klein, G.M. KopperW.J. Lauderdale, F. Lipparini, T. Metzroth, L.A. Mück, D.P. O'Neill, T. Nottoli, D.R. Price, E. Prochnow, C. Puzzarini, K. Ruud, F. Schiffmann, W. Schwalbach, C. Simmons, S. Stopkowicz, A. Tajti, J. Vázquez, F. Wang, J.D. Watts and the integral packages MOLECULE (J. Almlöf and P.R. Taylor), PROPS (P.R. Taylor), ABACUS (T. Helgaker, H.J. Aa. Jensen, P. Jørgensen, and J. Olsen), and ECP routines by A. V. Mitin and C. van Wüllen. For the current version, see http://www.cfour.de.

[212] Sergei N. Yurchenko and Thomas M. Mellor. Treating linear molecules in calculations of rotation-vibration spectra. *J. Chem. Phys.*, 153(15):154106, 2020. doi: 10.1063/5.0019546. URL https://doi.org/10.1063/5.0019546.

[213] Andrey Yachmenev, Sergei N. Yurchenko, Ivana Paidarová, Per Jensen, Walter Thiel, and Stephan P. A. Sauer. Thermal averaging of the indirect nuclear spin-spin coupling constants of ammonia: The importance of the large amplitude inversion mode. *J. Chem. Phys.*, 132(11):114305, 2010. doi: 10.1063/1.3359850. URL https://doi.org/10.1063/1.3359850.

[214] Gabriele Cazzoli, Cristina Puzzarini, Michael E. Harding, and Jürgen Gauss. The hyperfine structure in the rotational spectrum of water: Lamb-dip technique and quantum-chemical calculations. *Chem. Phys. Lett.*, 473(1-3):21–25, 2009. doi: 10.1016/j.cplett.2009.03.045. URL https://doi.org/10.1016/j.cplett.2009.03.045.

[215] Jonathan Tennyson, Peter F. Bernath, Linda R. Brown, Alain Campargue, Attila G. Császár, Ludovic Daumont, Robert R. Gamache, Joseph T. Hodges, Olga V. Naumenko, Oleg L. Polyansky, Laurence S. Rothman, Ann Carine Vandaele, Nikolai F. Zobov, Afaf R. Al Derzi, Csaba Fábri, Alexander Z. Fazliev, Tibor Furtenbacher, Iouli E. Gordon, Lorenzo Lodi, and Irina I. Mizus. IUPAC critical evaluation of the rotational–vibrational spectra of water vapor, part III: Energy levels and transition wavenumbers for $H_2{}^{16}O$. *J. Quant. Spectrosc. Radiat. Transf.*, 117:29–58, 2013. doi: 10.1016/j.jqsrt.2012.10.002. URL https://doi.org/10.1016/j.jqsrt.2012.10.002.

[216] Jonathan Tennyson, Sergei N. Yurchenko, Ahmed F. Al-Refaie, Victoria H.J. Clark, Katy L. Chubb, Eamon K. Conway, Akhil Dewan, Maire N. Gorman, Christian Hill, A.E. Lynas-Gray, Thomas Mellor, Laura K. McKemmish, Alec Owens, Oleg L. Polyansky, Mikhail Semenov, Wilfrid Somogyi, Giovanna Tinetti, Apoorva Upadhyay, Ingo Waldmann, Yixin Wang, Samuel Wright, and Olga P. Yurchenko. The 2020 release of the ExoMol database: Molecular line lists for exoplanet and other hot atmospheres. *J. Quant. Spectrosc. Radiat. Transf.*, 255:107228, 2020. doi: 10.1016/j.jqsrt.2020.107228. URL https://doi.org/10.1016/j.jqsrt.2020.107228.

[217] Alain Campargue, Alexander M. Solodov, Alexander A. Solodov, Andrey Yachmenev, and Sergei N. Yurchenko. Detection of electric-quadrupole transitions in water vapour near 5.4 and 2.5 µm. *Phys. Chem. Chem. Phys.*, 22(22):12476–12481, 2020. doi: 10.1039/d0cp01667e. URL https://doi.org/10.1039/d0cp01667e.

[218] Alain Campargue, Samir Kassi, Andrey Yachmenev, Aleksandra A. Kyuberis, Jochen Küpper, and Sergei N. Yurchenko. Observation of electric-quadrupole

infrared transitions in water vapor. *Phys. Rev. Research*, 2(2):023091, 2020. doi: 10.1103/physrevresearch.2.023091. URL https://doi.org/10.1103/physrevresearch.2.023091.

[219] Hélène Fleurbaey, Roberto Grilli, Didier Mondelain, Samir Kassi, Andrey Yachmenev, Sergei N. Yurchenko, and Alain Campargue. Electric-quadrupole and magnetic-dipole contributions to the $\nu_2 + \nu_3$ band of carbon dioxide near 3.3 µm. *J. Quant. Spectrosc. Radiat. Transf.*, 266:107558, 2021. doi: 10.1016/j.jqsrt.2021.107558. URL https://doi.org/10.1016/j.jqsrt.2021.107558.

[220] Andrey Yachmenev, Alain Campargue, Sergei N. Yurchenko, Jochen Küpper, and Jonathan Tennyson. Electric quadrupole transitions in carbon dioxide. *J. Chem. Phys.*, 154(21):211104, 2021. doi: 10.1063/5.0053279. URL https://doi.org/10.1063/5.0053279.

[221] Oleg L. Polyansky, Aleksandra A. Kyuberis, Nikolai F. Zobov, Jonathan Tennyson, Sergei N. Yurchenko, and Lorenzo Lodi. ExoMol molecular line lists XXX: a complete high-accuracy line list for water. *Mon. Not. R. Astron. Soc.*, 480(2):2597–2608, 2018. doi: 10.1093/mnras/sty1877. URL https://doi.org/10.1093/mnras/sty1877.

[222] Jonathan Tennyson, Sergei N. Yurchenko, Ahmed F. Al-Refaie, Emma J. Barton, Katy L. Chubb, Phillip A. Coles, S. Diamantopoulou, Maire N. Gorman, Christian Hill, Aden Z. Lam, Lorenzo Lodi, Laura K. McKemmish, Yueqi Na, Alec Owens, Oleg L. Polyansky, Tom Rivlin, Clara Sousa-Silva, Daniel S. Underwood, Andrey Yachmenev, and Emil Zak. The ExoMol database: Molecular line lists for exoplanet and other hot atmospheres. *J. Mol. Spectrosc.*, 327:73–94, 2016. doi: 10.1016/j.jms.2016.05.002. URL http://www.sciencedirect.com/science/article/pii/S0022285216300807.

[223] H. Bluyssen, A. Dymanus, and J. Verhoeven. Hyperfine structure of H_2O and HDSe by beam-maser spectroscopy. *Phys. Lett. A*, 24(9):482–483, 1967. doi: 10.1016/0375-9601(67)90154-5. URL https://www.sciencedirect.com/science/article/pii/0375960167901545.

[224] Samir Kassi and Alain Campargue. Cavity ring down spectroscopy with 5×10^{-13} cm^{-1} sensitivity. *J. Chem. Phys.*, 137(23):234201, 2012. doi: 10.1063/1.4769974. URL https://doi.org/10.1063/1.4769974.

[225] E. V. Karlovets, S. Kassi, and A. Campargue. High sensitivity CRDS of CO_2 in the 1.18 µm transparency window. Validation tests of current spectroscopic databases. *J. Quant. Spectrosc. Radiat. Transfer*, 247:106942, 2020. doi: 10.1016/j.jqsrt.2020.106942. URL https://doi.org/10.1016/j.jqsrt.2020.106942.

[226] Roland Tóbiás, Tibor Furtenbacher, Irén Simkó, Attila G. Császár, Meissa L. Diouf, Frank M. J. Cozijn, Joey M. A. Staa, Edcel J. Salumbides, and Wim Ubachs. Spectroscopic-network-assisted precision spectroscopy and its application to water. *Nat. Commun.*, 11(1):1708, 2020. doi: 10.1038/s41467-020-15430-6. URL https://doi.org/10.1038/s41467-020-15430-6.

[227] Stephen G. Kukolich. Measurement of the molecular g values in H_2O and D_2O and hyperfine structure in H_2O. *J. Chem. Phys.*, 50(9):3751–3755, 1969. doi: 10.1063/1.1671623. URL https://doi.org/10.1063/1.1671623.

[228] G. Yu. Golubiatnikov, V. N. Markov, A. Guarnieri, and R. Knöchel. Hyperfine structure of $H_2{}^{16}O$ and $H_2{}^{18}O$ measured by Lamb-dip technique in the 180–560 GHz frequency range. *J. Mol. Spectrosc.*, 240(2):251–254, 2006. doi: 10.1016/j.jms.2006.09.012. URL https://www.sciencedirect.com/science/article/pii/S0022285206002591.

[229] Ch. Daussy, T. Marrel, A. Amy-Klein, C. T. Nguyen, Ch. J. Bordé, and Ch. Chardonnet. Limit on the parity nonconserving energy difference between the enantiomers of a chiral molecule by laser spectroscopy. *Phys. Rev. Lett.*, 83:1554–1557, 1999. doi: 10.1103/PhysRevLett.83.1554. URL https://link.aps.org/doi/10.1103/PhysRevLett.83.1554.

[230] S. N. Yurchenko, A. F. Al-Refaie, and J. Tennyson. ExoCross: a general program for generating spectra from molecular line lists. *Astron. Astrophys.*, 614:A131, 2018. doi: 10.1051/0004-6361/201732531. URL https://doi.org/10.1051/0004-6361/201732531.

[231] Alain Campargue, Samir Kassi, Krzysztof Pachucki, and Jacek Komasa. The absorption spectrum of H_2: CRDS measurements of the (2-0) band, review of the literature data and accurate *ab initio* line list up to 35 000 cm^{-1}. *Phys. Chem. Chem. Phys.*, 14:802–815, 2011. doi: 10.1039/C1CP22912E. URL http://dx.doi.org/10.1039/C1CP22912E.

[232] A. C. Cheung, D. M. Rank, C. H. Townes, D. D. Thornton, and W. J. Welch. Detection of NH_3 molecules in the interstellar medium by their microwave emission. *Phys. Rev. Lett.*, 21:1701–1705, 1968. doi: 10.1103/PhysRevLett.21.1701. URL https://link.aps.org/doi/10.1103/PhysRevLett.21.1701.

[233] J. P. Gordon, H. J. Zeiger, and C. H. Townes. The Maser—new type of microwave amplifier, frequency standard, and spectrometer. *Phys. Rev.*, 99:1264–1274, 1955. doi: 10.1103/PhysRev.99.1264. URL https://link.aps.org/doi/10.1103/PhysRev.99.1264.

[234] J. P. Gordon, H. J. Zeiger, and C. H. Townes. Molecular microwave oscillator and new hyperfine structure in the microwave spectrum of NH_3. *Phys. Rev.*, 95:282–284, 1954. doi: 10.1103/PhysRev.95.282. URL https://link.aps.org/doi/10.1103/PhysRev.95.282.

[235] Š. Urban, V. Špirko, D. Papoušek, J. Kauppinen, S. P. Belov, L. I. Gershtein, and A. F. Krupnov. A simultaneous analysis of the microwave, submillimeterwave, far infrared, and infrared-microwave two-photon transitions between the ground and ν_2 inversion-rotation levels of $^{14}NH_3$. *J. Mol. Spectrosc.*, 88(2):274–292, 1981. doi: 10.1016/0022-2852(81)90179-X. URL http://www.sciencedirect.com/science/article/pii/002228528190179X.

[236] Brian J. Drouin, Shanshan Yu, John C. Pearson, and Harshal Gupta. Terahertz spectroscopy for space applications: 2.5–2.7 THz spectra of HD, H_2O and NH_3. *J. Mol. Spectrosc.*, 1006(1):2–12, 2011. doi: 10.1016/j.molstruc.2011.05.062. URL http://www.sciencedirect.com/science/article/pii/S0022286011004509.

[237] J. J. Hillman, D. E. Jennings, and J. L. Faris. Diode laser–CO_2 laser heterodyne spectrometer: measurement of 2sQ(1,1) in $2\nu_2$–ν_2 of NH_3. *Appl. Opt.*, 18(11):1808–1811, 1979. doi: 10.1364/AO.18.001808. URL http://ao.osa.org/abstract.cfm?URI=ao-18-11-1808.

[238] C. Cottaz, G. Tarrago, I. Kleiner, and L. R. Brown. Assignments and intensities of $^{14}NH_3$ hot bands in the 5- to 8-µm ($3\nu_2$–ν_2, ν_2+ν_4–ν_2) and 4-µm ($4\nu_2$–ν_2, ν_1–ν_2, ν_3–ν_2 and $2\nu_4$–ν_2) regions. *J. Mol. Spectrosc.*, 209(1):30–49, 2001. doi: 10.1006/jmsp.2001.8406. URL http://www.sciencedirect.com/science/article/pii/S0022285201984061.

[239] I. Kleiner, G. Tarrago, and L. R. Brown. Positions and intensities in the $3\nu_2/\nu_2+\nu_4$ vibrational system of $^{14}NH_3$ near 4 µm. *J. Mol. Struct.*, 173(1):120–145, 1995. doi: 10.1006/jmsp.1995.1224. URL http://www.sciencedirect.com/science/article/pii/S0022285285712246.

[240] Jeniveve Pearson, Shanshan Yu, John Pearson, Keeyoon Sung, Brian Drouin, and Olivier Pirali. Extended measurements and an experimental accuracy effective Hamiltonian model for the $3\nu_2$ and $\nu_4 + \nu_2$ states of ammonia. *J. Mol. Spectrosc.*, 353: 60–66, 2018. doi: 10.1016/j.jms.2018.09.004. URL http://www.sciencedirect.com/science/article/pii/S0022285218302406.

[241] Li Li, R. M. Lees, and Li-Hong Xu. External cavity tunable diode laser spectra of the $\nu_1 + 2\nu_4$ stretch-bend combination bands of $^{14}NH_3$ and $^{15}NH_3$. *J. Mol. Spectrosc.*, 243(2):219–226, 2007. doi: 10.1016/j.jms.2007.04.003. URL http://www.sciencedirect.com/science/article/pii/S0022285207000987.

[242] Stephen R. Langford, Andrew J. Orr-Ewing, Ross A. Morgan, Colin M. Western, Michael N. R. Ashfold, Arjan Rijkenberg, Connie R. Scheper, Wybren Jan Buma, and Cornelis A. de Lange. The spectroscopy of high Rydberg states of ammonia. *J. Chem. Phys.*, 108(16):6667–6680, 1998. doi: 10.1063/1.476082. URL https://doi.org/10.1063/1.476082.

[243] A. E. Douglas. Electronically excited states of ammonia. *Discuss. Faraday Soc.*, 35:158–174, 1963. doi: 10.1039/DF9633500158. URL http://dx.doi.org/10.1039/DF9633500158.

[244] Jacqueline van Veldhoven, Jochen Küpper, Hendrick L. Bethlem, Boris Sartakov, André J. A. van Roij, and Gerard Meijer. Decelerated molecular beams for high-resolution spectroscopy: The hyperfine structure of $^{15}ND_3$. *Eur. Phys. J. D*, 31(2): 337–349, 2004. doi: 10.1140/epjd/e2004-00160-9. URL http://dx.doi.org/10.1140/epjd/e2004-00160-9.

[245] P. Coles, A. Owens, J. Küpper, and A. Yachmenev. Hyperfine-resolved rotation-vibration line list of ammonia (NH_3). *Astrophys. J.*, 870(1):24, 2018. doi: 10.3847/1538-4357/aaef7e. URL https://doi.org/10.3847/1538-4357/aaef7e.

[246] Sylvestre Twagirayezu, Gregory E. Hall, and Trevor J. Sears. Quadrupole splittings in the near-infrared spectrum of $^{14}NH_3$. *J. Chem. Phys.*, 145(14):144302, 2016. doi: 10.1063/1.4964484. URL https://doi.org/10.1063/1.4964484.

[247] Afaf R. Al Derzi, Tibor Furtenbacher, Jonathan Tennyson, Sergei N. Yurchenko, and Attila G. Császár. Marvel analysis of the measured high-resolution spectra of $^{14}NH_3$. *J. Quant. Spectrosc. Radiat. Transf.*, 161:117–130, 2015. doi: 10.1016/j.jqsrt.2015.03.034. URL http://www.sciencedirect.com/science/article/pii/S0022407315001442.

[248] Kevin C. Cossel, Eleanor M. Waxman, Ian A. Finneran, Geoffrey A. Blake, Jun Ye, and Nathan R. Newbury. Gas-phase broadband spectroscopy using active sources: progress, status, and applications. *J. Opt. Soc. Am. B*, 34(1):104–129, 2017. doi: 10.1364/JOSAB.34.000104. URL http://josab.osa.org/abstract.cfm?URI=josab-34-1-104.

[249] Markus W. Signets. *High-resolution Infrared Laser Spectroscopy and Gas Sensing Applications*. John Wiley & Sons, 2011. ISBN 9780470749593. doi: 10.1002/9780470749593.hrs046. URL https://onlinelibrary.wiley.com/doi/abs/10.1002/9780470749593.hrs046.

[250] Tonglei Cheng, Kenshiro Nagasaka, Tong Hoang Tuan, Xiaojie Xue, Morio Matsumoto, Hiroshige Tezuka, Takenobu Suzuki, and Yasutake Ohishi. Mid-infrared supercontinuum generation spanning 2.0 to 15.1 µm in a chalcogenide step-index fiber. *Opt. Lett.*, 41:2117–2120, 2016. doi: 10.1364/OL.41.002117. URL http://ol.osa.org/abstract.cfm?URI=ol-41-9-2117.

[251] Zheming Zhao, Xunsi Wang, Shixun Dai, Zhanghao Pan, Shuo Liu, Lihong Sun, Peiqing Zhang, Zijun Liu, Qiuhua Nie, Xiang Shen, and Rongping Wang. 1.5–14 µm

midinfrared supercontinuum generation in a low-loss Te-based chalcogenide step-index fiber. *Opt. Lett.*, 41:5222–5225, 2016. doi: 10.1364/OL.41.005222. URL http://ol.osa.org/abstract.cfm?URI=ol-41-22-5222.

[252] Eisen C. Gross, Kimberly A. Tsang, and Trevor J. Sears. Re-evaluation of ortho-para-dependence of self pressure-broadening in the $\nu_1 + \nu_3$ band of acetylene. *J. Chem. Phys.*, 154(5):054305, 2021. doi: 10.1063/5.0036602. URL https://doi.org/10.1063/5.0036602.

[253] Vassilii Nemtchinov, Keeyoon Sung, and Prasad Varanasi. Measurements of line intensities and half-widths in the 10-µm bands of $^{14}NH_3$. *J. Quant. Spectrosc. Radiat. Transf.*, 83(3):243–265, 2004. doi: 10.1016/S0022-4073(02)00354-0. URL http://www.sciencedirect.com/science/article/pii/S0022407302003540.

[254] Wolfgang Demtröder. *Doppler-free Laser Spectroscopy*. John Wiley & Sons, 2011. ISBN 9780470749593. doi: https://doi.org/10.1002/9780470749593.hrs082. URL https://onlinelibrary.wiley.com/doi/abs/10.1002/9780470749593.hrs082.

[255] Aleksandra Foltynowicz, Lucile Rutkowski, Isak Silander, Alexandra C. Johansson, Vinicius Silva de Oliveira, Ove Axner, Grzegorz Soboń, Tadeusz Martynkien, Paweł Mergo, and Kevin K. Lehmann. Sub-Doppler double-resonance spectroscopy of methane using a frequency comb probe. *Phys. Rev. Lett.*, 126:063001, 2021. doi: 10.1103/PhysRevLett.126.063001. URL https://link.aps.org/doi/10.1103/PhysRevLett.126.063001.

[256] Wolfgang Demtröder. *Laser Spectroscopy 2: Experimental Techniques*. Springer Verlag, Berlin, 2008. ISBN 978-3-662-44641-6. doi: 10.1007/978-3-662-44641-6.

[257] Toshiki Sugimoto and Katsuyuki Fukutani. Electric-field-induced nuclear-spin flips mediated by enhanced spin–orbit coupling. *Nat. Phys.*, 7(4):307–310, 2011. doi: 10.1038/nphys1883. URL https://doi.org/10.1038/nphys1883.

[258] P. R. Bunker and P. Jensen. Chirality in rotational energy level clusters. *J. Mol. Spectrosc.*, 228(2):640–644, 2004. doi: 10.1016/j.jms.2004.02.027. URL https://www.sciencedirect.com/science/article/pii/S0022285204000773.

[259] Alec Owens, Andrey Yachmenev, Sergei N. Yurchenko, and Jochen Küpper. Climbing the Rotational Ladder to Chirality. *Phys. Rev. Lett.*, 121(19):193201, 2018. doi: 10.1103/physrevlett.121.193201. URL https://doi.org/10.1103/physrevlett.121.193201.

[260] A. Owens, A. Yachmenev, and J. Küpper. Coherent control of the rotation axis of molecular superrotors. *J. Phys. Chem. Lett.*, 9(15):4206–4209, 2018. doi: 10.1021/acs.jpclett.8b01689. URL https://dx.doi.org/10.1021/acs.jpclett.8b01689.

[261] Joanna Karczmarek, James Wright, Paul Corkum, and Misha Ivanov. Optical centrifuge for molecules. *Phys. Rev. Lett.*, 82(17):3420–3423, 1999. doi: 10.1103/PhysRevLett.82.3420. URL https://link.aps.org/doi/10.1103/PhysRevLett.82.3420.

[262] A. A. Milner, A. Korobenko, K. Rezaiezadeh, and V. Milner. From gyroscopic to thermal motion: A crossover in the dynamics of molecular superrotors. *Phys. Rev. X*, 5(3):031041, 2015. doi: 10.1103/PhysRevX.5.031041. URL https://link.aps.org/doi/10.1103/PhysRevX.5.031041.

[263] L. D. Barron. True and false chirality and parity violation. *Chem. Phys. Lett.*, 123(5):423–427, 1986. doi: 10.1016/0009-2614(86)80035-5. URL https://www.sciencedirect.com/science/article/pii/0009261486800355.

[264] D. DeMille, S. B. Cahn, D. Murphree, D. A. Rahmlow, and M. G. Kozlov. Using molecules to measure nuclear spin-dependent parity violation. *Phys. Rev. Lett.*, 100

(2):023003, 2008. doi: 10.1103/physrevlett.100.023003. URL https://doi.org/10.1103%2Fphysrevlett.100.023003.

[265] Emine Altuntaş, Jeffrey Ammon, Sidney B. Cahn, and David DeMille. Demonstration of a sensitive method to measure nuclear-spin-dependent parity violation. *Phys. Rev. Lett.*, 120:142501, 2018. doi: 10.1103/PhysRevLett.120.142501. URL https://link.aps.org/doi/10.1103/PhysRevLett.120.142501.

Acronyms

CBS complete basis set.

CC coupled-cluster.

CI configuration interaction.

CW continuous wave.

DFG difference frequency generation.

DLA demodulating logarithm amplifier.

FBG fiber Bragg grating.

FC frequency comb.

FCI full configuration interaction.

FFT fast Fourier transform.

FP Fabry-Pérot.

FTS Fourier transform spectrometer.

GTO Gaussian-type orbital.

HeNe helium-neon.

HF Hartree-Fock.

HNLF highly-nonlinear suspended-core fiber.

HWHM half-width at half-maximum.

InSb indium antimonide.

KEO kinetic energy operator.

MIR mid-infrared.

MO molecular orbit.

MOT magnetic-optical trapping.

NPR nonlinear polarization rotation.

OODR optical-optical double-resonance.

OPA optical parametric amplification.

OPD optical path difference.

OPO optical parametric oscillator.

OPR *ortho-para* ratio.

PLL phase-locked loop.

PPLN periodically poled Lithium Niobate.

PSD power spectral density.

PZT piezoelectric ceramic transducer.

RF radio frequency.

RIN relative intensity noise.

SA saturable absorber.

SNR signal-to-noise ratio.

TIA transimpedance amplifier.

TROVE theoretical rovibrational energies.

Acknowledgments

I would like to extend my sincere thanks to all the people who have contributed to this thesis and supported me in any respect on this special journey.

First of all, I want to thank my supervisor Jochen Küpper and co-supervisor Andrey Yachmenev for providing me an opportunity to perform my doctoral research in the Controlled Molecule Imaging group (CMI) at the Center for Free-Electron Laser Science (CFEL), Deutsches Elektronen-Synchrotron (DESY). I learned a lot from both of them and I am thankful for their support, advise, and guidance throughout the whole project. Many thanks to our collaborator Ingmar Hartl for the opportunity to do experiment in FS-LA group at DESY. I benefited much from his incredible experimental skills and his enthusiasm in doing experiments.

I could not have undertaken this journey without people that contributed to this work, either through help in theoretical calculations and simulations, or through participating in the experiments and data analysis. I would like to extend my sincere thanks to CMI-theory team led by Andrey Yachmenev. Many thanks to Andrey Yachmenev, Alec Owens, Andrei Duchko, Linda Thesing and Yahya Saleh for constructive discussions and suggestions on this project. Special thanks to Emil Zak and Cem Saribal for the great help in working together with the nuclear spin density for H_2S, field-dressed and field-gradient-dressed spectrum of water, and Richmol. I would like to also thank Sergey Yurchenko for his advice in creating the hyperfine linelist for water. Many thanks to Ahmed Al-Refaie for his guide in coding and exocross. I am also grateful to Phillip Coles for passing not only the knowledge of molecular symmetry but also deadlift. Thanks should also go to Vinicius Silva de Oliveira and Dominic Laumer for measuring the frequency comb spectrum of ammonia together.

I had the pleasure of working and discussing with all colleagues from both CMI and FS-LA group. Many thanks to Amit Samanta, Armando Estillore, Christoph Heyl, Evangelos Karamatskos, Helen Bieker, Jannik Lübke, Jia Wang, Jolijn Onvlee, Joss Wiese, Jovana Petrovic, Lanhai He, Lena Worbs, Matthew Robinson, Melby Johny, Nils Roth, Prannay Balla, Ruth Livingstone, Sebastian Trippel, Stefanie Kerbstadt, Terry Mullins, Xiaoyan Sun and Zhipeng Huang for their help in many aspects on this 5-year journey. I would like to offer my special thanks to Lena Worbs and Jannik Lübke for writing the thesis together. Many thanks to Karol Długołęcki and Lucas Gonschior for the machine drawing of liquid-nitrogen-cooled multi-pass-cell cryostat. Thanks a lot to Barbora Vagovič for all the paper work and issue arrangements for being the connection with Jochen.

I'm extremely grateful to the "lightning weight-loss group" for not only quantitatively modeling and controlling our weight and health condition, but also the good memories. I am indebted to Liwei Song, Lianghui Huang, Yuxuan Ma for being my roommates and Anna Beck being my landlady that make me feel just at home. Words cannot express my gratitude to Lanhai He and Chufeng Li for the brain storm and sharing of experiences during the coffee time after lunch. Special thanks go to Junmin Wang for his care and instruction in both life and science. Many thanks also go to Bufftreff football team and DESY basketball group for making my body being on the way. I would like to acknowledge financial support from China Scholarship Council (CSC).

Last but not least, I would like to express my deepest gratitude to my family and friends that supported me during this whole journey. I thank my parents for their support in financial and otherwise throughout my whole education. I want to thank my sister and grandma for their great support. I am also thankful to my friends Yang Yu, Yue Cao, Fan Cheng, Lopsang Thundrup, Sherp Yantso, Nini, Yifan Hu for their concerns and encouragements.

List of publications

Publications related to this thesis:

2022 Andrey Yachmenev, **Guang Yang**, Sergei Yurchenko, Emil Zak, Jochen Küpper, "The nuclear-spin-forbidden rovibrational transitions of water from first principles", *J. Chem. Phys.*, **156**, 204307 (2022), arXiv:2203.07945 [physics].

2022 **Guang Yang**, Vinicius Silva de Oliveira, Dominic Laumer, Christoph Heyl, Andrey Yachmenev, Ingmar Hartl, Jochen Küpper, "Self-broadening and self-shift in the $3\nu_2$ band of ammonia from mid-infrared frequency-comb spectroscopy", **submitted to** *J. Mol. Spec.* (2022), arXiv:2205.04088 [physics].

Other publications I have contributed to:

2022 **Guang Yang**, Cem Saribal, Emil Zak, Andrey Yachmenev, Jochen Küpper, "The enhanced *ortho-para* transitions of water in external field and field gradient", **in preparation** (2022).

2022 Cem Saribal, **Guang Yang**, Emil Zak, Yahya Saleh, Jannik Eggers, Vishnu Sanjay, Andrey Yachmenev, Jochen Küpper, "Richmol: Python package for variational simulations of molecular nuclear motion dynamics in fields", **in preparation** (2022).

Eidesstattliche Versicherung / Declaration on oath

Hiermit versichere ich an Eides statt, die vorliegende Dissertationschrift selbst verfasst und keine anderen als die angegebenen Hilfsmittel und Quellen benutzt zu haben. Die eingereichte schriftliche Fassung entspricht der auf dem elektronischen Speichermedium. Die Dissertation wurde in der vorgelegten oder einer ähnlichen Form nicht schon einmal in einem früheren Promotionsverfahren angenommen oder als ungenügend beurteilt.

Hamburg, den 25.11.2022 Unterschrift: Guang Yang